Seismicity and Crustal Structure in North Greenland

Annette Ellingsen

Thesis for the degree

Master of Science

University of Bergen

Department of Earth Science

June 1, 2018

Abstract

The crustal structure of Greenland varies greatly across the island. Previous studies have revealed that the region of North Greenland differs from the rest of Greenland, with a more shallow crustal thickness. Although this region is far from any plate boundary, earthquakes do occur. Locating these intraplate earthquakes can lead to a better understanding of the seismicity in the area.

A challenge of understanding this region is the lack of seismic data available, as few seismic stations are in operation. However, four temporary stations were in operation from 2004 to 2007, and the data obtained gives new insights in the tectonic processes in the remote area. The velocity model used in this region today is a uniform velocity model for all of Greenland. Using the same velocity model for the entire island is not logical, as the crustal structure varies. It is thus beneficial to obtain a regional velocity model for North Greenland.

The main objective of this thesis has been to find a new velocity model for North Greenland and this has been done using information about the crustal structure in the region. To obtain the knowledge needed, a joint inversion of receiver functions and apparent S-wave velocities has been performed. Shear wave velocity as a function of depth beneath the seismic stations was obtained and further implemented into a new regional velocity model. Earthquakes in the area were then relocated and the different locations were compared to locations obtained with the Greenland Velocity Model.

Acknowledgements

First, I would like to thank my supervisors at the University of Bergen, Lars Ottemöller, Stéphane Rondenay and Mathilde Sørensen, for all the guidance, suggestions and feedback during this thesis. Further, I would like to thank my co-supervisors at GEUS, Peter Voss and Trine Dahl-Jensen, for their contribution with data and discussions of the results.

I would also like to thank Anne Drottning for all her help during this last year. Even though she is not listed as a supervisor, she has acted as one in every possible way. She has continued to develop the program and increased my understanding of the method used in this thesis.

In addition, I would like to thank Marthe Vestly and Karina Løviknes for feedback on different chapters of the writing. My fellow classmates, thank you for the daily lunch breaks and the many hours spent together in classes and at Gneis.

Finally, I would like to direct a special thanks to my dear friend and roommate, Anette Nygaard, for proofreading the entire thesis. Thank you for providing me with motivating words and endless support.

Contents

1. Introduction

The seismicity of North Greenland is poorly known, because few seismic stations have been in operation in this remote area. During the period 2004-2007, four temporary seismic stations were deployed in North Greenland, by The Geological Survey of Denmark and Greenland (GEUS). This data provides new opportunities to get a better understanding of the tectonic processes in this region.

1.1 Motivation

The tectonic history of Greenland has resulted in a diverse geology across the island and many authors have made efforts to understand the complex structure of Greenland. A surface wave dispersion study by Gregersen (1984) revealed some crustal structure anomalies near continental margins. It was assumed that on average, the structure of Greenland was similar to the eastern Canadian Shield. Four years later, a new study using spectral ratio curves and five seismic stations, made it clear that there are some significant structural differences between Greenland and Canada (Gregersen et al., 1988).

The crustal structure was further investigated by Dahl-Jensen et al. (2003), using receiver function analysis. This article describes the results from the GLATIS-project (Greenland Lithosphere Analysed Teleseismically on the Ice Sheet), which in 1999 and gave access to geological data of the continental crust across Greenland.

The project showed that the depth of the Moho in the southern part of Greenland is significantly greater than the crustal thickness in North Greenland. This is illustrated in Figure 1.1, that shows the estimated Moho depths beneath stations across Greenland. The widespread crustal thickness was unknown before the publication of the results obtained in the GLATIS-project. The two gray stations in Figure 1.1 were not part of the GLATIS-project, but other studies who also estimated Moho depth. Luckily, these stations are located in the study area of this thesis.

Since the structure in Greenland was assumed to be similar to the structure in Canada, the velocity model available for Canada was implemented for Greenland. It is today the general velocity model used by GEUS to locate earthquakes for all of Greenland. With knowledge about the crustal structure differences across Greenland, it is not realistic to use the same velocity model for the entire island when locating earthquakes. It is obvious that the locations estimated would then, in some places, have a large error.

To obtain a regional velocity model, detailed information about the crustal structure is needed. The temporary stations operating in North Greenland between 2004-2007 are the main sources of information and these stations form the basis for the work in this thesis. Data from these stations are supplemented with data from permanent stations located around the region.

1.2 Objective

Synthetic tests can be performed to show that the location accuracy is dependent and varies greatly on the choice of velocity model. Figure 1.2 shows this. A set of earthquakes was used to estimate epicenter locations with two distinct velocity models, where one was assumed to be the correct velocity model. It is clear from Figure 1.2 that some of the estimated locations are far from each other, something that shows the large error in the locations estimated with the wrong velocity model. How the synthetic tests were performed will be explained in Chapter 4: Method.

The synthetic tests show the need for a local velocity model for North Greenland. The main objective of this thesis is therefore to make a new, more

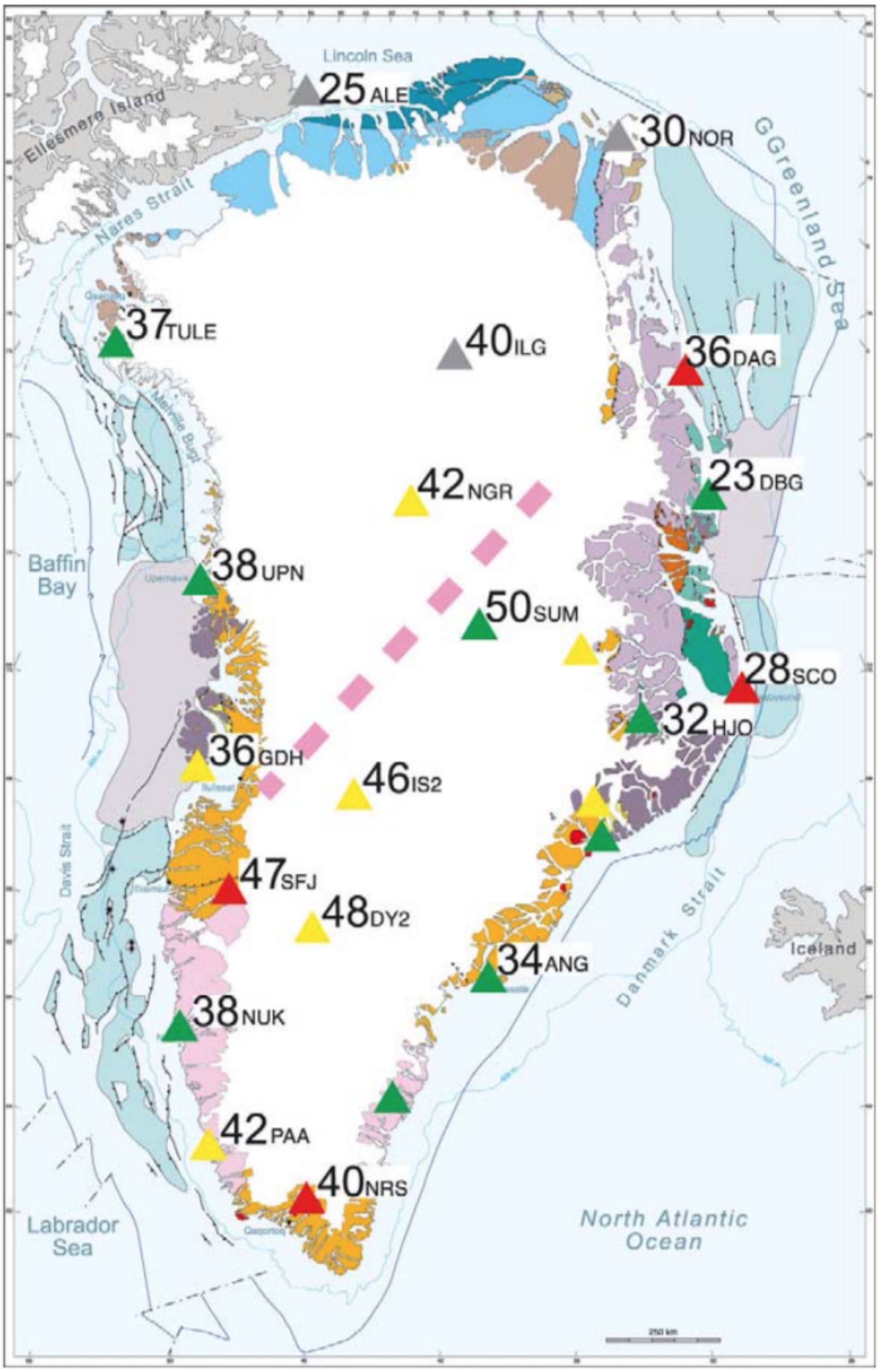

Figure 1.1: Estimated Moho depth beneath stations across Greenland. The red, yellow and green stations were included in the GLATIS-project. The gray stations are from other studies. The map is obtained from Dahl-Jensen et al. (2003).

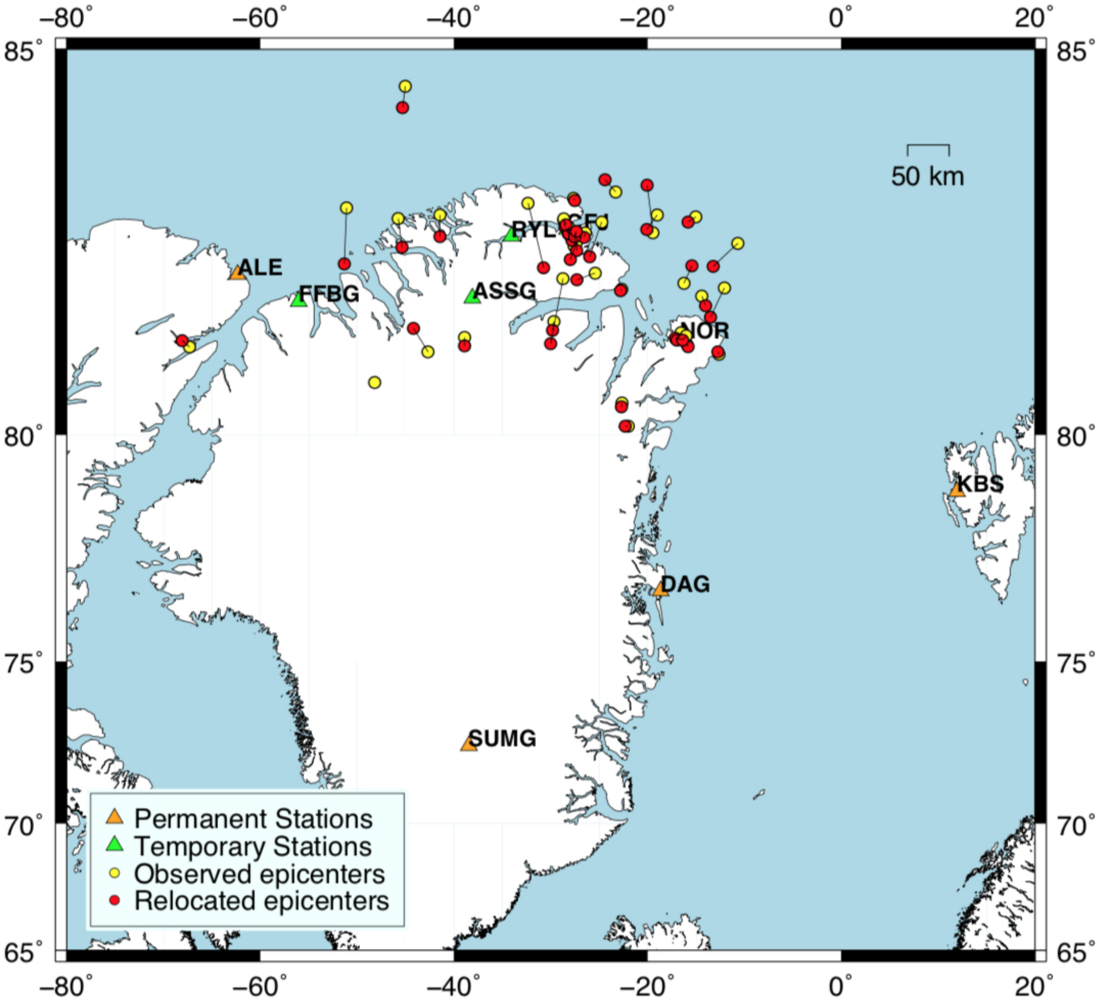

Figure 1.2: The results from a synthetic test. The red and yellow dots are estimated epicenter locations obtained using two distinct velocity models.

detailed velocity model for the region and use it to relocate earthquakes in the area. Accurate relocation is important to get a better understanding of the seismic activity.

1.3 Outline

The work performed in this thesis is presented in seven chapters. First, I will give an overview of the geological and tectonical framework of the study area in Chapter 2, before the data that is analyzed in this study will be introduced in Chapter 3. The background theory needed to understand the method is explained shortly in the beginning of Chapter 4, before the method used to obtain information about the crustal structure of the area is presented in the same chapter. The results obtained with the joint inversion method are images of the subsurface beneath the stations, these are presented in Chapter 5, where they are also used to obtain a series of new regional velocity models. The earthquakes are further relocated with one of the new velocity models. In Chapter 6 are the structure results and the relocations discussed and a conclusion is provided in the end of the thesis in Chapter 7.

2. Geological and Tectonical Framework

This chapter will examine the main stages of the tectonic history of how Greenland has developed from the earliest of times, where the geology of North Greenland will be described in more detail. The focus is on North Greenland as that is the main area of interest for this thesis.

2.1 Tectonic History

The geological development of Greenland started in Precambrian (4000 Ma; early Archean). This is when crustal rocks first started to form and continental crust became a significant amount of the surface of the Earth (Marshak, 2011). The dominant basement rocks of Greenland consist of crystalline gneisses and plutonic rocks (Kanao et al., 2015). They were formed during orogenic activities and can be divided into three different types of basement provinces that together make up the Precambrian Shield (Henriksen et al., 2000):

1. 3100-2600 Ma: Archean Rocks. These rocks are almost unaffected by later orogenic activity.

2. Reworked Archean rocks. These rocks have gone through metamorphism in the early Proterozoic period and are therefore reworked from Archean rocks (1850 Ma; early Proterozoic).

3. 2000-1750 Ma: Early Proterozoic juvenile Rocks.

All of these rocks are older than 1600 Ma and are known as the Laurentian Shield. The distribution of these rocks are shown in Figure 2.1 (Henriksen et al., 2000). In North Greenland, none of these rocks are exposed, because the area is covered by younger sediments.

Figure 2.1: Simplified map of the Precambrian Shield in Greenland, showing the distribution of the three different provinces. Orange: Preserved Archean rocks (1). Yellow: Reworked Archean rocks (2). Pink: Juvenile Proterozoic rocks (3). The white areas are ice or younger formations. Figure extracted from Henriksen et al. (2000).

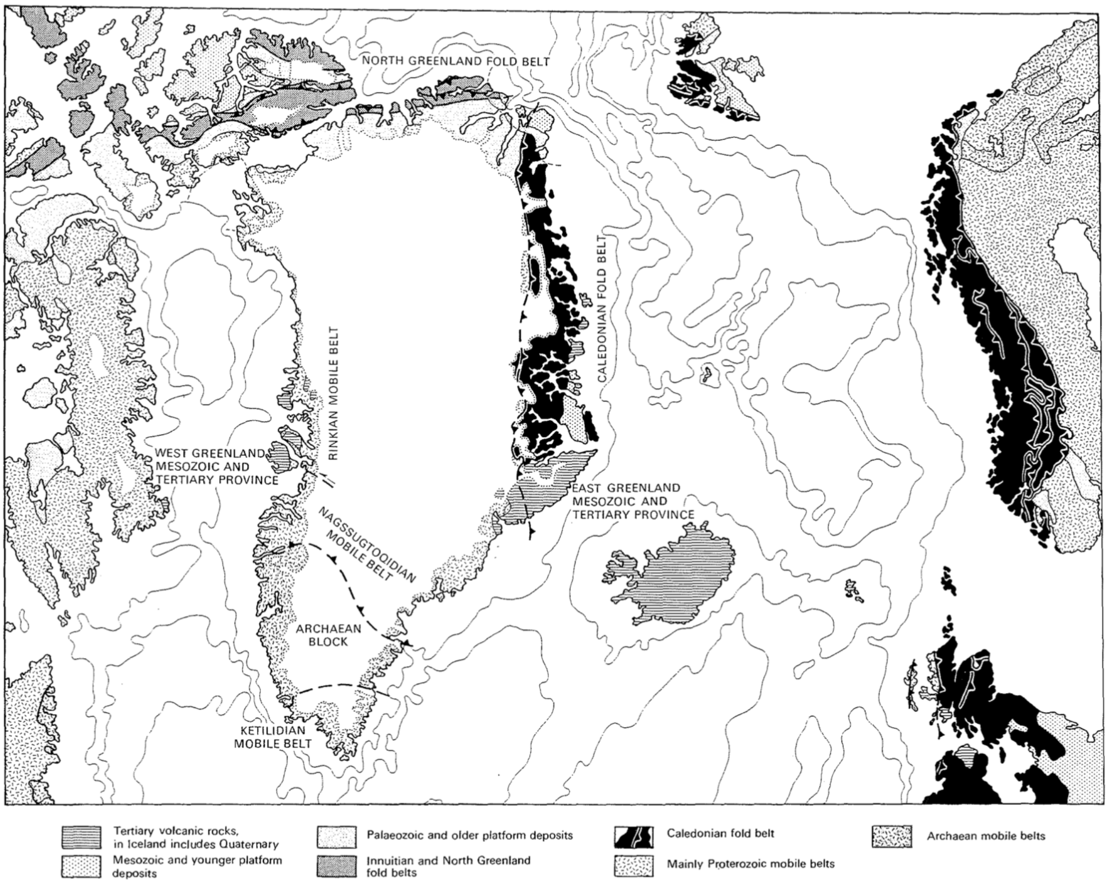

Figure 2.2: The two Paleozoic fold belts in Greenland. The Ellesmerian fold belt, represented as the North Greenland fold belt (dark grey), and the Caledonian fold belt in East Greenland (black). Figure obtained from Higgins et al. (2000).

During the Paleozoic (540-255 Ma), two major fold belts developed along the margins of the stable Precambrian shield (Henriksen et al., 2000). One of these fold belts is the Ellesmerian fold belt, which developed between Canada and North Greenland in Cambrian (540-485 Ma). The other fold belt of interest, the Caledonian fold belt, developed as a result of the collision between Laurentia and Baltica, when the Iapetus ocean closed in Silurian (445-420) (Higgins et al., 2000). The extent of these fold belts today can be seen in Figure 2.2. Because of the orogenic acitivities that was happening in Cambrian and Silurian, Greenland (Laurentia), Europe (Baltica) and North America were during Devonian (420-358 Ma) acting as one continent.

In latest Paleozoic, the orientation of the major plates changed. During Carboniferous to Permian time (358-250 Ma), rifting initiated between the Laurentian shield (Greenland) and the Baltic shield (Europe). This is illustrated in Figure 2.3, where the sea between Greenland and Norway opened up because of active sea-floor spreading.

In the Paleozoic-Mesozoic transition (250 Ma), North-East Greenland was dominated by regional subsidence and block faulting. A strike-slip zone called the deGeer Fracture Zone formed at the plate boundary between Greenland and Svalbard. This fault was connected to the separation of Greenland and Baltica, and led to a more localized basin formation in North-East Greenland during the late Jurassic and Cretaceous (163-66 Ma). The deGeer Fault separated Svalbard from North Greenland (Henriksen et al., 2000).

In the late Mesozoic (100-66 Ma; late Cretaceous), the stress field changed. This is also illustrated by Figure 2.3. Greenland was still separating from the Baltic shield East of Greenland and at the same time, rifting west of Greenland was initiated both in the Labrador sea and in Baffin Bay. Faults in this region were connected to a sinistral fault in Nares Strait North-West in Greenland (Tessensohn and Piepjohn, 2000). These faults were separating Greenland from the American Plate. The spreading ridges on the East and West side of Greenland got connected south of Greenland, and created a triple junction, causing the Greenland plate to move North, independently form the other big plates. This orientation continued into Early Cenozoic (66-58 Ma; Paleocene) (Laughton, 1975; Tessensohn and Piepjohn, 2000).

During the Cenozoic (66-0 Ma), the seafloor spreading west of Greenland ceased. Greenland was again part of the Laurentian plate, moving away from the Eurasian plate because the mid-Atlantic ridge to the east of Greenland (Laughton, 1975; Blinova, 2011). This is illustrated in Figure 2.4. Spreading with this geometry has continued to the present.

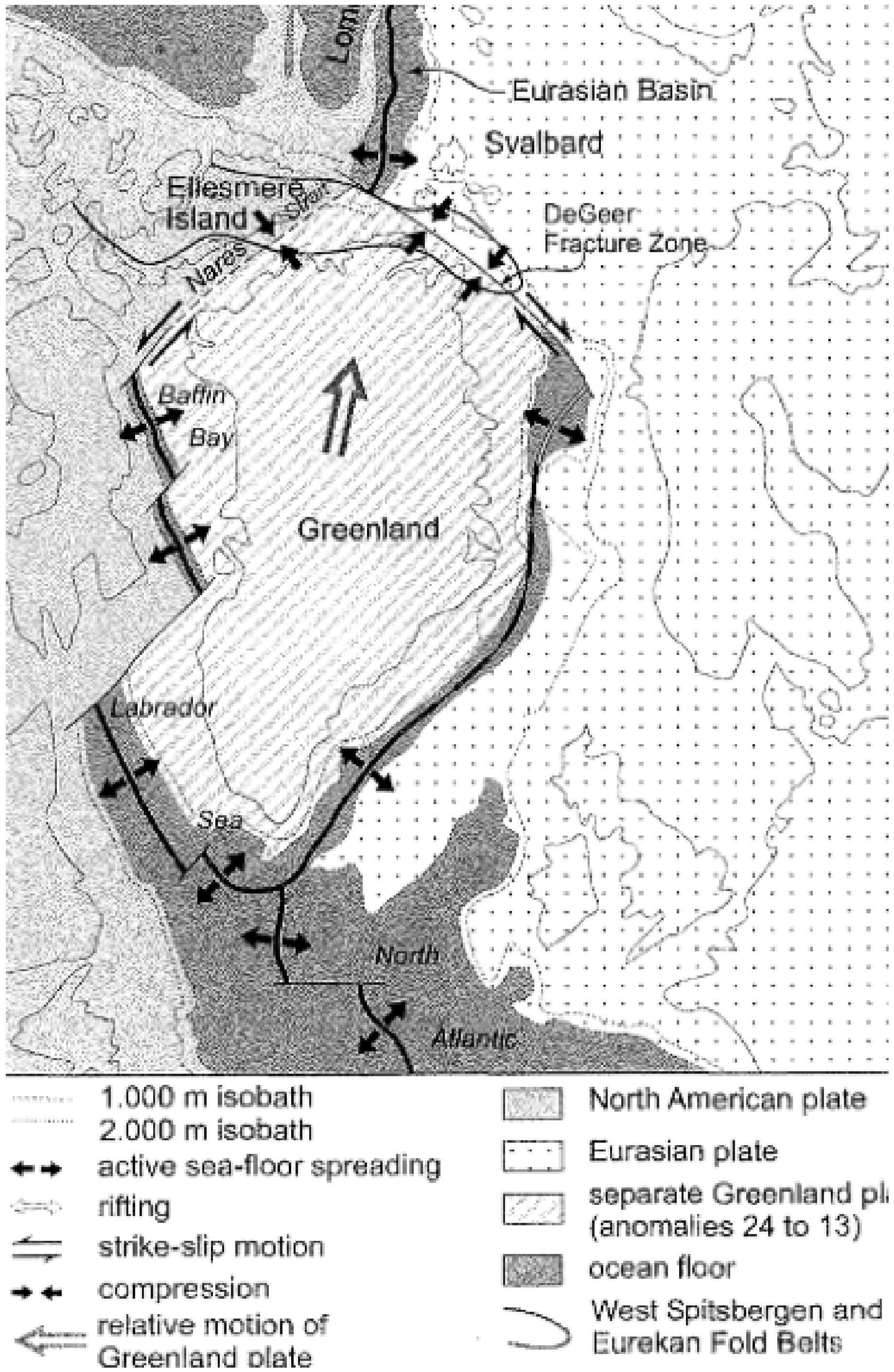

Figure 2.3: Tectonic motions between the latest Paleozoic and the earliest Cenozoic. Greenland was moving independently from the other plates. Figure slightly modified from Tessensohn and Piepjohn (2000).

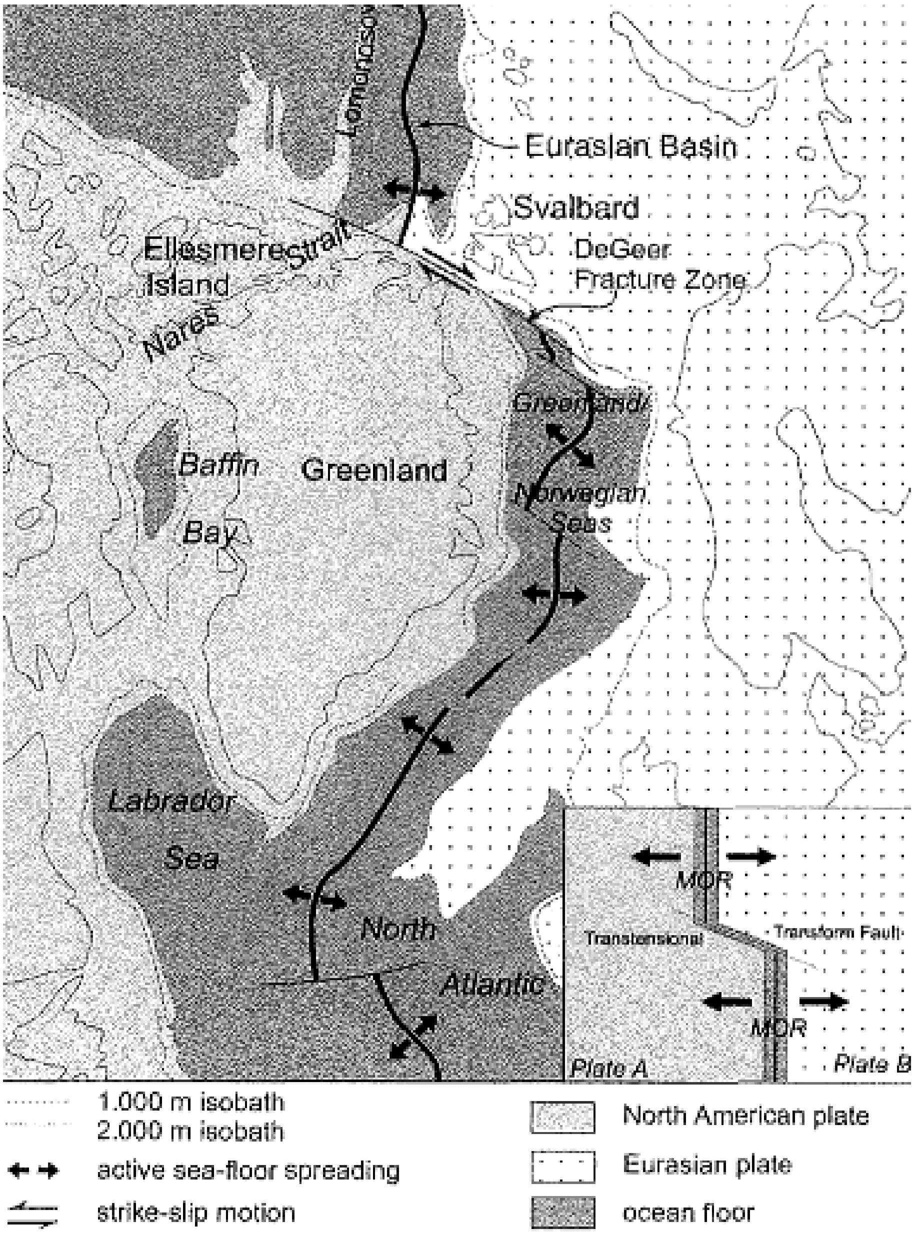

Figure 2.4: Tectonic motion after the Cenozoic. Again, Greenland was a part of the American Plate. Figure slightly modified from Tessensohn and Piepjohn (2000).

In the Quaternary (2.58-0 Ma), almost the entire surface of Greenland was covered by ice. After the last glacial period, the inland ice retreated and some ice free areas exist around the coastline today. It is possible study the geology in these areas and this has been done to some extent (Henriksen et al., 2000).

In North Greenland, the geology has been studied and mapped as the Franklinian basin and the Wandel Sea Basin. This can be seen from Figure 2.5, where most of North Greenland is represented in green and light green colors. According to the legend in Figure 2.5b this refer to the Franklinian Basin, with deposits from Cambrian to Silurian (540-420). Smaller parts in North Greenland are mapped as the Wandel Sea Basin, deposited in Carboniferous to Cretaceous (358-66 Ma).

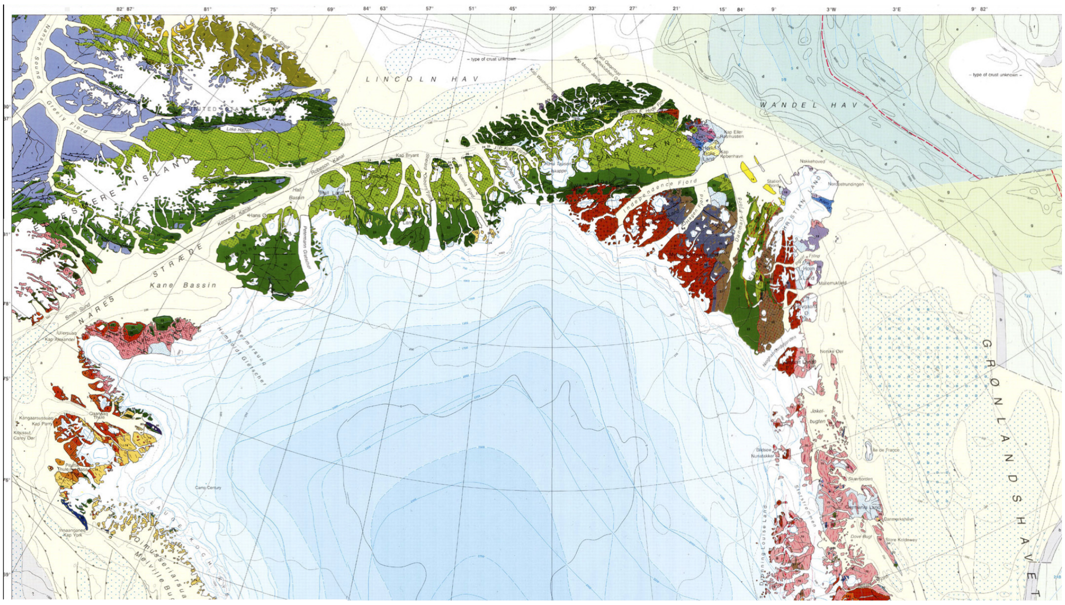

(a) Geological units in North Greenland

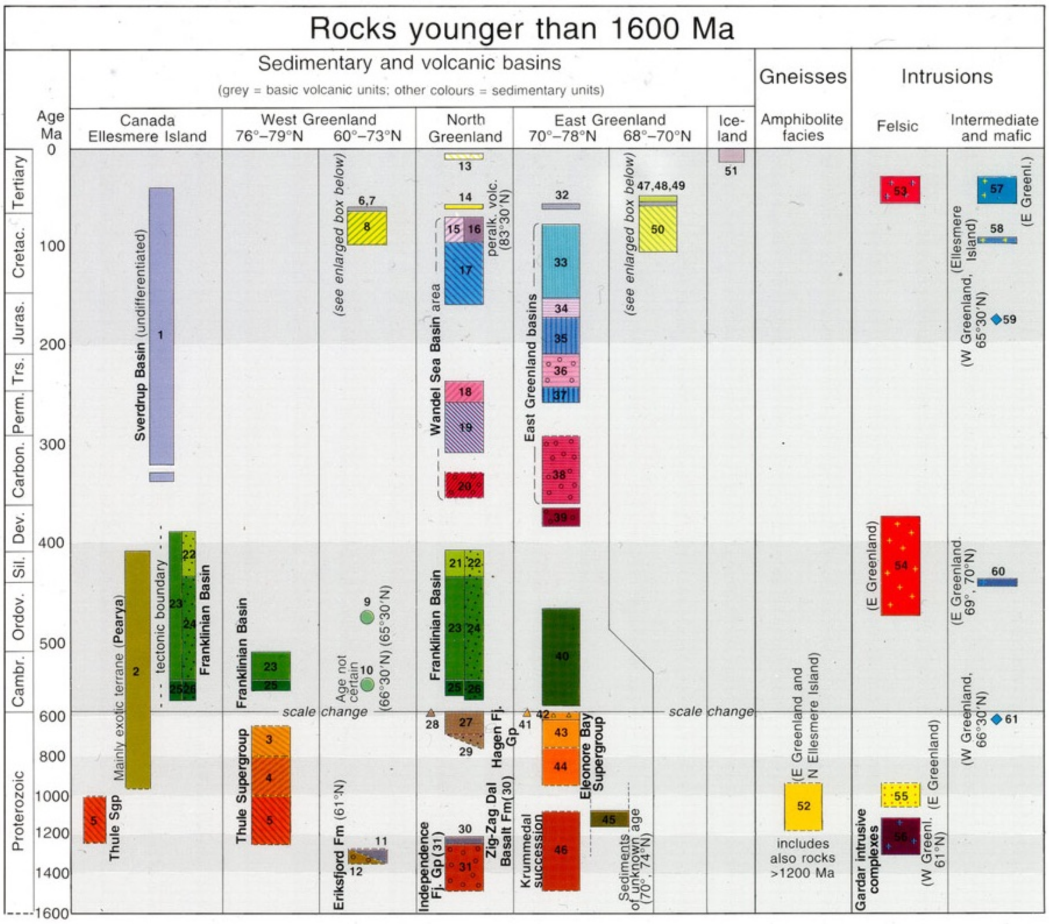

(b) Legend

Figure 2.5: Geological units in North Greenland. Map slightly modified from Henriksen et al. (2000).

2.2 Geology

2.2.1 The Franklinian Basin

The Franklinian basin was initiated by rifting between North Greenland and Canada. According to Henriksen and Higgins (2000), the basin developed as a passive margin in early Cambrian, as the oldest exposed deposits in the basin are of this age. The 2000 km long basin extends from the Canadian Arctic Islands across North Greenland to Kronprins Christian Land (Henriksen et al., 2000). Figure 2.6 shows the extension of the basin, colored in green.

Figure 2.6: Extension of the Franklinian Basin across Canada and North Greenland colored in green. Slightly modified from Rosa et al. (2016).

Deposition in this basin went on for a long time and was brought to a close by the Ellesmerian orogeny in Devonian (419-358 Ma). The basin deposits are divided in deep water through and shelf sediments (Dahl-Jensen et al., 2003).

The boundaries of the basin is of interest, but the only boundary that still remains is the southernmost boundary with deposits from the Proterozoic. This is a 2 km thick sandstone succession called the Independence Fjord Group and the Zig-Zag Dal basalt formation. The basalts are from the middle Proterozoic and are conformably overlying the Independence Fjord

Group (Henriksen and Higgins, 2000).

Later deposits in the area further east are recognized as the Wandel Sea Basin, a postorogenic sequence in the junction between the two Palaeozoic orogens (Håkansson and Stemmerik, 1989; Stemmerik et al., 1998).

2.2.2 The Wandel Sea Basin

The Wandel Sea Strike-Slip Mobile Belt is a dextral transpression zone in North-East Greenland where areas of local compression are found. This is illustrated in Figure 2.7. A fault system known as the Trolle Land Fault System (TLFZ) developed when the break-up between Laurentia and Eurasia commenced in Carboniferous (358-298 Ma). The deposits from this break-up are colored gray in Figure 2.7, and named the Wandel Sea Basin. This is an area with where sediment basins are dominating (Håkansson and Pedersen, 2001).

2.3 Seismicity

The seismicity of North Greenland is poorly known because few seismic stations have been in operation in this area. In addition, the magnitudes of the earthquakes in the region are small. This makes it difficult to obtain good seismic data. Greenland is not located at a plate boundary; therefore, the seismic activity in the area is low.

According to Kanao et al. (2015), some seismicity related to deglaciation has been reported from different regions in the Arctic, this includes the continental margins of northern Greenland. The small earthquakes that are generated in Greenland are considered to be a result of tectonic motions, which are either vertical motions (uplift) due to isostasy and/or plate tectonic motions due to the oceanic ridge west of Greenland. Only a few fault plane solutions are available in North Greenland, because the earthquakes are so small and

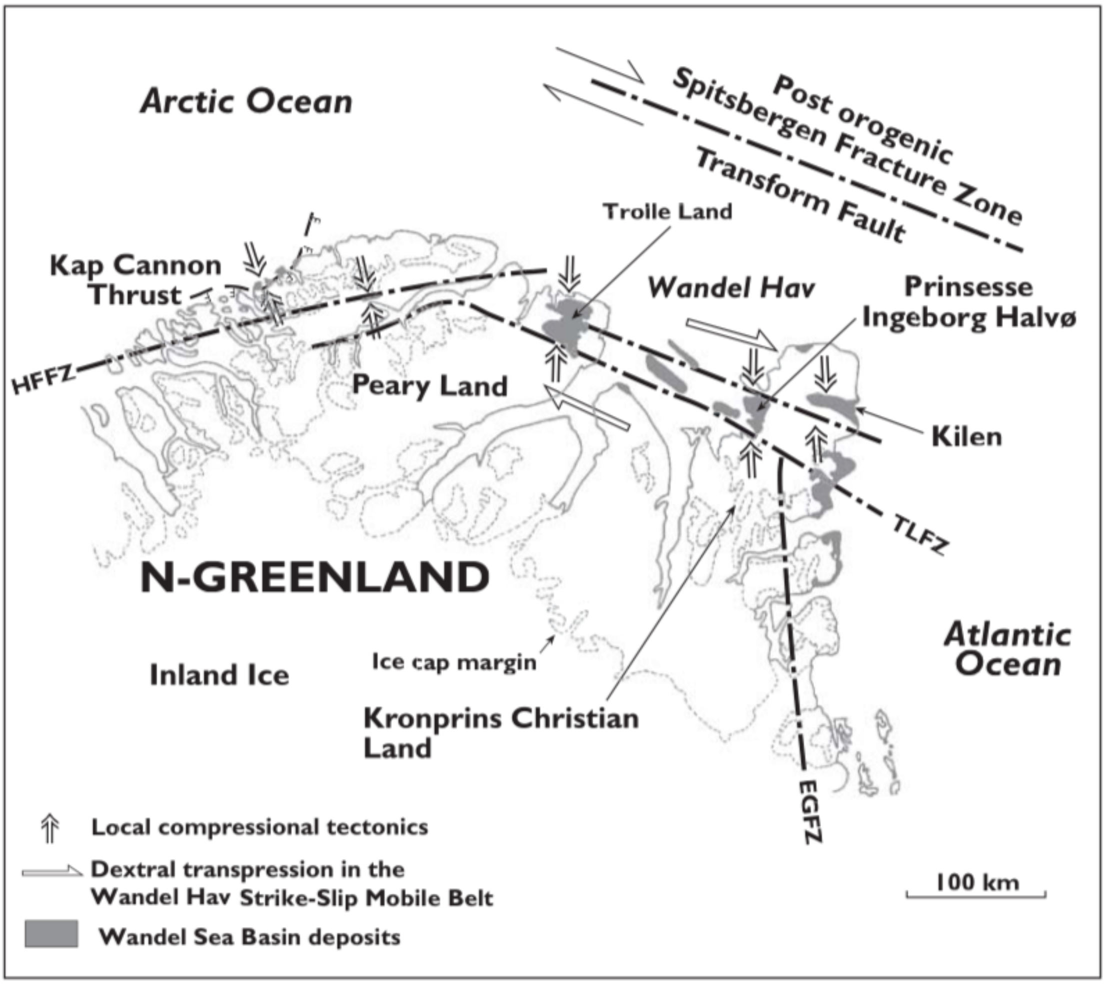

Figure 2.7: Deposits in the Wandel Sea Basin colored in gray. Figure obtained from Håkansson and Pedersen (2001).

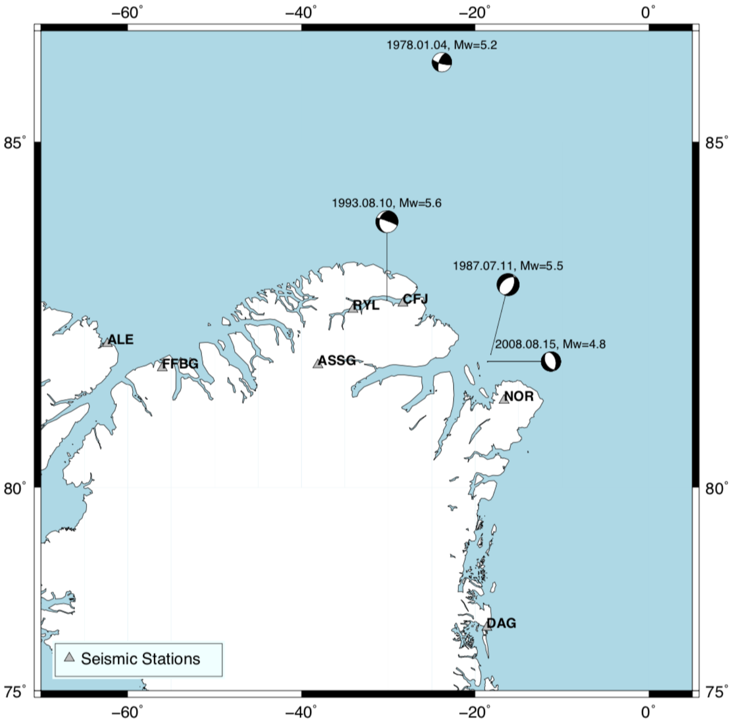

Figure 2.8: Focal Mechanisms from the GMT catalog. The search criteria for the focal mechanisms was $80 < latitude < 90$ and $-80 < longitude < -10$. Origin time and moment magnitude is shown above the focal mechanisms.

only visible at a few stations. This makes it difficult to assess the main cause of the intraplate earthquakes (Larsen et al., 2014; Gregersen, 1982).

From the Global CMT Catalog (Dziewonski et al., 1981; Ekström et al., 2012), only four fault plane solutions are found in the study region of this thesis, since the start of the catalog in 1976. These are plotted in Figure 2.8. The lack of focal mechanisms limits the possibility to understand the tectonic stress field that causes the earthquakes. To better understand the seismicity in the area, many more fault plane solutions and earthquake locations are required (Gregersen, 1982). The fault plane solutions from 1978 and 1993 represent compression in the N-S direction or tension in the E-W direction. The solutions from 1987 and 2008 have near vertical planes, resulting in pure normal faulting.

3. Data

3.1 Stations

The seismic data presented in this thesis are obtained from four temporary and five permanent stations. The four temporary stations (ASSG, CFJ, FFBG and RYL) are located in North Greenland, in the study area of this thesis. There are many permanent stations in Greenland, but only three of them are included in this thesis (SUMG, DAG and NOR). One permanent station in Canada (ALE) and one station located in Svalbard (KBS) are also included. Table 3.1 gives an overview of the seismographs used in this thesis and Figure 3.1 shows where they are located.

The seismic data from these stations were extracted from GEUS (The Geological Survey of Denmark and Greenland), IRIS (Incorporated Research Institutions for Seismology) and GFZ (German Research Centre for Geosciences). Table 3.2 shows where the data were obtained from.

The main time periods with data are from the 1st of July to the 31st of December for 2004, 2005 and 2006. For 2007, the data are mainly from the 1st of January to the 30th of June. The time periods were chosen based on when most of the stations were operating. Due to weather conditions and loss of power, the temporary stations did not run continuously throughout the four years.

The power supply to the stations was a combination of wind power, sun power and batteries. The region is very remote and has changing weather conditions. GEUS only went to the stations each summer, to repair and collect data. If something happened to the stations in between the visits, the stations might not record data. Heavy winds often broke the windmills,

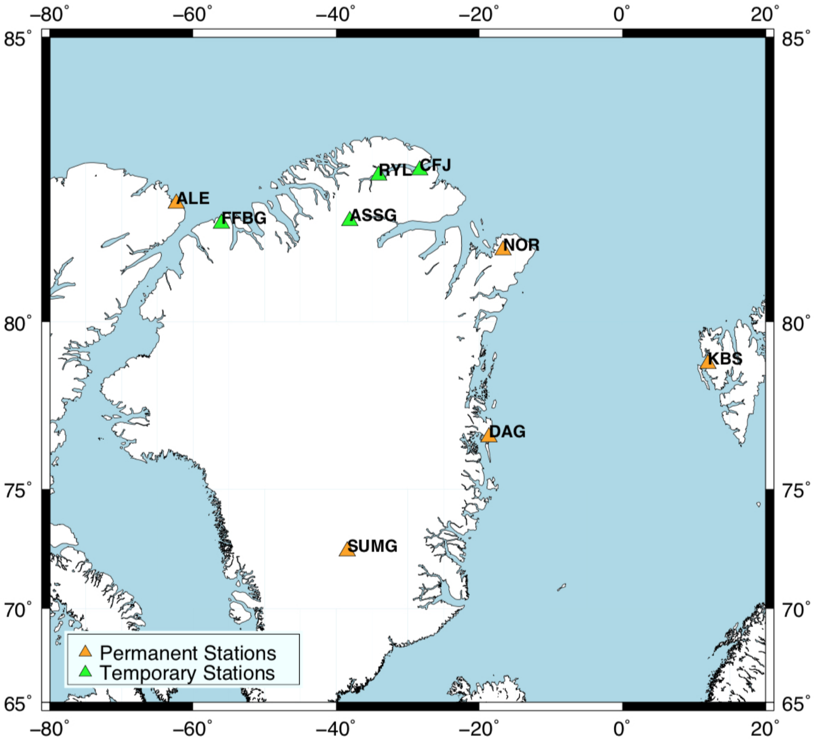

Figure 3.1: Seismic stations in Greenland, Canada and Svalbard. Temporary stations are shown in green and permanent stations are orange.

Station Code	Latitude°	Longitude°	Elev.(m)	Network	Operation
ALE	82.500	-62.350	60	II	1990-
ASSG	82.176	-38.108	318	DK	2004-2005
CFJ	83.084	-28.321	60	DK	2005-2007
DAG	76.771	-18.655	23	GE	1998-
FFBG	82.130	-56.036	30	DK	2004-2006
KBS	78.915	11.938	90	GE	1994-
NOR	81.600	-16.683	36	DK	2002-
RYL	83.000	-34.072	3	DK	2006-2007
SUMG	72.575	-38.460	3240	GE	2000-

Table 3.1: Seismic stations used in this thesis. If no end year is listed, the station is still in operation.

	2004	**2005**	**2006**	**2007**
ALE	GEUS	GEUS	IRIS	IRIS
ASSG	GEUS	GEUS		
CFJ		GEUS	GEUS	GEUS
DAG	GFZ	GEUS	GFZ	GFZ
FFBG	GEUS	GEUS	GEUS	
KBS	GEUS	GEUS	GEUS	
NOR	GFZ	GFZ	GFZ	GFZ
RYL			GEUS	GEUS
SUMG	GEUS	GEUS	GFZ	GFZ

Table 3.2: Overview of where the different data files were obtained from. A blank box means that there are no data available.

cutting off the wind power supply. Also, the study area is above a latitude of 80°N, so dark polar nights are also a challenge, limiting the use of the solar panels. Each station was also equipped with batteries (300Ah each). These were mainly charged by solar energy during the summer and then they supplied the stations with energy when the sun disappeared. In the middle of the winter, the batteries often ran out of power and were not recharged until the sun got back in the spring. As most of the stations were out of power by December, the time periods with data are mainly summer and fall.

Table 3.3-3.6 shows the operation periods for the stations during the four years. It can be seen from Table 3.6 that almost no data was obtained from the temporary stations during 2007, probably because the stations were out of power. The stations were collected by GEUS in the summer of 2007 which is the reason for using the time period between January and July for that year, even though almost no data are available.

Station Code	**Start Date**	**End Date**	**Duration**
ALE	01.07.2004	31.12.2004	183
ASSG	24.07.2004	18.11.2004	117
CFJ	-	-	0
DAG	01.07.2004	31.12.2004	183
FFBG	28.07.2004	02.11.2004	97
KBS	01.07.2004	03.07.2004	3
	05.07.2004	30.08.2004	56
	07.09.2004	14.09.2004	7
NOR	01.07.2004	31.12.2004	183
RYL	-	-	0
SUMG	01.07.2004	09.07.2004	8
	14.07.2004	31.12.2004	170

Table 3.3: Operation period for the seismic stations during 2004. The temporary stations are shown in bold font.

Station Code	**Start Date**	**End Date**	**Duration**
ALE	01.07.2005	31.12.2005	183
ASSG	18.07.2005	07.10.2005	81
	18.10.2005	29.11.2005	42
CFJ	16.07.2005	14.10.2005	90
DAG	01.07.2005	23.11.2005	145
	06.12.2005	31.12.2005	25
FFBG	18.07.2005	29.09.2005	73
KBS	01.07.2005	31.12.2005	183
NOR	01.07.2005	11.12.2005	163
RYL	-	-	0
SUMG	01.07.2005	31.12.2005	183

Table 3.4: Operation period for the seismic stations during 2005. The temporary stations are shown in bold font.

Station Code	Start Date	End Date	Duration
ALE	01.07.2006	31.12.2006	183
ASSG	-	-	0
CFJ	10.07.2006	29.11.2006	142
DAG	01.07.2006	31.08.2006	61
	03.09.2006	31.12.2006	119
FFBG	24.07.2006	04.11.2006	103
KBS	01.07.2006	18.12.2006	170
NOR	01.07.2006	31.08.2006	61
	05.12.2006	31.12.2006	26
RYL	15.07.2006	11.10.2006	88
SUMG	01.07.2006	31.12.2006	183

Table 3.5: Operation period for the seismic stations during 2006. The temporary stations are shown in bold font.

Station Code	Start Date	End Date	Duration
ALE	01.01.2007	30.06.2007	180
ASSG	-	-	0
CFJ	19.03.2007	20.03.2007	1
	25.03.2007	05.04.2007	11
	08.04.2007	12.05.2007	34
DAG	01.01.2007	30.06.2007	180
FFBG	-	-	0
KBS	-	-	0
NOR	01.01.2007	30.06.2007	180
RYL	05.03.2007	07.03.2007	2
SUMG	-	-	0

Table 3.6: Operation period for the seismic stations during 2007. The temporary stations are shown in bold font.

3.2 Analyzing the Data

The data was processed with the SEISAN analysis software (Havskov and Ottemoller, 1999). The continuous raw data from the vertical component of the seismographs were scanned manually and interesting events were marked and further analyzed.

3.2.1 Continuous Data

One station was chosen for continuous scanning each year. The scanning was done manually, where one window contained two hours of data and a band-pass filter was applied, where frequencies between 3-8 Hz were included. For periods where the signal-to-noise ratio (SNR) was either high or low, the amplitude ratio was either enhanced or reduced, respectively, by applying other filters.

Figure 3.2a and 3.2b show how the seismograms are represented if the SNR is poor (high or low). It is desirable to have seismograms with a suitable SNR. An example where the SNR is good and also where an interesting event is visible, is shown in Figure 3.2c. This is a time window showing the seismogram from the vertical component from the CFJ station, with a time window from 07:41 to 09:41 in the morning of the 25th of July 2005. It is clear that something happens on the 09:07-line and this is the types of events that were marked and assumed to be earthquakes. In the same figure, the wiggles on the rest of the seismogram show a desirable SNR.

3.2.2 Analyzing Events

After scanning through the continuous data for one station for each of the four years, the events that were marked got analyzed further. When marked, the events got a time stamp making it possible to find the same event on the

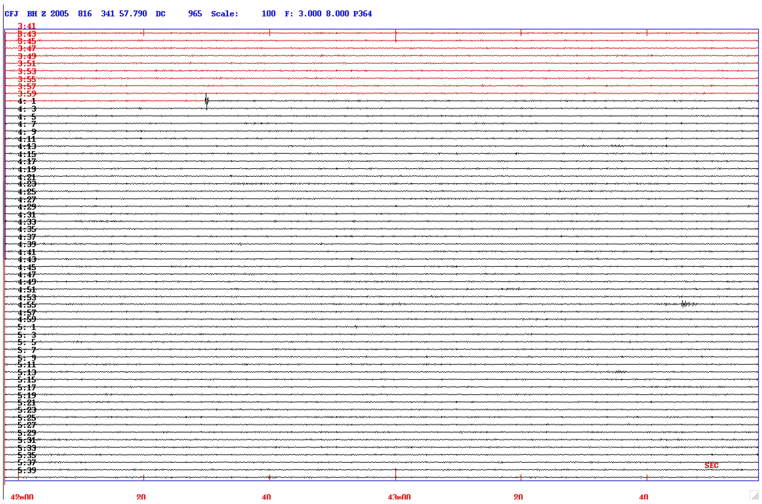

(a) High SNR

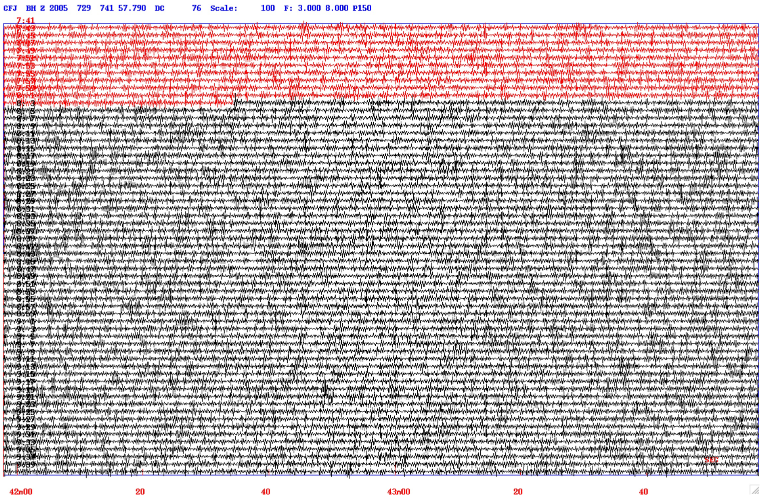

(b) Low SNR

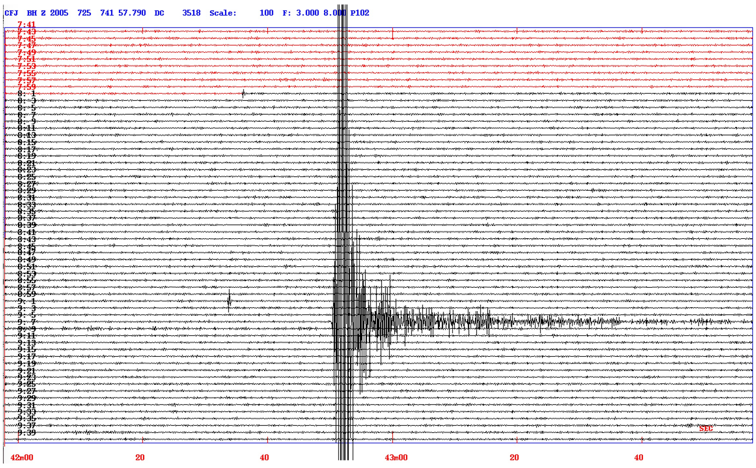

(c) Good SNR and an interesting event

Figure 3.2: Examples of seismograms with different signal-to-noise ratio (SNR). a) shows high SNR where the signals are barely seen. In b) the SNR is low. It is difficult to see if there is a wanted signal in between all the noise. c) shows a good SNR and an interesting event. The seismograms are obtained from the CFJ station.

seismograms for all the stations. This was done to see if the same event was recorded at several stations. For this process, two different filters were used, depending on which filter showed the signals more clearly. One filter was set to 1-5 Hz and the other filter was set to 5-9.9 Hz.

The events had to be visible in the seismograms of at least three different seismic stations to be analyzed in more detail, to secure an accurate location when locating the earthquakes later. An example of the analysis process is shown in Figure 3.3, which is the same event that was shown in the continuous data in Figure 3.2c. The station names are shown to the left of the seismograms. Figure 3.3a shows the seismograms for the stations before applying any filter and it can be seen that it is hard to detect the event at any of the other stations than CFJ. In Figure 3.3b and 3.3c are the same seismograms shown, but the two band-pass filters are now applied. The event is clearly seen with both filters, but it is more clear when filtering with the higher band-pass filter (5-9.9 Hz). Therefore, this filter was applied when picking the phases for this particular event. Figure 3.3d is included to show this process. The first arrival, the P-phase, was picked on the vertical component and the S-phase was picked on one of the horizontal components. This was done to all the events that were marked in the scanning process.

3.2.3 Locations

It was desirable to use the picked P-and S-phases to invert for the hypocenters and this process is based on the travel times originated from at least three P-phases and one S-phase. Due to the knowledge of the tectonic processes in the region, the earthquakes were forced to not locate below Moho. In the location process it was beneficial to get an RMS-value as low as possible, to minimize the error in the location estimates.

The Velocity Model used in the location process was the one layer Greenland Velocity Model, shown in Table 3.7. This is not a local velocity model for the area, but a general velocity model used to locate earthquakes in all of

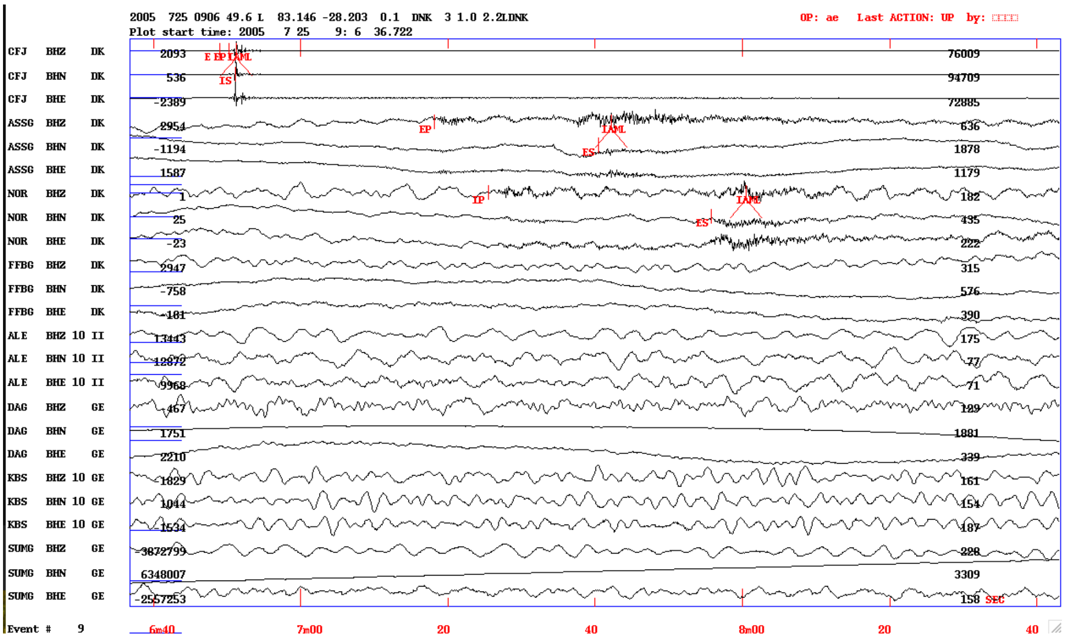

(a) No filter

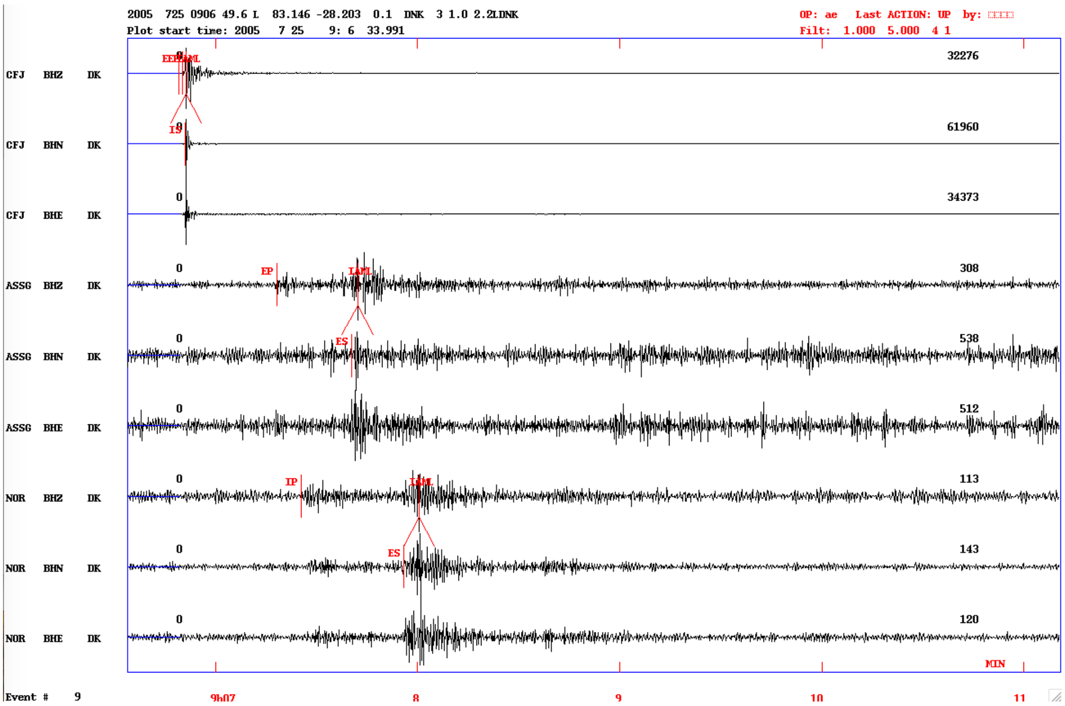

(b) Filter: 1-5 Hz

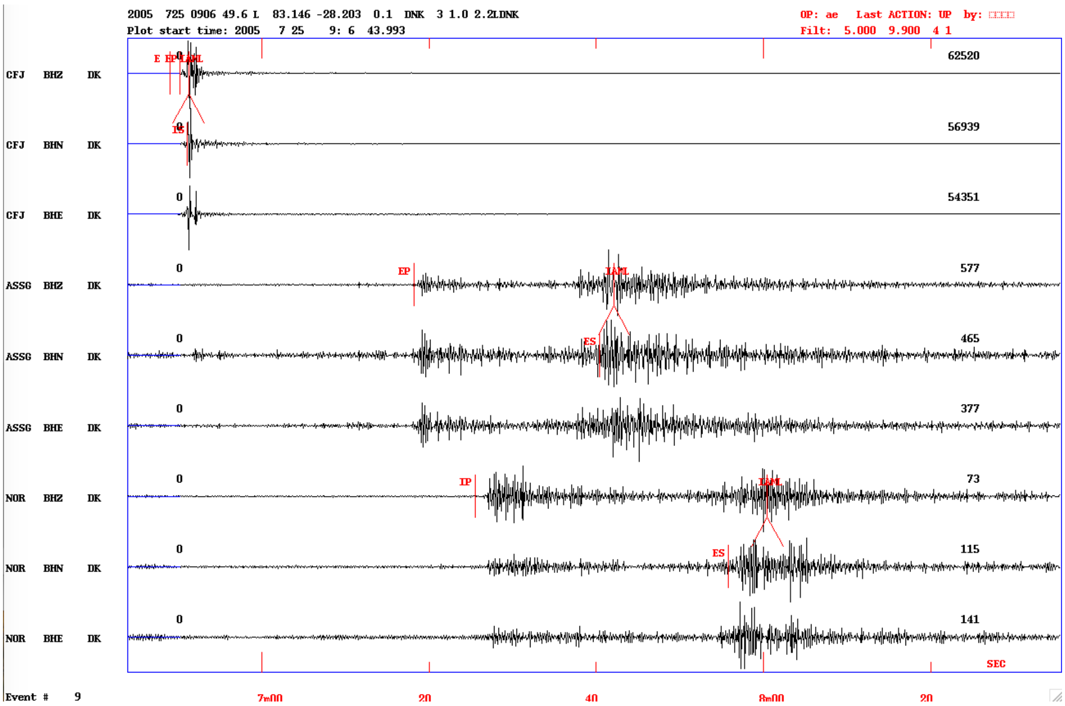

```
2005  725 0906 49.6 L  83.146 -28.203  0.1  DNK  3 1.0 2.2LDNK
Plot start time: 2005   7 25    9: 6  43.993
```

```
OP: ae   Last ACTION: UP   by: □□□□
Filt:  5.000  9.900  4 1
```

(c) Filter: 5-9.9 Hz

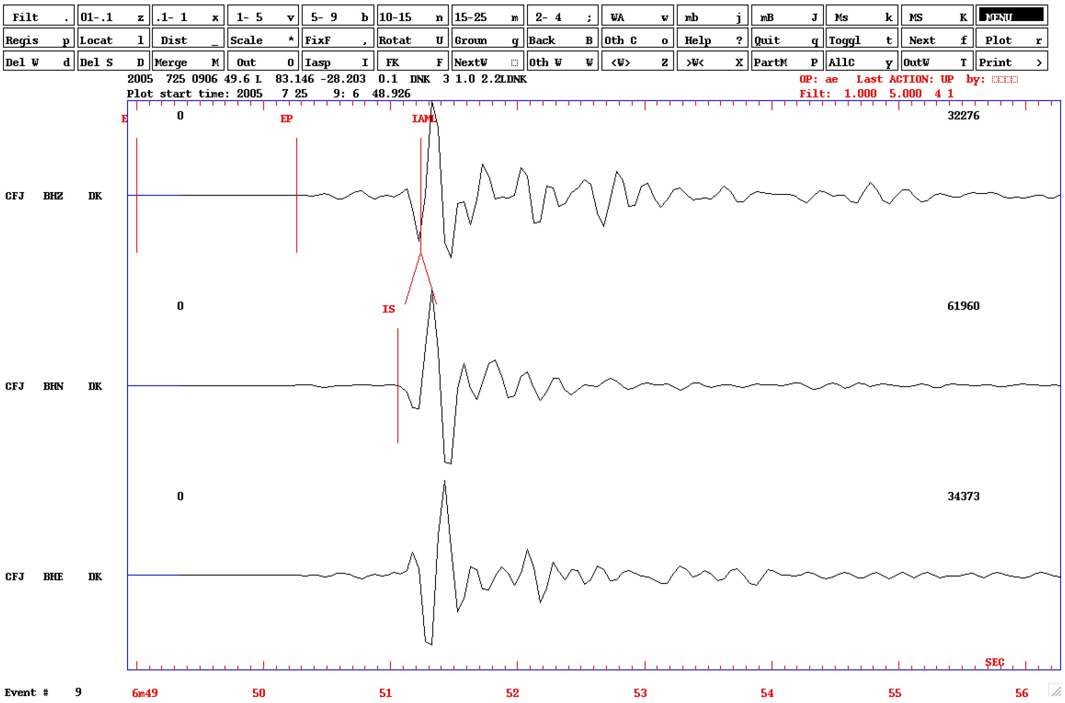

```
2005  725 0906 49.6 L  83.146 -28.203  0.1  DNK  3 1.0 2.2LDNK
Plot start time: 2005   7 25    9: 6  48.926
```

```
OP: ae   Last ACTION: UP   by: □□□□
Filt:  1.000  5.000  4 1
```

(d) Phase picking example

Figure 3.3: Figures showing the process of analyzing events picked from the continuous scanning. a) shows the seismograms before any filters are applied. b) and c) shows the same seismograms with different filters. d) shows an example of where on the seismograms the phases are picked.

Vp [km/s]	**Depth [km]**	
6.2	0	
8.2	36	Moho
8.5	80	

Table 3.7: The Greenland Velocity Model. One layer above Moho.

Greenland. When the events were located, the study area was restricted to a latitude of 80°N and 90°N and a longitude of 80°W and 10°W. The 42 earthquakes were located in this region during the four years and the locations are shown as yellow dots in Figure 3.4. The estimated depths for the earthquakes are shown in Figure 3.5, where it is seen that the earthquakes mostly have a shallow origin and a lot of the events appear to originate at the surface. It would be interesting to see if the depth of these earthquakes changes if relocated with a different velocity model. More detailed information about each individual event is presented in Table 3.8.

3.2.4 Magnitudes

Local magnitudes were estimated for the 42 earthquakes. This was done by finding the biggest amplitude-peak in the recoded S-wave train on the vertical component, using the Wood Anderson filter. The equation for calculating the local magnitude is represented below.

$$Ml = log(A) - a * log(dist) - b * dist - C, \tag{3.1}$$

where A is the amplitude that is picked and the difference in arrival time between the P- and S-waves is used to correct for the distance between the source and the receiver. The letters a and b are distance attenuation coefficients and are assumed to be the same for all event in the same region.

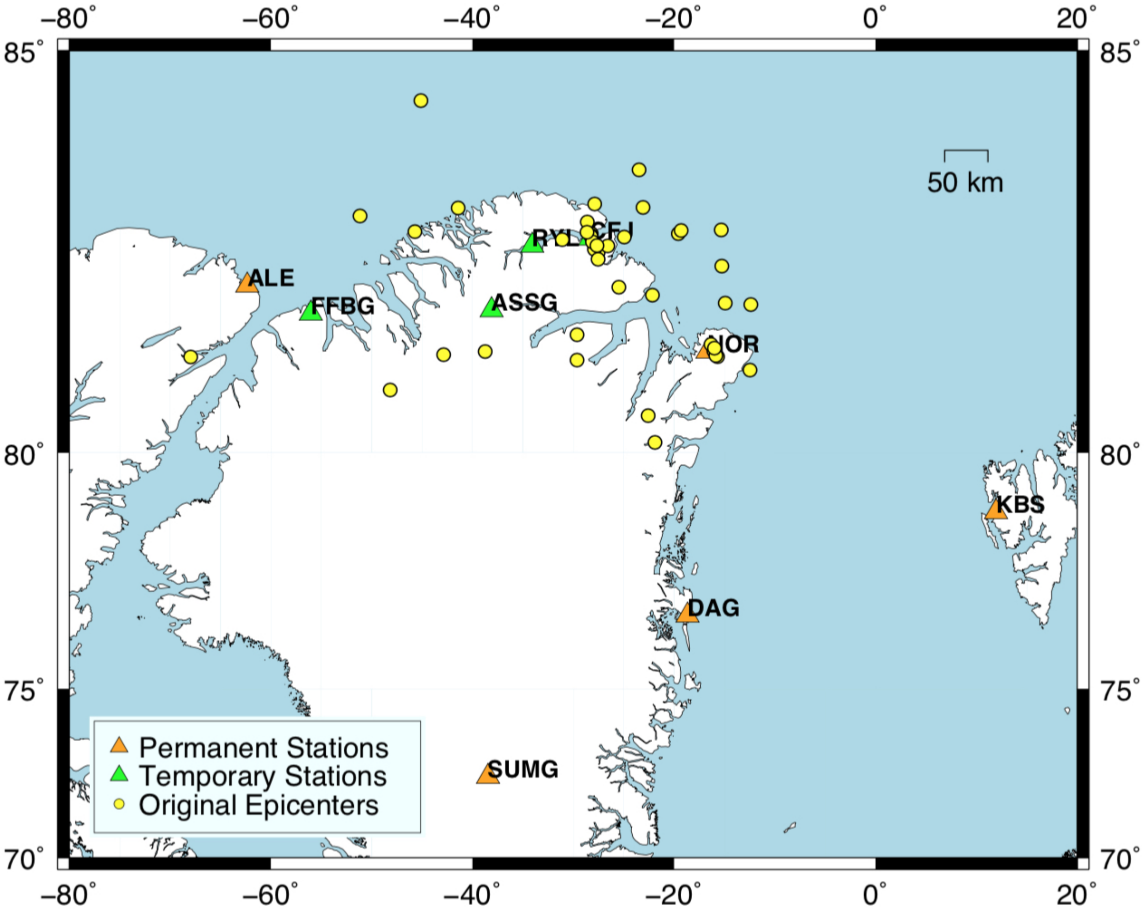

Figure 3.4: Earthquakes recorded in the study area between 2004-2007.

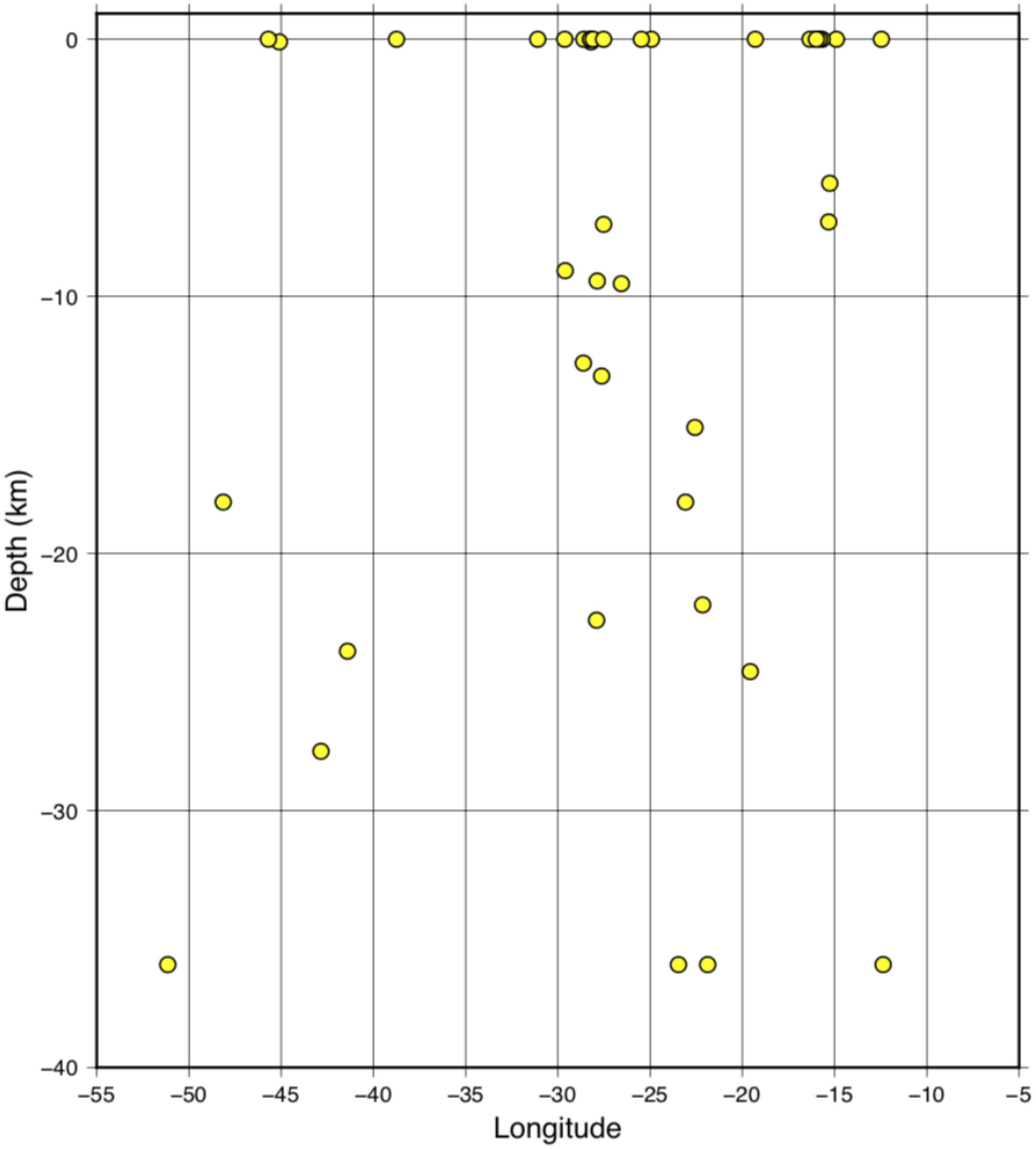

Figure 3.5: Earthquake depths for the epicenters shown in Figure 3.4.

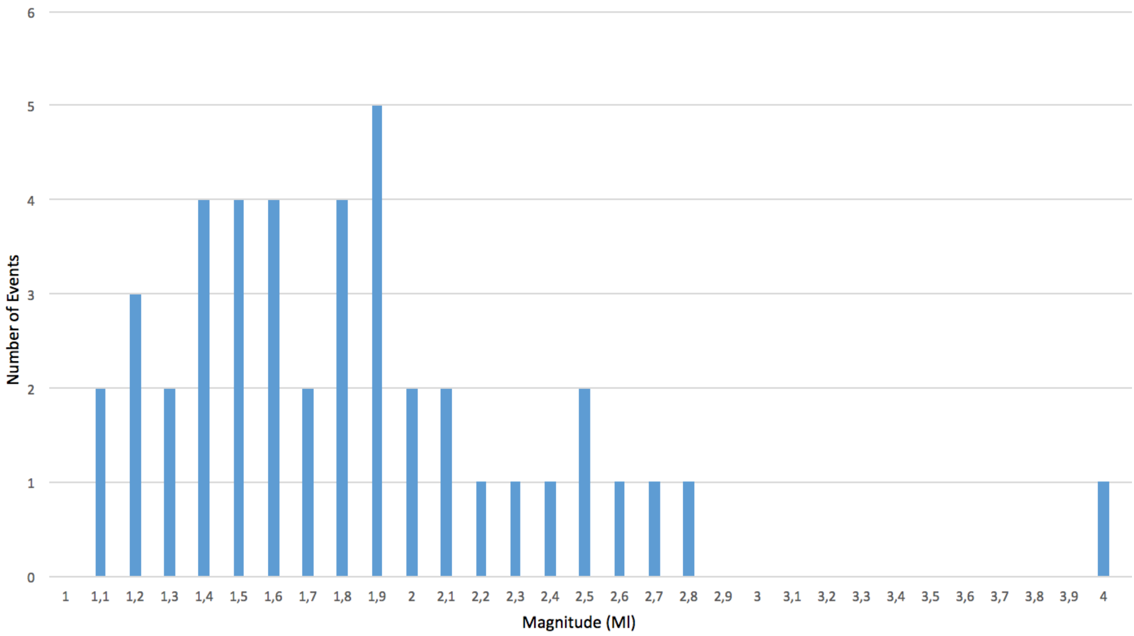

Figure 3.6: Magnitude distribution of the 42 earthquakes.

C is a constant that is dependent on the magnitude of the earthquake and is calculated by determining a reference distance and fixing the magnitude assumed to correspond to that distance (Havskov and Ottemoller, 1999).

The magnitudes obtained in North Greenland range from 1.1 to 4.0, shown in Figure 3.6. It is clear that the magnitude of the earthquakes in this region are rather small, but the events were still detected at three or four different stations.

Event	Date	Origin Time	Latitude	Longitude	Depth	RMS	Ml
1	2004.07.27	23:27	83.337	-51.151	36.0	1.5	1.7
2	2004.08.15	09:45	80.165	-21.881	36.0	0.6	1.4
3	2004.08.23	06:51	81.555	-42.839	27.7	1.2	1.1
4	2004.08.24	19:59	81.328	-12.462	0.0	1.8	1.7
5	2004.08.28	12:21	82.918	-27.516	7.2	1.1	2.6
6	2004.08.30	13:48	81.520	-67.970	18.1	2.9	1.9
7	2004.09.01	01:16	81.472	-29.623	0.0	1.3	1.4
8	2004.09.03	10:57	80.617	-22.565	15.1	0.3	1.6
9	2004.09.12	15:18	81.839	-29.609	9.0	1.3	2.7
10	2004.10.14	12:13	84.551	-45.104	0.1	1.3	1.9
11	2004.10.17	00:39	83.104	-24.929	0.0	1.0	2.4
12	2004.11.09	23:54	83.073	-31.090	0.0	1.5	2.0
13	2004.11.13	05:35	81.022	-48.145	18.0	1.9	1.6
14	2005.07.18	04:05	83.440	-41.405	23.8	0.2	1.8
15	2005.07.23	07:16	82.958	-27.897	22.6	0.8	1.2
16	2005.07.25	09:06	83.146	-28.203	0.1	1.0	1.9
17	2005.08.02	03:10	83.122	-28.218	0.0	1.0	1.4
18	2005.08.02	13:15	82.998	-26.560	9.5	0.5	1.4
19	2005.08.11	11:11	83.282	-28.589	0.0	1.1	1.9
20	2005.08.11	22:19	83.111	-28.241	0.0	0.7	1.3
21	2005.08.20	19:30	83.047	-28.096	0.0	0.7	1.6
22	2005.08.26	17:08	82.270	-14.902	0.0	1.0	1.5
23	2005.08.29	20:36	83.002	-27.627	13.1	1.3	1.2
24	2005.08.30	17:34	81.526	-15.680	0.0	1.1	4.0
25	2005.09.03	16:37	81.608	-16.037	0.0	0.1	1.5
26	2005.09.07	14:01	81.541	-15.833	0.0	1.4	1.6
27	2005.09.14	07:52	81.703	-16.325	0.0	1.2	1.8
28	2005.09.27	00:41	82.833	-27.523	0.0	0.4	2.5
29	2005.09.27	06:13	83.485	-27.863	9.4	0.9	2.8
30	2005.10.03	20:42	81.598	-38.746	0.0	1.7	1.3
31	2005.10.06	10:36	83.187	-15.321	7.1	0.4	1.5
32	2005.10.06	20:18	82.376	-22.149	22.0	0.4	1.2
33	2005.10.07	05:58	83.143	-19.570	24.6	0.2	2.1
34	2006.07.12	10:58	82.480	-25.479	0.0	0.8	1.9
35	2006.07.26	08:32	83.161	-28.618	12.6	0.1	2.1
36	2006.07.30	14:48	81.648	-15.986	0.0	1.6	2.0
37	2006.08.06	15:36	83.860	-23.456	36.0	3.0	1.5
38	2006.09.15	14:55	82.253	-12.372	36.0	1.5	2.3
39	2006.09.30	09:27	82.749	-15.257	5.6	1.2	2.2
40	2006.10.04	04:44	83.182	-19.297	0.0	0.7	2.5
41	2006.10.06	00:07	83.448	-23.082	18.0	1.2	1.8
42	2006.11.12	08:00	83.167	-45.694	0.0	0.6	1.8

Table 3.8: Date, origin time, latitude, longitude, depth, RMS error and magnitude for each of the 42 events found in the study area between 2004 and 2007.

4. Method

4.1 Relocation

Accurate estimation of earthquake locations is a widely known problem in seismology. Locations are obtained by inverting the observed data, which is why an uncertainty in the result is present. It is important with good location estimations to understand the fault orientations and the tectonic activity around the Earth. The choice of velocity model in the location process has a big impact on the resulting locations. The earthquakes are relocated if the velocity model is replaced. Information about the crustal structure in the area where earthquakes are located is important.

4.1.1 Relocation with Synthetic Tests

Synthetic testing is a way to validate or check the robustness of the solutions obtained in an inversion process. In this thesis, synthetic tests were performed to show that locating earthquakes with different velocity models give very different results. For convenience, the earthquakes found in North Greenland between 2004 and 2007 were used. In theory, any set of earthquakes could be used to perform the same tests.

The set of earthquakes was located by inverting the travel times recorded at the seismic stations and some estimated locations were then obtained. A slightly modified version of the velocity model for South-Western Norway was used for convenience (Havskov and Bungum, 1987). This velocity model is shown in Table 4.1. The locations obtained are referred to as *observed epicenters* and plotted as yellow circles in Figure 4.1. These locations are assumed to be the correct locations in the following synthetic tests.

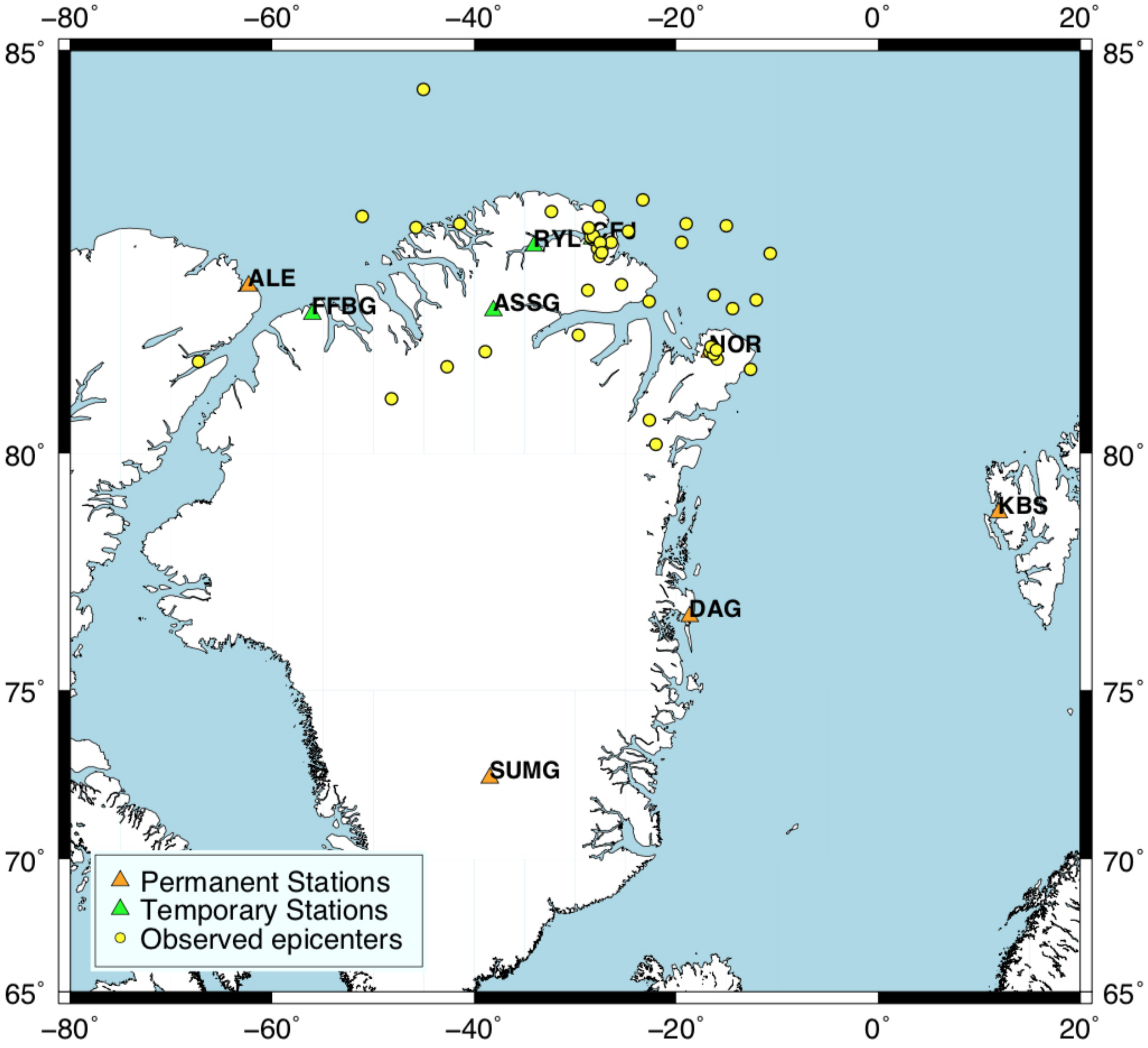

Figure 4.1: Earthquakes recorded in the study area between 2004-2007, located with the velocity model for South-Western Norway (Table 4.1).

Vp [km/s]	**Depth [km]**	
6.2	0	
6.2	12	
7.1	23	
8.05	31	Moho
8.25	50	
8.5	80	

Table 4.1: Velocity Model for South-Western Norway

When performing the synthetic tests, it is assumed that the crustal structure of the area is known and that the starting (observed) locations are correct. The synthetic tests were performed with the following procedure:

1. **Forward synthetic modeling.** When the locations (m) and the crustal structure (A) are known, forward modeling can be performed to calculate the travel times (d). This is illustrated in Equation 4.1,

$$d = Am. \tag{4.1}$$

2. **Inversion.** Next, it is assumed that the travel times (d) obtained are correct. The travel times are then used to invert for new locations (m') and a choice of velocity model (A) is required. By modifying Equation 4.1, this is illustrated by the expression:

$$m' = [A^T A]^{-1} A^T d. \tag{4.2}$$

The new locations obtained (m') can then be compared to the old locations (m) to check the quality of the velocity model chosen in the inversion. If the correct velocity model for the area was used, the new locations are equal to the old locations ($m = m'$). If the velocity model chosen was a weak representation of the crustal structure, the new locations deviate from the old locations ($m \neq m'$).

Synthetic Test 1: Relocation with the correct velocity model

To validate that the method works, a velocity model equal to the crustal structure was chosen. The expected result was that the new locations would be the same as the old locations ($m = m'$). Forward synthetic modeling was first performed with the observed locations (m) and the known crustal structure (A), shown in Figure 4.2a. These parameters were then used to calculate the travel times (d), as expressed by Equation 4.1. The obtained travel times (d) were further used to invert for the new locations (m') with a velocity model (A) equal to the crustal structure, shown in Figure 4.2b.

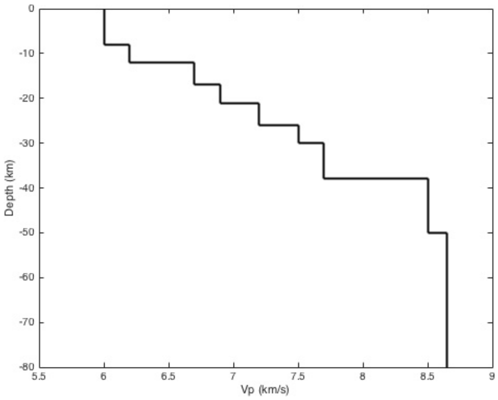

(a)

Vp [km/s]	**Depth [km]**	
6.0	0	
6.2	8	
6.7	12	
6.9	17	
7.2	21	
7.5	26	
7.7	30	
8.50	38	Moho
8.65	50	
8.9	80	

(b)

Figure 4.2: Crustal structure and velocity model used in Synthetic Test 1. a) shows the synthetic crustal structure and b) shows the velocity model used to relocate. The velocity model is equal to the crustal structure.

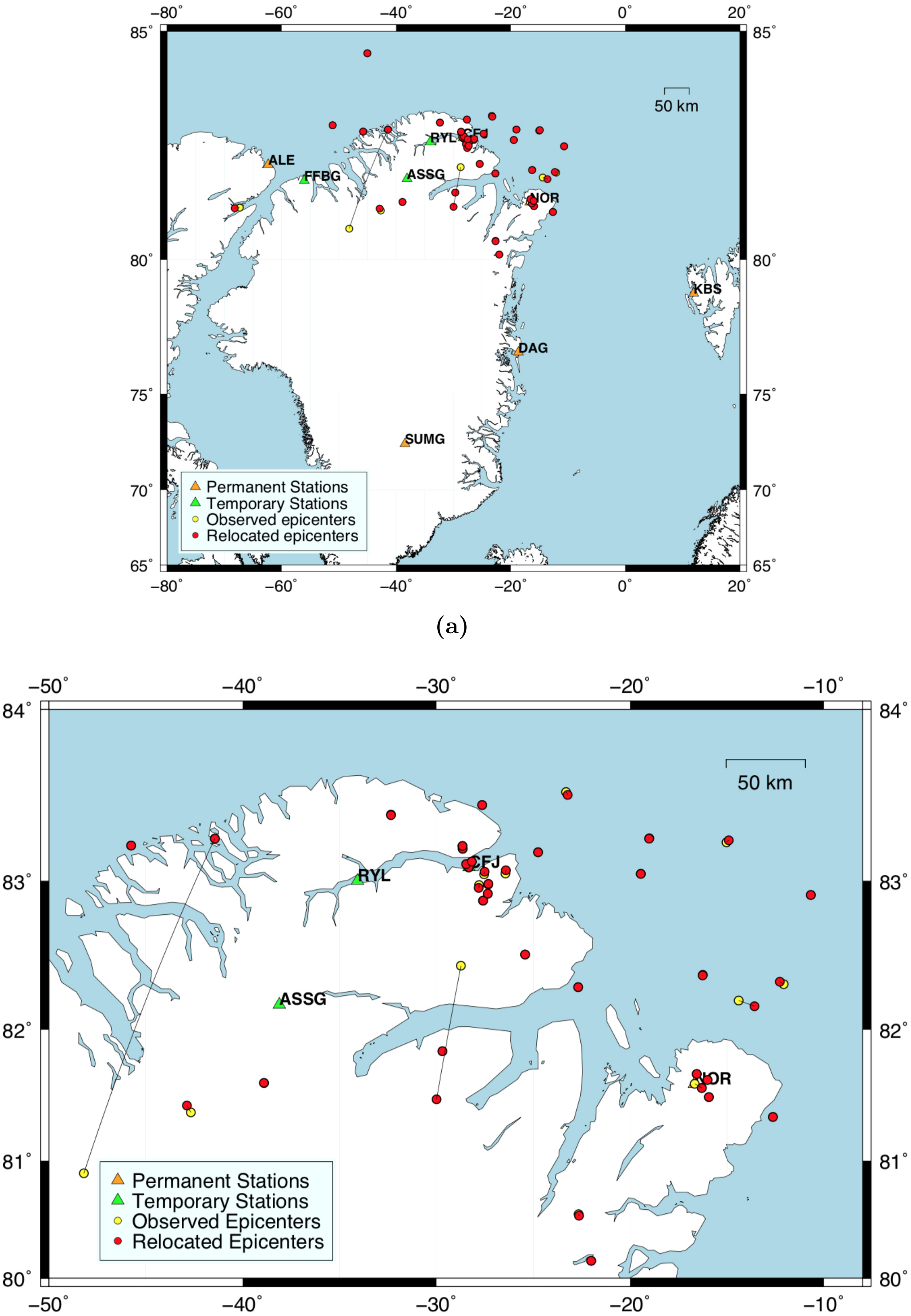

(a)

(b)

Figure 4.3: Synthetic test where earthquakes are relocated with a velocity model equal to the crustal structure. Relocated locations are represented by red dots and the old locations are shown by yellow dots. Some changes in location due to different starting locations. (Synthetic Test 1).

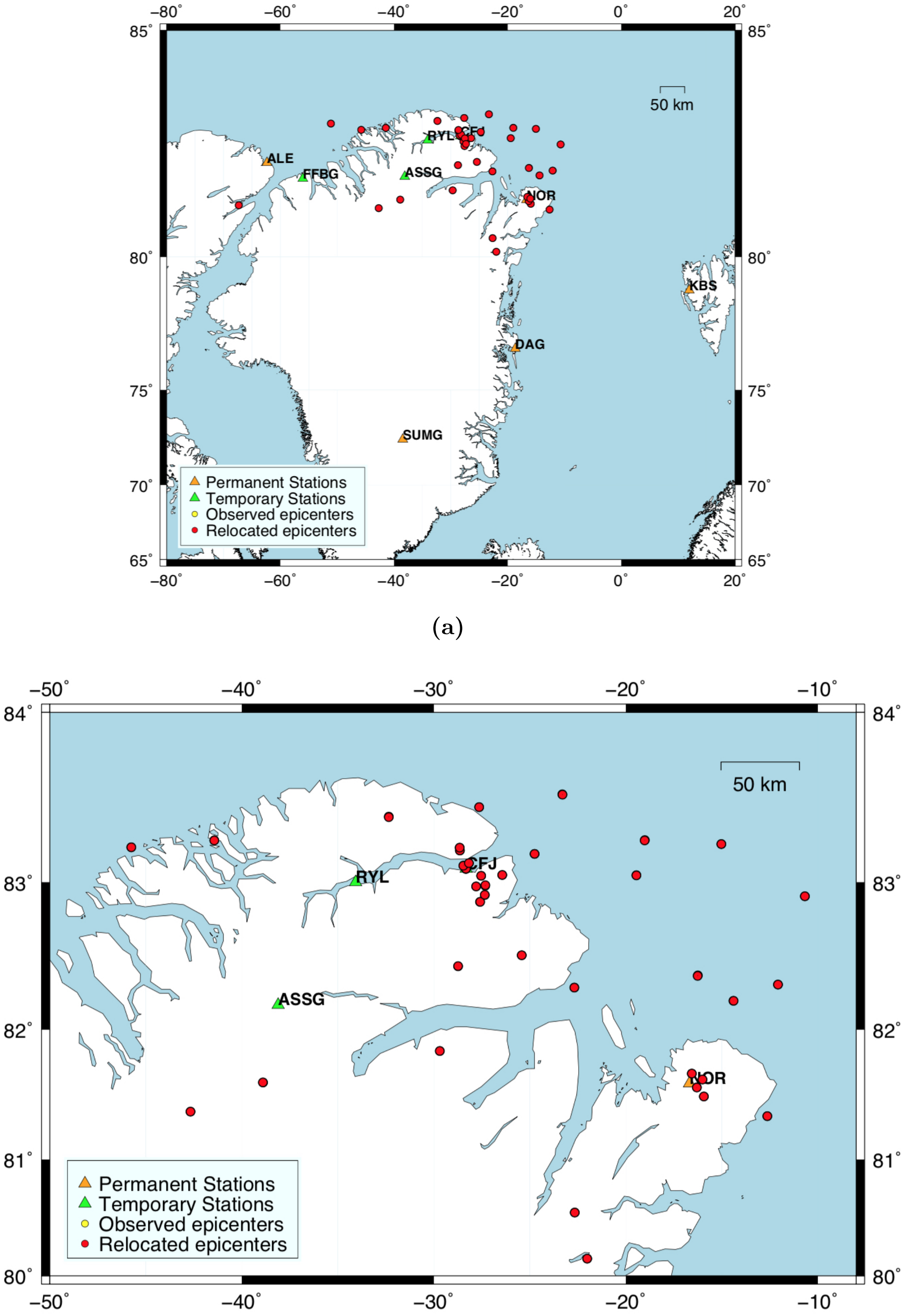

(a)

(b)

Figure 4.4: Synthetic test where earthquakes are relocated with a velocity model equal to the crustal structure and the starting locations are forced to be the same. (Synthetic Test 1).

New locations were obtained and the comparison with the old locations are shown in Figure 4.3. The old locations are represented with yellow circles and the new locations are represented with red circles. Some of the yellow circles are not visible under the red circles because the locations are so similar. A few of the estimated locations do change. This was not expected, but it happens because the starting locations has changed in the inversion process. Due to the least-square solution method, where the hypocenter solution is the absolute minimum of the error, the program has found a different local minima. This leads to a different epicenter location and then also a different starting location, giving location estimates far from each other.

By forcing the inversion to use the old starting locations, this problem is avoided. This is illustrated in Figure 4.4, where none of the yellow circles can be seen under the red circles, because the locations are practically the same. Further, will we try to see what happens when the velocity model used in the relocation process is different than the crustal structure.

Synthetic Test 2: Relocation with the wrong velocity model

In the previous subsection, the robustness of the method was tested. Now the method will be applied to show how much the earthquake locations can change when a velocity model that is different from the crustal structure is used.

The same starting locations (m) and crustal structure as in the previous test were used in this test. The first step in the method, the forward modeling, gave the same travel times (d) as in the Synthetic Test 1. For the inversion, a velocity model different than the crustal structure was applied. The simplified one layer velocity model for Greenland was used. The crustal structure and the velocity model are shown in Figure 4.5a and 4.5b, respectively. The crustal structure has seven layers above Moho and the velocity model has one layer above Moho. It is clear that the velocity model is too simple for the crustal structure.

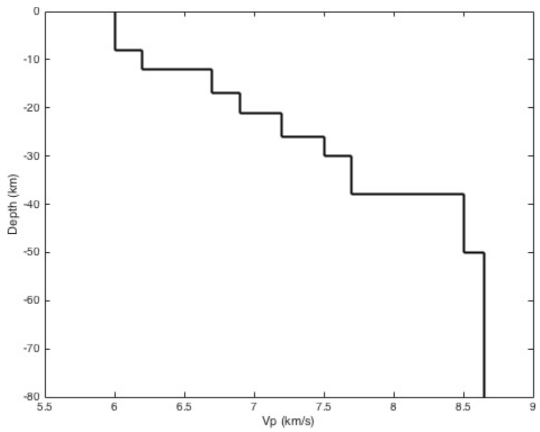

(a)

Vp [km/s]	**Depth [km]**	
6.2	0	
8.2	36	Moho
8.5	80	

(b)

Figure 4.5: Crustal structure and velocity model used in Synthetic Test 2. a) shows the synthetic crustal structure and b) the one layer velocity model for Greenland. Notice the difference between the detailed crustal structure and the simple velocity model.

The simple velocity model and the travel times were then used to invert for new locations. In Figure 4.6, the new locations (red) are compared to the old locations (yellow). The distance between the red and yellow dots is quite large. It is clear that locating earthquakes with the wrong velocity model can give epicenter locations with great error. Many of the epicenters in this test moved between 20-50 km.

The synthetic tests clearly shows how important it is to have knowledge about the crustal structure when locating earthquakes. When locating with a velocity model that is different from the crustal structure, it has been shown that the error in location can be quite large. This is applicable for areas all around the Earth and it also amplifies the need for a new regional velocity model when locating earthquakes in North Greenland.

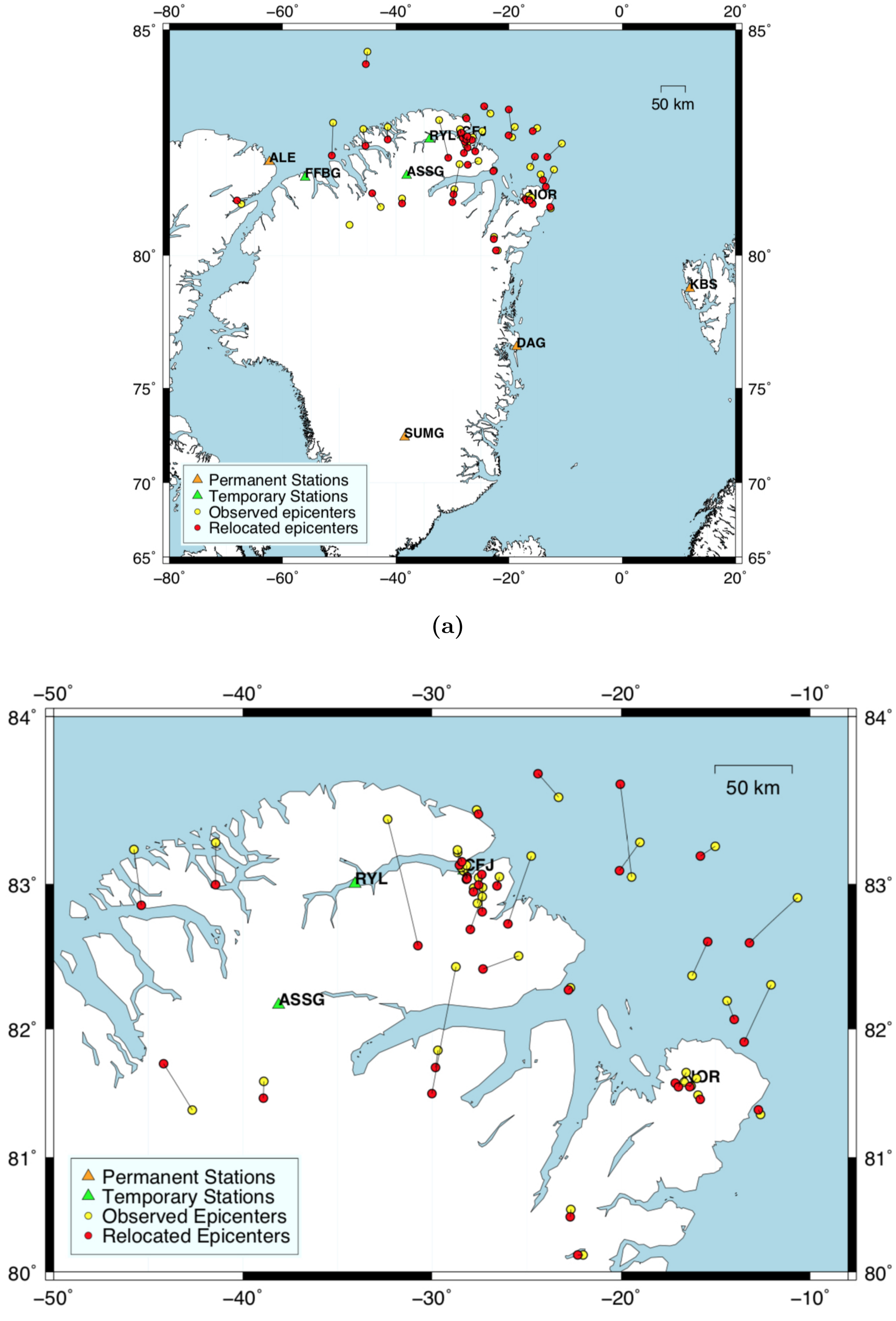

(a)

(b)

Figure 4.6: Synthetic test where earthquakes are relocated with a velocity model that is too simple for the crustal structure. Relocated locations are represented by red dots and the old locations are shown by yellow dots. (Synthetic Test 2).

4.2 From Teleseismic Earthquakes to a Detailed Crustal Structure

Previous studies of the crustal structure in Greenland are mostly based on receiver function analysis. In this thesis, a joint inversion method is applied to find the S-wave velocity structure beneath stations. The method uses both receiver functions and apparent S-wave velocities. To understand the method, receiver functions and apparent S-wave velocity will be explained separately first. The inversion combining the two parameters is then described.

4.2.1 Receiver Functions

Receiver functions (RFs) are computed from teleseismic waves that are converted at an interface and recorded by a seismic receiver at the surface. When a wave encounters a seismic boundary, the material differences between the two layers above and below the boundary causes the wave to reflect, refract and/or convert. If the wave is converted, it means that the polarization of the wave changes at the interface. Most receiver functions are made out of P-to-S (Ps) converted waves, because the phases in the P-coda are usually not contaminated by other phases, and the Ps-converted waves are the first converted waves to arrive (Rondenay, 2009).

The Ps-wave registered at the surface will have a different travel time than the direct P-wave. The delay time between the two waves can be computed and used to estimate the crustal thickness (Zhu and Kanamori, 2000). For receiver function computation, it is necessary to separate the converted waves from the other waves. This is done by rotating the coordinate system (Burdick and Langston, 1977; Rondenay, 2009).

Isolation of the wavefields

Today most seismic stations are three component systems, where the seismometers consist of a North-South, East-West and a vertical component, recognized as a N-E-Z system. The energy from both P- and S-waves will then be partly recorded on all components, due to the way the waves propagate through the Earth. It is desirable to isolate the wave energy on the different components. This can be done by rotating the coordinate system from a N-E-Z system to a Z-R-T system. This is a system that contains a vertical, radial and a transverse component. This rotation is done with equation 4.3 from Rondenay (2009).

$$\begin{pmatrix} R \\ T \\ Z \end{pmatrix} = \begin{pmatrix} -cos\gamma & -sin\gamma & 0 \\ sin\gamma & -cos\gamma & 0 \\ 0 & 0 & 1 \end{pmatrix} \begin{pmatrix} N \\ E \\ Z \end{pmatrix}, \tag{4.3}$$

where R, T and Z represent the radial, transverse and vertical components respectively. γ is the back azimuth of the incident ray, the angle at which the waves arrive at the station, measured from north.

With this rotation, the incoming converted wavefield is in direction of the radial component. This means that the Ps-waves are captured mostly on the radial component (R), which is horizontal. The direct P-waves are confined to the vertical component (Z). This is simplified and the waves are not completely isolated on one component unless the angle of incidence for the teleseismic P-wave is vertical, something that is rare. The angle of incidence for teleseismic waves are normally between 10° and 30°. Since the signals will not be completely isolated, there is some leakage of the wave energy. Even though this is the case, the waves are better isolated to one component in the Z-R-T rotated coordinate system compared to before the rotation (Rondenay, 2009).

It is possible to further rotate the coordinate system to orient the axes parallel to the incoming waves, to avoid further leakage of the energy. This is done by rotating the coordinate system to a L-Q-T system or further to a P-SV-SH system. These rotations require assumptions about the P-wave velocity. In the joint inversion method, we do not want to completely isolate the polarizations because we exploit the signal leakage to obtain the apparent incidence angles needed to calculate the apparent velocities (this will be explained later). Therefore, the Z-R-T rotation is used in this study.

Deconvolution

The signals recorded at the stations are convolutions of the source signature, the Earth's impulse response and the instrumental response from the seismic recorder. It is therefore necessary to deconvolve the seismic signal recorded at the stations. A common approach is to deconvolve the signals in the frequency domain, which is also done here.

Individual receiver functions can be stacked to increase the signal-to-noise ratio (SNR). A moveout correction should be performed to each individual trace before this operation is performed. The moveout correction accounts for the variation in distance between the source and the receiver, so that the peaks representing the same layers will appear at the same time. The stacking follows the moveout correction. It is also necessary to convert the receiver functions from the frequency domain to the time domain before analyzing the RFs. In the moveout correction process, inverse Fourier Transform is applied to convert the signal from the frequency to the time domain (Rondenay, 2009).

Analysis

The stacked receiver functions can be analyzed to obtain information about the subsurface. The radial receiver function is of interest, where the converted Ps wavefield energy is isolated. A difference in seismic properties from one layer to another will be represented as a peak in the receiver function, where the size of the peak refers to the magnitude of the discontinuity (Rondenay, 2009). The Ps-phase from the Moho discontinuity should be the second largest peak in the receiver function after the peak from the direct P-phase at time zero. This is because the variations in material properties between the lower crust and the upper mantle are large. The delay time between the P- and Ps-phase arrivals can easily be converted to depth, with Equation 4.4 from Zhu and Kanamori (2000):

$$H = \frac{t_{Ps}}{\sqrt{\frac{1}{V_{S^2}} - p^2} - \sqrt{\frac{1}{V_{P^2}} - p^2}} \tag{4.4}$$

This makes receiver functions practical tools for estimating crustal thickness beneath stations. Receiver functions contain more peaks in addition to the Moho peak, and they represent discontinuities in the crust with smaller impedance contrast. An advantage with receiver functions is that they are sensitive to deeper velocity contrasts. A known problem with receiver function inversion is the fact that the inversion is performed with prior constraints on the S-wave velocities in the starting model. This is not the case for the apparent S-wave velocity inversion, where there are no initial constraints on S-wave velocities in the crust (Svenningsen and Jacobsen, 2007).

4.2.2 Apparent S-wave Velocity

Svenningsen and Jacobsen (2007) showed that the absolute S-velocity beneath a station can be found from the receiver functions, without prior knowledge or constrains of the S-wave velocity in the crust. This entire subsection is based on their article.

To obtain the S-wave velocity structures beneath stations, information about the apparent S-wave velocity from the surface to the uppermost mantle has to be known. The next step is then to apply a standard linearized iterative inversion to obtain the S-velocities as a function of depth.

The method of calculating the apparent velocities is done by applying a low-pass filter over the receiver functions in the time domain. This is done to emphasize the spectral content of the signal in the vicinity of a given period T. Only the signal within the period is used in the calculations of the apparent velocities. The period has a corresponding wavelength which is equivalent to a certain depth in the crust and the average of the velocities down to that depth is calculated. By increasing the period, the velocities further down in the crust and upper mantle are calculated.

For higher periods, there are more peaks in the receiver function that are included in the calculations. This is because a higher period equals a larger wavelength and thus an increased depth. With increasing depth, more boundaries are encountered and also more velocities are included. This makes the calculations more complicated. Also, multiples are included for higher periods and these are biasing the results. For these reasons, the most reliable apparent velocities are obtained for the smallest periods, and thus the shallowest crust.

In the article by Svenningsen and Jacobsen (2007), it is explained that it is desirable to use the vertical and radial receiver functions to estimate the apparent velocity. To calculate the apparent velocity, the apparent incidence angle is needed. It is defined as the angle between the particle motion that appears when a P-wave hits an interface and the normal to the interface (Svenningsen and Jacobsen, 2007; Nuttli and Whitmore, 1961). This is illustrated in Figure 4.7.

The particle motion is a combination of two components, Z and R. Because the P-wavefield energy is not completely confined to either component, the leakage of energy is exploited to calculate the apparent incidence angle, $\overline{i_p}$. In the Z-R-T rotated coordinate system, deconvolving the Z-component from the R-component leads to the radial receiver function, R_{RF}. Also deconvolving Z from itself, the vertical receiver function, Z_{RF}, is obtained. Both receiver functions have a peak representing the incident P-wave, an approximated zero-phase spike, at arrival time t=0. This can be used to find the apparent incidence angle:

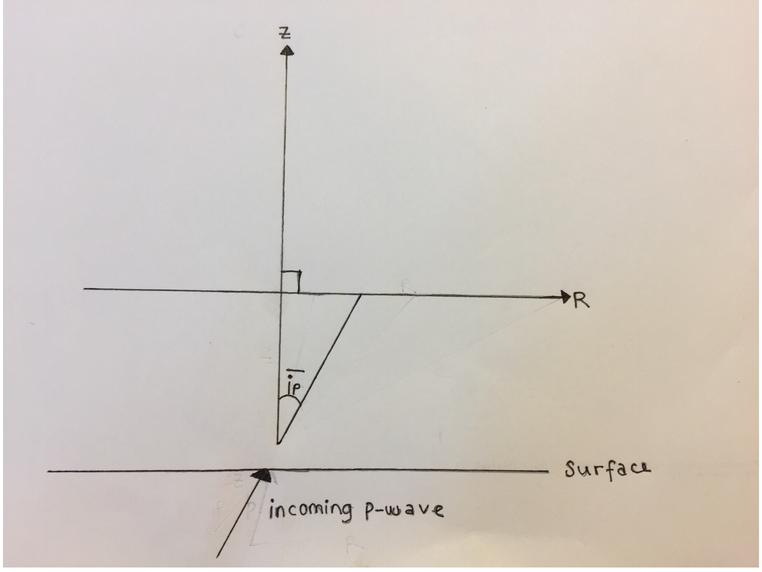

Figure 4.7: A simple illustration of the apparent incidence angle, $\overline{i_p}$.

$$\overline{i_p} = tan^{-1}\left[\frac{R_{RF}(t=0)}{Z_{RF}(t=0)}\right]. \tag{4.5}$$

Equation 4.5 shows how to calculate the apparent velocity without the low-pass filter. When a filter is applied on the receiver functions, the equation is transformed to

$$\overline{i_p}(T) = tan^{-1}\left[\frac{\int_{-T}^{T} R_{RF}(\tau)cos^2(\frac{\pi\tau}{2T})d\tau}{\int_{-T}^{T} Z_{RF}(\tau)cos^2(\frac{\pi\tau}{2T})d\tau}\right], \tag{4.6}$$

where the filter is made with a squared-cosine shape. The apparent incidence angle calculated according to Equation 4.6 is further used to calculate the apparent velocity with Equation 4.7,

$$V_{s,app}(T) = \frac{sin(\frac{1}{2}\overline{i_p}(T))}{p}. \tag{4.7}$$

The horizontal slowness of the incoming P-wave (p) is also needed and it is often set to a constant value. By ranging T from 0.1 s to $>$ 100 s and calculating the $V_{S,app}(T)$ response, we obtain the apparent S-velocity as a function of period for the entire crust and uppermost mantle. The $V_{S,app}(T)$ is inverted to represent the S-wave velocity as a function of depth.

Some problems in this process is the influence the Vp/Vs-ratio has on the inversion from $V_{S,app}$ to $V_s(z)$. The ratio is a value that has to be chosen, so assumptions have to be made. This number will probably affect the depth estimation more than the S-wave velocities.

Both receiver function inversion and apparent S-wave velocity inversion will individually result in a detailed image of the structure of the subsurface, but receiver functions are needed to perform the inversion of the apparent velocities since the apparent velocities are obtained from the RFs. By doing the inversions individually, the structure obtained only tries to fit one of the data sets. By combining the two, the structure tries to fit both data sets. This makes it a more complicated inversion and it should give better results, as the constraints of the two models complement each other.

4.3 Joint Inversion of Receiver Functions and Apparent S-wave Velocities

The joint inversion used in this thesis is performed through a MATLAB code that was originally made by Christian Schiffer and further automated and tested on both synthetic and real data by Anne Drottning (Drottning, 2017). Some changes have been made to the program after her thesis was submitted, so there are some differences in the explanation of the method in this thesis, compared to hers.

4.3.1 Joint Inversion

Solving inverse problems is complicated as often one deals with non-unique solutions. The goal of the joint inversion is to obtain a robust, unbiased shear wave velocity model below a seismic station by inverting the model parameters (p) from the combination of observed data (d) (Ammon et al., 1990; Drottning, 2017). The joint inversion method used in this thesis is calculated with equation 4.8 from Drottning (2017), which is a weighted linearized least-square iterative algorithm.

$$p_{i+1} = p_i + M[G^T C_d^{-1} \Delta d + C_p^{-1} \Delta p] \tag{4.8}$$

The model parameters (p) are represented as a matrix, with delay times between P- and Ps-waves in one column and S-wave velocities in another, $[dtps, V_s]$. Receiver function inversion alone usually inverts for V_S and depth to interfaces. Here, the method of Svenningsen and Jacobsen (2007) is used, which parameterizes the model with delay times instead of interface depth, because it reduces the non-uniqueness of the problem.

In Equation 4.8, the observed data is denoted as d, where both the receiver functions and the apparent S-wave velocities are on a matrix form, $[RF, V_{S,app}]$. C represents the covariance matrices for both the observed data (C_d) and the model parameters (C_p), representing the standard deviations of the data values (the amount of variation in the data set). M represents the postcovariance matrix, which is the standard deviation to the solution. The equation also contains G, the Jacobian matrix that relates the observed data and the model parameters. It is a representation of how much the data will be changed due to the different parameter for each iteration.

These individual parameters are combined in the last part of Equation 4.8. The combination of parameters is changing, and hopefully improving, the velocity structure for each iteration. When changes are made to the parameters, the structure is updated. For each iteration, the fit to the observed data should be better as the method tries to minimize the data error to find the best fitting solution. This error is defined as the difference between the observed and estimated data and the process is repeated until the data error converges (changes less than 1% for three consecutive iterations), with a maximum of 30 iterations. This limit is due to the time it takes to run the inversion and the expectations of the result to be good enough after 30 iterations (Drottning, 2017).

In the joint inversion of receiver functions and apparent velocities, it is possible to change the weights on the two data types. The weights range from 1 to 20, where 1 means that the results try to fit the data more than the starting model. Increasing the weights will cause the results to depend more on the starting model than the data. The standard weighting of the inversion is 1 for both data types. That means they are influencing the inversion equally and the results depend more on the data than the starting model. Increasing the weight for one of the data types means that the inversion is favoring the other data set.

It is more time consuming to run the inversion for both RF and $V_{s,app}$, compared to running an inversion for only receiver functions or only apparent S-wave velocities. This is because the joint inversion process tries to fit a more complicated and detailed dataset in the joint inversion. This should give us more robust results as the non-uniqueness is reduced.

4.3.2 Input

The input parameters in the program are files that contain observed receiver functions for each station, both the radial and vertical. The apparent S-wave velocities are also required and are computed from the receiver functions. In addition to this, we need one or more starting models to run the program. In this thesis, 35 different starting models are used. They are represented in Figure 4.8.

Some of the starting models are based on the observed data, so no prior information about the area is needed. The delay times that are converted to depth are picked from the stacked receiver function and the crustal velocities are obtained from the apparent S-velocities. The number of layers in the resulting structures are derived from the number of peaks in the observed receiver functions. These starting models are shown in the upper left corner.

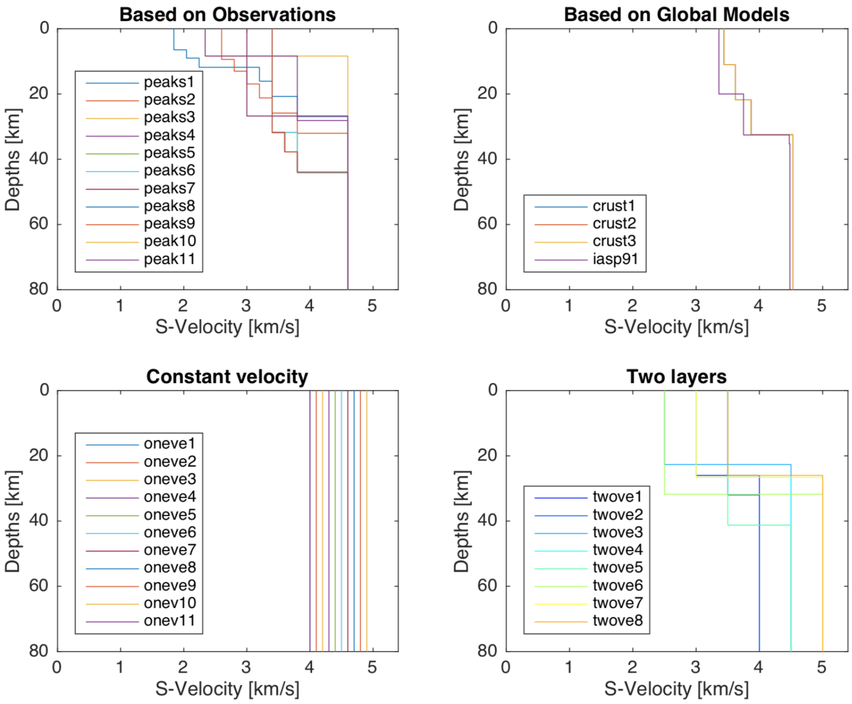

Figure 4.8: The 35 starting models used in the joint inversion method.

Some starting models are based on global models, where prior information of the area is needed. This is the iasp91 (Kennett and Engdahl, 1991) and the CRUST1.0 (Laske et al., 2013) models, shown in the upper right plot.

Some of the starting models are simpler models with fixed velocities. These are shown in the two lower plots. Eleven starting models have a constant velocity through the entire crust and mantle, with velocities between 4 km/s and 5 km/s. Nine starting models are made with two different velocities, one for the crust and one for the mantle. For the starting models with fixed velocities, the Moho is randomly chosen between a depth of 20 and 60 km.

4.3.3 Output

The program outputs an image of the structure beneath each station, where the S-wave velocity is represented as a function of depth. Multiple starting models are used and a resulting structure is calculated from each starting model. A few unrealistic resulting structures are to be expected. To avoid these structures to contaminate further calculations, a quality check is performed to remove unrealistic results. This include structure results containing unrealistically low mantle velocities or structures with mantle velocities at a shallower depth than 10 km. It also includes resulting structures with layer boundaries deeper than 80 km, structures with too low starting S-wave velocities and results where the data error is larger than the average error. The program uses 35 different starting models and calculates a resulting structure for each starting model, that gives 35 different resulting structures. The quality check is then performed to remove unrealistic results.

The program has two ways to compute and represent the structure beneath the seismic stations. An example of the outputs from the joint inversion is shown in Figure 4.9. Looking at Figure 4.9b, two resulting structures are represented with different colors. The estimated results represented in blue are obtained from one single starting model that is based on observations, *peak11*. This starting model was concluded to be the best and most reliable model by Drottning (2017).

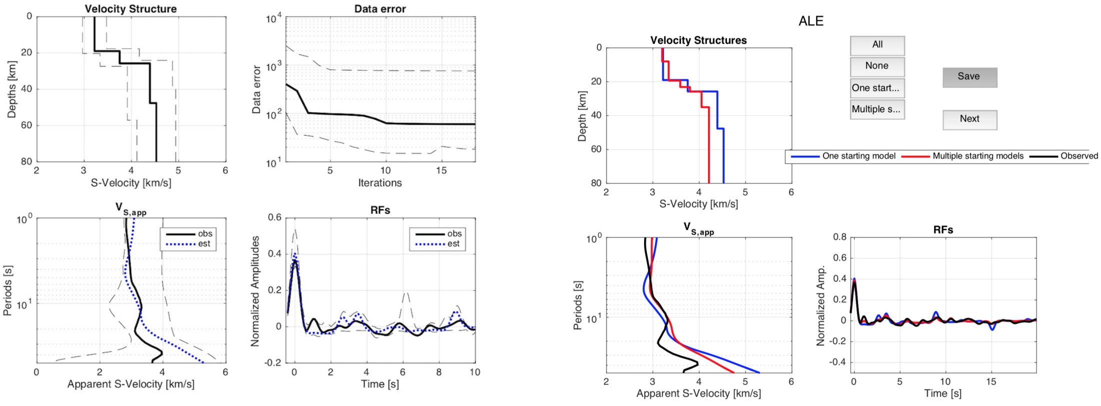

(a) **(b)**

Figure 4.9: The joint inversion results for station ALE. a) shows the structure calculated from one starting model and the errorbars for this structure. b) shows the results for one starting model and the results obtained using multiple starting models.

The estimated results represented in red are calculated from multiple starting models. 35 structures are calculated for each station and the quality control is performed to remove unrealistic structure results. Among the structures that are left after the quality control, the five most similar structure results are used to calculate an average, which result in the red structure. This method has a fixed number of layers and result in a more detailed structure than the blue structure. This might reflect a better fit to the RF and $V_{s,app}$, but can also represent boundaries that are less clear and therefore increase the uncertainty.

The two lower plots in Figure 4.9b shows how both of the estimated apparent velocities and the estimated receiver functions fit the observed apparent velocity and the observed receiver function. We want the estimated functions to fit the observed functions as much as possible, because the estimated functions combined make the main structures in the upper left plot. The boundary between the crust and the mantle normally reflects a clear peak in the receiver function, corresponding to a large jump in the S-wave velocity in the main structure. It is thus important that the peak in the observed and estimated receiver function is consistent in time.

Since the results for the single starting model (blue) in Figure 4.9b are the results mainly trusted, they are represented with errorbars in Figure 4.9a. The estimated RF and apparent velocity are here shown as blue, dotted lines in the two lower plots. The solid black lines are the observed RF and the observed apparent velocity. The resulting main structure is represented in black in the upper left plot.

Errors for the results are also calculated. For the resulting structure, error bars are calculated by using all the resulting structures obtained from the different starting models. The error bars are representing the structure with the largest deviations from the main structure that is obtained with the peak11 starting model. The error bars have the same number of layers as the main structure, something that is manipulated to give the best error estimate of the shear wave velocity variations. The error bars for the structure are represented as dotted lines, which is also the case for the error estimate in the three other subplots in 4.9a. In the upper right plot, the error is plotted with the iterations. Information about the number of iterations in the inversion can be extracted and at the same time how the error develops with the iterations. The error should converge with increased iterations.

4.3.4 Picking Moho Depths

The Moho depth is picked manually. Since the output has two resulting structures, determining the Moho depth can be challenging. In this thesis the structure determined from the single starting model is mainly trusted. The structure estimated from multiple starting models are mostly used as a comparison.

The expected S-wave velocity in the mantle is higher than 4 km/s. Looking at the resulting structures, the Moho depths are assumed to be at the corresponding depth to where the velocity increase from under 4 km/s to a velocity above 4 km/s. It is important to compare the estimated receiver functions of the resulting structures to the observed receiver functions in this process. A clear peak is expected to represent the Moho discontinuity, because of the large acoustic impedance contrast between the crustal layer above the mantle and the mantle properties below. To trust the Moho depth from the resulting structure, the Moho peak should also be visible in the estimated receiver functions at the same time as the observed receiver function peak.

The program adds some constraints to the S-velocity in the mantle to prevent the estimated model parameters to deviate too much from the starting model. Drottning (2017) constrained the S-velocities in the mantle with ±0.1 km/s. If we take a look at Figure 4.9a again, this is illustrated. In the main structure, a small boundary layer appears at a depth of 47.5 km. This layer is forced by the program to reach the expected S-velocity in the mantle. The boundary layer above, at 26 km, would here be picked as the Moho discontinuity. This appears to be the boundary with the largest velocity contrast and the depth where the transition to mantle velocities is reached.

4.4 Application to North Greenland Data

To be able to make a velocity model for the North Greenland region, it was necessary to obtain more information about the crustal structure in the area. This was done by performing the joint inversion method on the stations in the study area.

Because of the coordinate system rotation required to isolate the wavefields, one of the temporary stations in North Greenland was useless for receiver function analysis. The horizontal component BHN on station RYL was broken during the time period it was operating, so this station was not included in the inversion. The inversion was therefore performed for five stations: ALE, FFBG, CFJ, ASSG and NOR.

Three of these were temporary stations and two are permanent stations, so the quality of the data recorded are therefore varying. The receiver functions needed to run the program were downloaded and processed through the GLImER database (Rondenay et al., 2017). For all of the stations, earthquakes recorded with an epicentral distance between the 29° and 98° distance range were included. For the permanent stations, a magnitude of mb ≥ 5.8 was required for the event to be included. For the temporary stations, the limit was lowered to mb ≥ 5.5. This is a standard procedure by GLImER and is done to allow more earthquakes (more data) to be included in the calculations.

5. Results

The results in this chapter are divided in two parts, the structure results and relocation results. For each station, two estimated S-velocity structures as a function of depth were imaged. The imaging results from the five stations will be represented first. The structure results are further implemented into a series of average velocity models for the study area. In the end, the earthquakes found in North Greenland between 2004 and 2007 are relocated with the different velocity models.

5.1 Structure

The choice of starting model will affect the result, and the number of starting models are therefore important. The structure from multiple starting models would probably be more reliable if more starting models were included. The structures obtained for the different starting models are either local minimas or the absolute minimum in the objective function we are trying to minimize, where the absolute minimum would represent the best structure.

When multiple starting models are used, some models result in local minimas rather than the absolute minimum. This is not problematic if many starting models are used, because it is more likely that the absolute minimum is found for most solutions. When only 35 starting models are used, it is often difficult to determine if most of the results found the absolute minimum, if a lot of the solutions found the same local minima or if the solutions are scattered around at different local minimas. If five structure results that are the five most similar structures have resulted in a local minima, the result will be a structure that is incorrect, because the correct structure is represented by the absolute minimum. Because of this, the red structure is not the most reliable. However, it is useful to compare it with the structure from one starting model, the single starting model that was concluded to provide the most robust results by Drottning (2017).

The results from the stations will be presented in alphabetical order.

5.1.1 Crustal Structure Beneath the Stations

Station ALE

The results for station ALE are shown in Figure 5.1. The observed receiver function in the lower right corner and the observed apparent velocity function in the lower left corner are represented with black lines. Both have a realistic structure, so the data for this station is good. Through the GLImER procedure, 891 receiver functions were obtained for this station after the SNR quality control was performed. 127 of these events were removed in the quality control by the inversion program. This second quality control was performed to make sure the receiver functions in the stacking do not disturb the wanted signal. Station ALE is a permanent station that has been in operation since 1990. Many events are therefore recorded, so even when removing events in the quality controls, a solid number of receiver functions remain for the inversion process. 764 individual receiver functions were stacked to obtain the observed receiver function. The Moho peak in the observed RF seems to be around 3.8 s.

In Figure 5.1b the results from the two different methods are shown. The estimated receiver functions have distinct peaks at the same time as the observed RF, see the lower right plot. The estimated RF representing the structure obtained from multiple starting models (red) seems to fit the observed RF better than the estimated RF representing the structure from the single starting model (blue). The red structure has a fixed number of layers higher than the number of layers in the blue structure. It is therefore easier for this function to fit the observed function. Even though it might fit the Moho peak better, it appears to be too flat for some of the other peaks in

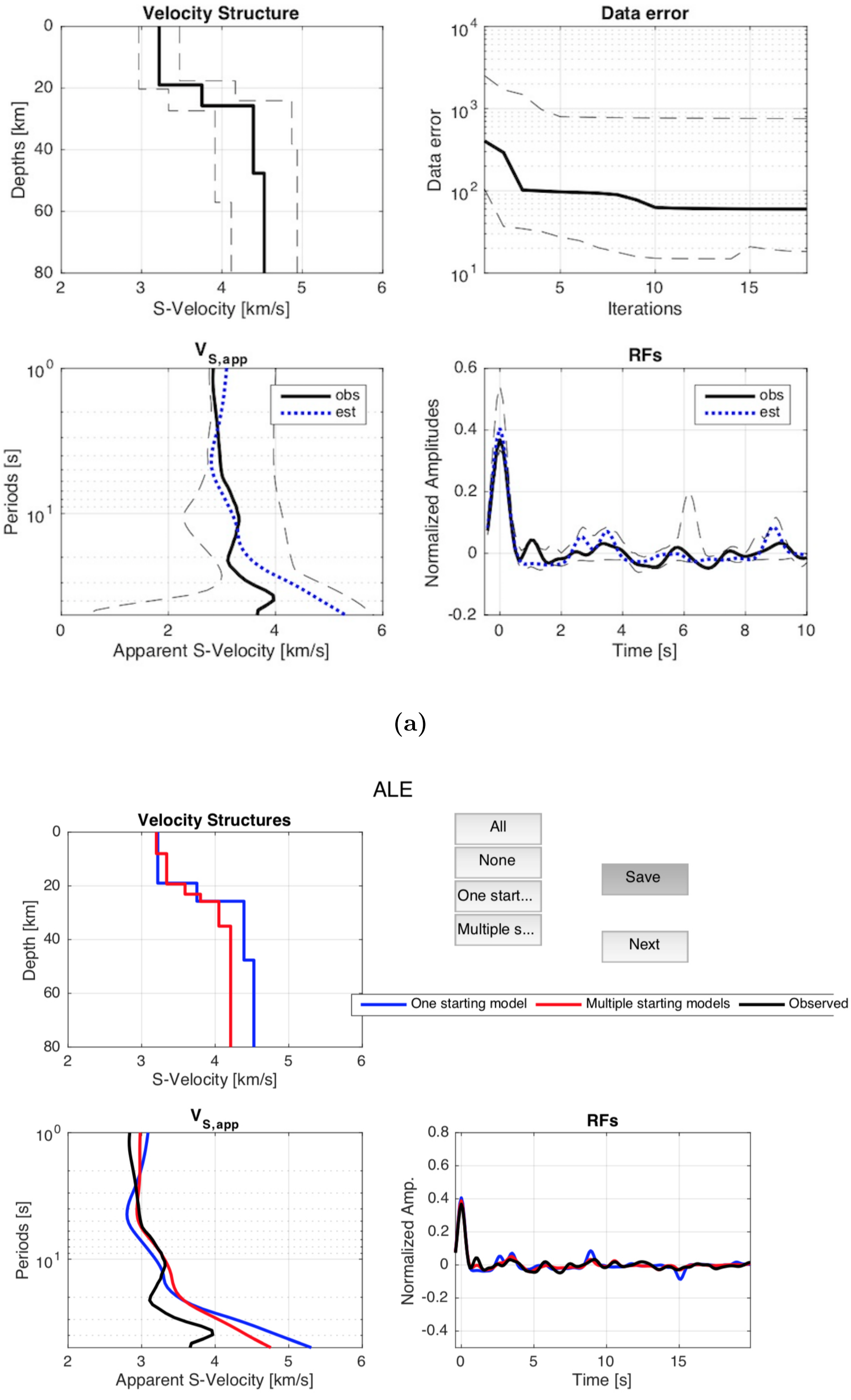

(a)

(b)

Figure 5.1: Joint inversion results for station ALE.

the observed RF. In the apparent S-wave velocity plot to the left of the RFs, the observed apparent velocity function starts at low velocities just below 3 km/s with slowly increasing velocities with period up to 10 s. The estimated apparent velocities show a good fit to the observed $V_{s,app}$ up to that period. Deeper down in the Earth, the uncertainties increase and it is more difficult to obtain a good fit between the observed and estimated apparent velocities.

The resulting structure using multiple starting models (red), represents a structure with more layers than the structure obtained with one single starting model (blue). The boundaries are then less distinct and make it more difficult to interpret where the big velocity contrasts are. For the crust, the difference between the two structures are the number of layers obtained. The velocities correspond well with each other. The largest difference between the two structures is the velocities in the mantle. The transition to Mantle velocities corresponds to a depth of 26 km. This boundary is present in both structures, but is less distinct in the red structure compared to the blue structure. This depth is in agreement with the peak in the receiver function.

In Figure 5.1a the results for the single starting model are represented with error bars. The error bars are helpful to look at to see how big of a deviation there is when using different starting models. The main structure with error bars shows an uncertainty in the velocity of around ± 0.2 km/s for the upper crust. The uncertainties increase when entering the mantle, where the uncertainty is around ± 0.4 km/s. The inversion ran 17 iterations for the single starting model and the data error converged around iteration 10.

Station ASSG

The inversion results for station ASSG are shown in Figure 5.2. For this station, the observed RF looks very good with a clear Moho peak at T$\approx$ 4.9 s. The observed apparent velocity curve is complex and not realistic for the higher periods. Since the observed apparent velocities are calculated from the receiver function, this unrealistic velocity curve probably arises because the observed receiver function contains multiples and/or because the data quality

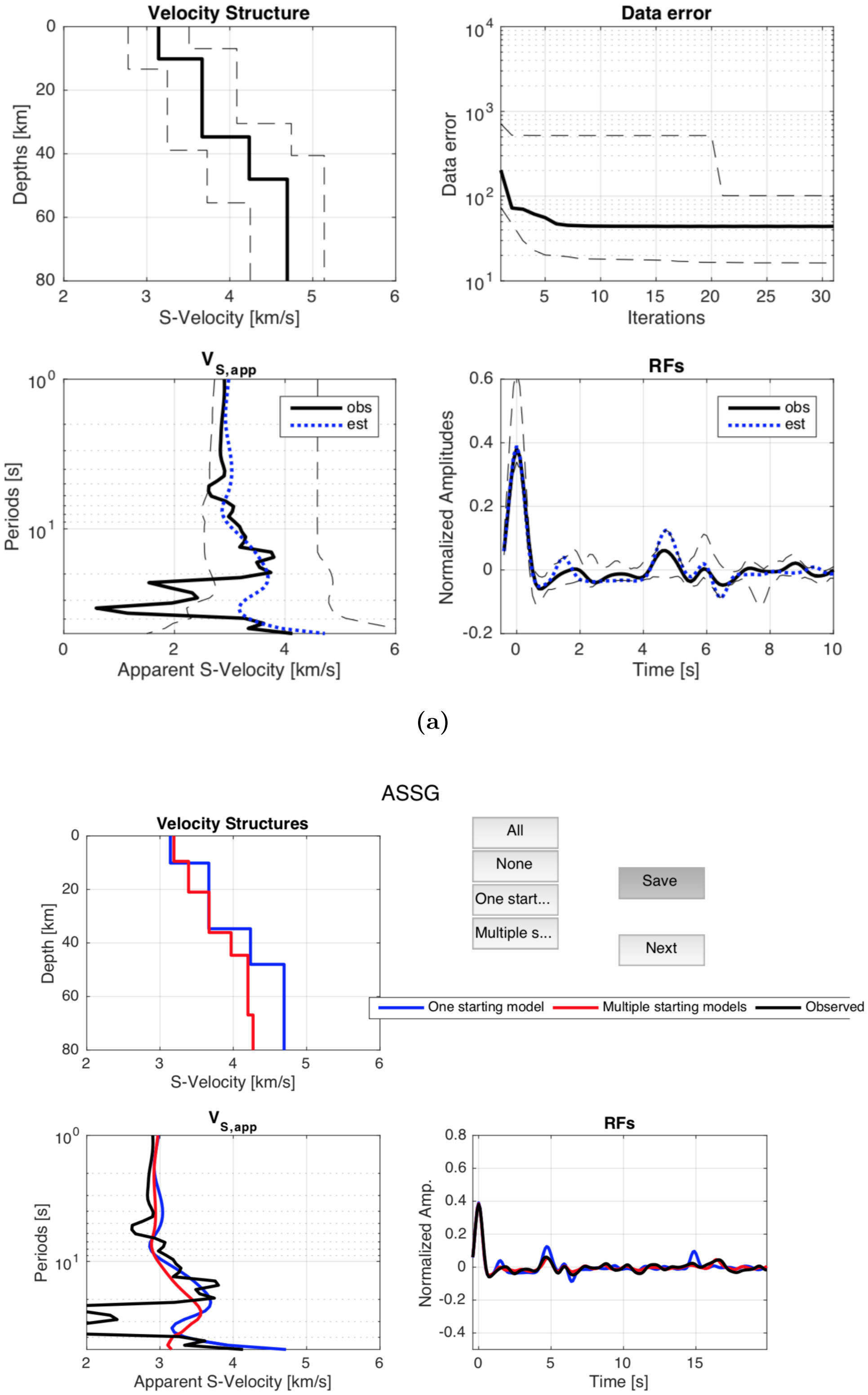

(a)

(b)

Figure 5.2: Joint inversion results for station ASSG.

for this station is poor. Through the GLImER procedure were 47 individual receiver functions obtained. In the quality check, only eight receiver functions were removed. This could mean that there was little noise contaminating the signals recoded at the station, even though this station was temporary.

Figure 5.2b shows the results from the two different methods for station ASSG. Both of the estimated RFs fit well with the observed RF, including the Moho peak. The estimated apparent velocities also fit relatively well to the observed data, considering the complicated shape of the observed apparent velocity curve. The two structures obtained for this station are also quite similar before the mantle velocities are reached. The red structure has more layers, but it looks like both structures start and end with similar crustal velocities. In the transition to mantle velocities, a difference in velocities arise between the two structures, where the structure obtained from multiple starting models show lower velocities than the structure obtained from the single starting model.

The transition to mantle velocities corresponds to a depth of 35 km. There is also a clear increase in velocity at 48 km depth, where the velocities increase even more. This increase is quite large, but since there are no clear peak in the receiver function corresponding to this boundary, it is assumed to be a result of the S-velocity constraints, forcing the structure to reach higher mantle velocities.

In Figure 5.2a, the results from the single starting model is shown with error bars. The data error started to converge around iteration 7, but the inversion still ran 30 iterations. After iteration 20, the deviation in the error decreased drastically. In the lower left plot it is seen that the observed apparent velocity reaches outside of the error bars for high periods. This means that none of the starting models were successful in fitting the complex structure. Also, the error bar deviates a lot for the higher apparent velocities. This implies that at least one starting model estimates velocities that are too high.

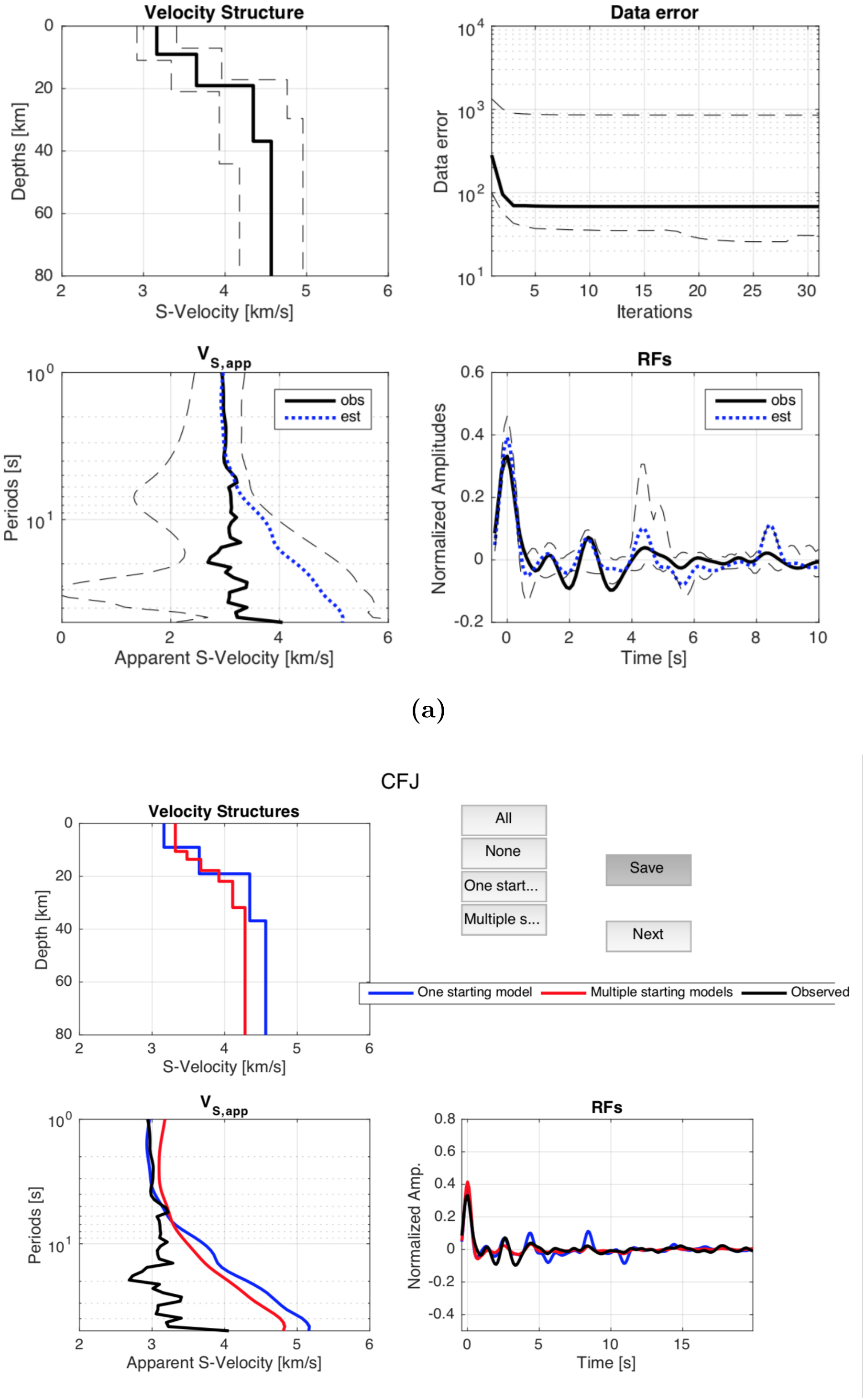

(a)

(b)

Figure 5.3: Results for station CFJ.

Station CFJ

The results for station CFJ is shown in Figure 5.3. The observed apparent velocity curve looks odd, probably because the data quality for this station is poor or because of multiples in the receiver function. This station was a temporary station in operation for four years. The number of individual receiver functions that was used to calculate the observed RF for this station was 78, as 27 receiver functions did not pass the quality check. The observed receiver function is not as good as the RF for ASSG, even though more receiver functions were included in the stacking. From the observed RF, the Moho peak appears to be around T$\approx$ 2.6 s or T$\approx$4.8 s.

Figure 5.3b shows the results for the two methods for station CFJ. The blue estimated RF seems to fit the first possible Moho peak in the observed RF better than the second peak, where the blue overshoots the peak. The blue RF also have some later peaks that are very distinct, which are not present in the observed RF. For the red estimated RF, the fit to the Moho peak is better for the second peak alternative in the observed RF. Compared to the first peak, the red peak is too flat. The estimated apparent velocity fit to the observed apparent velocity is good for the first periods, especially for the blue function. After approximately 7 s, the apparent velocity deviates more. This is a result of the complicated structure the observed apparent velocity has. It is too complex for the estimated apparent velocity to fit.

The resulting structures from the two methods beneath this station differ more than they did for the previous stations. The structure obtained from the single starting model (blue) starts with a lower velocity in the upper crust compared to the structure obtained from multiple starting models (red). Both structures shows an increase in S-velocity to above 4 km/s around the same depth, but the layer in the red structure is less distinct. It appears to be two jumps in velocity in the red structure, which could both represent the transition to the mantle. The corresponding depths of these boundaries are at 21 km and 32 km. It is difficult to determine which one that reflects the Moho. The latter boundary should probably be favored, since that velocity increase corresponds to a better fit between the estimated and observed RF. For the blue structure, the velocity increase is more distinct and the transition to mantle velocities for this structure corresponds to a depth of 19 km, consistent with the first of the two peaks in the RFs. Also for this station the difference in mantle velocities have the same trend, where the red structure shows lower velocities than the blue structure.

In Figure 5.3a, the error bars are shown for the single starting model results. The second peak in the RFs has a much higher error than the first peak. 30 iterations were performed for this station and the data error converged already at iteration 3. The deviation in the data error is quite big and the uncertainties in estimated apparent velocity seem to be small in the upper crust and very large for the mantle. This is also the case for the S-wave velocity, from the error bars the uncertainty is around ± 0.15 km/s in the upper crust and ± 0.4 for the mantle.

Station FFBG

Figure 5.4 shows the results for station FFBG. The observed data for this temporary station also contains a lot of multiples or has poor data quality. The observed receiver function does not have a clear Moho peak and the observed apparent velocity curve for higher periods has an unrealistic trend. 33 individual receiver functions passed the quality check and were used to obtain the observed RF, where 24 receiver functions were removed in the process. It appears to be difficult to obtain good quality data for this station.

In Figure 5.4b, it is shown that the estimated RFs do not fit the observed RF. For the blue RF, the peaks are present at completely different times, and for the red RF, the peaks are very weak and can almost not be seen. The estimated apparent velocity is not a good fit to the observed apparent velocity either. The red apparent velocity curve has an acceptable fit for the middle periods, but it is not enough to trust the resulting structures obtained from this. However, if we were to only look at the main structure result alone, the velocity increase to mantle velocities happens at a corresponding depth of 37 km. The results for this station are very tentative and are therefore not included in the procedure of making the regional velocity models.

Station NOR

The last station is the permanent station NOR. The results for this station are shown in Figure 5.5. The data quality for this station appears to be good, as the observed apparent velocity curve does not decrease as it has done in the other temporary stations. The observed receiver function has a relatively clear Moho peak at T$\approx$ 4.1 s. For this station, 52 individual radial receiver functions were stacked to obtain the observed RF, and then 83 RFs were removed in the quality control.

In Figure 5.5b, the results from the two methods are shown. The estimated RFs fit the observed receiver function well, but the blue slightly overshoots. The same applies for the $V_{s,app}$, where the estimated apparent velocity curves are matching the observed apparent velocity curve. The observed apparent velocity in the upper crust is low, resulting in low velocities for the S-velocity structures in the upper crust visible in both the resulting structures. The two structures match each other quite well. Also for this station, the red structure has more layers than the blue structure. The velocities in the crust are consistent for the two structures, but deviates more from each other in the mantle. The transition to mantle velocities appears to be of a corresponding depth of 31 km. This boundary is more distinct in the blue structure than in the red, but it is visible in both structures.

In Figure 5.5a the error bars are represented with the results from the single starting model. 10 iterations were needed for this inversion and the error converged at iteration 7. The error bars for the apparent velocity appears to be small.

For many of the resulting structures, it appears to be a small boundary in the mantle, represented as a small increase in the S-velocity. This layer is in most cases forced by the program, because of the constraints on the S-

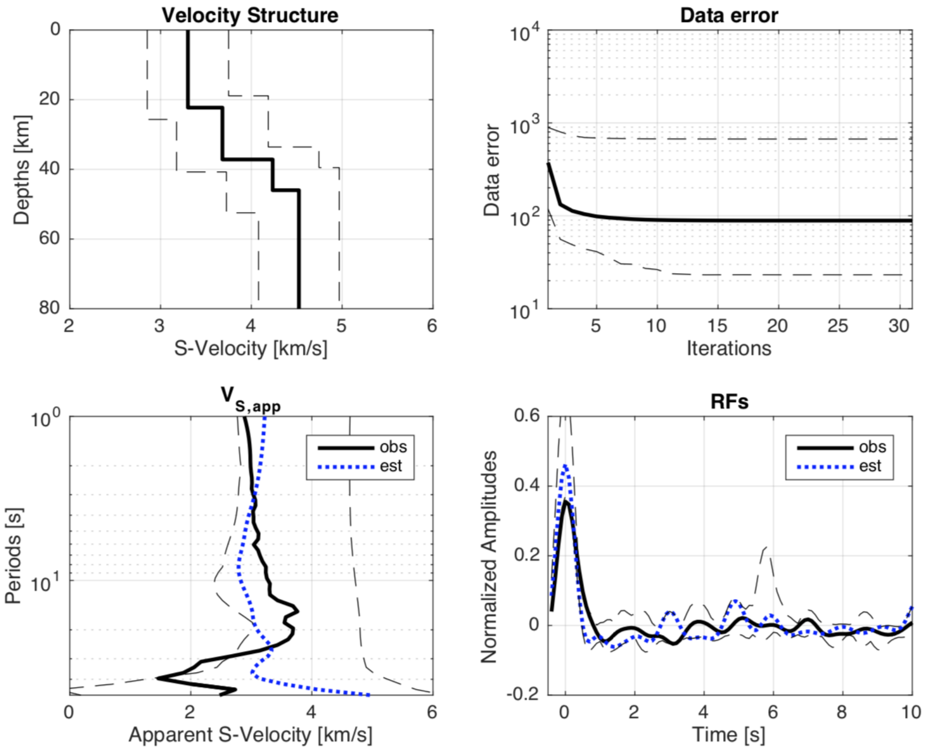

(a)

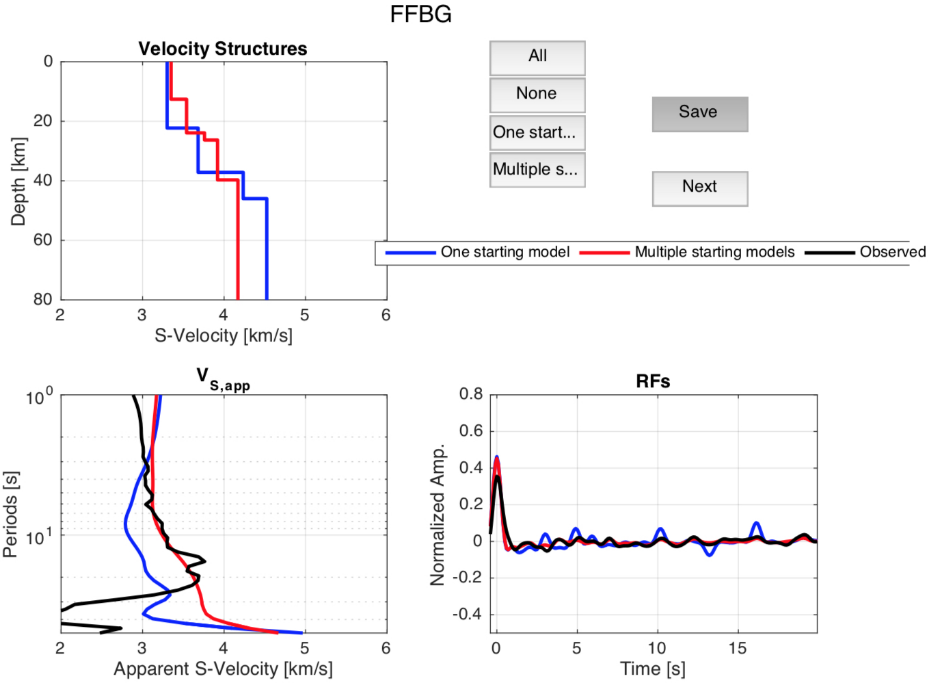

(b)

Figure 5.4: Results from the joint inversion.

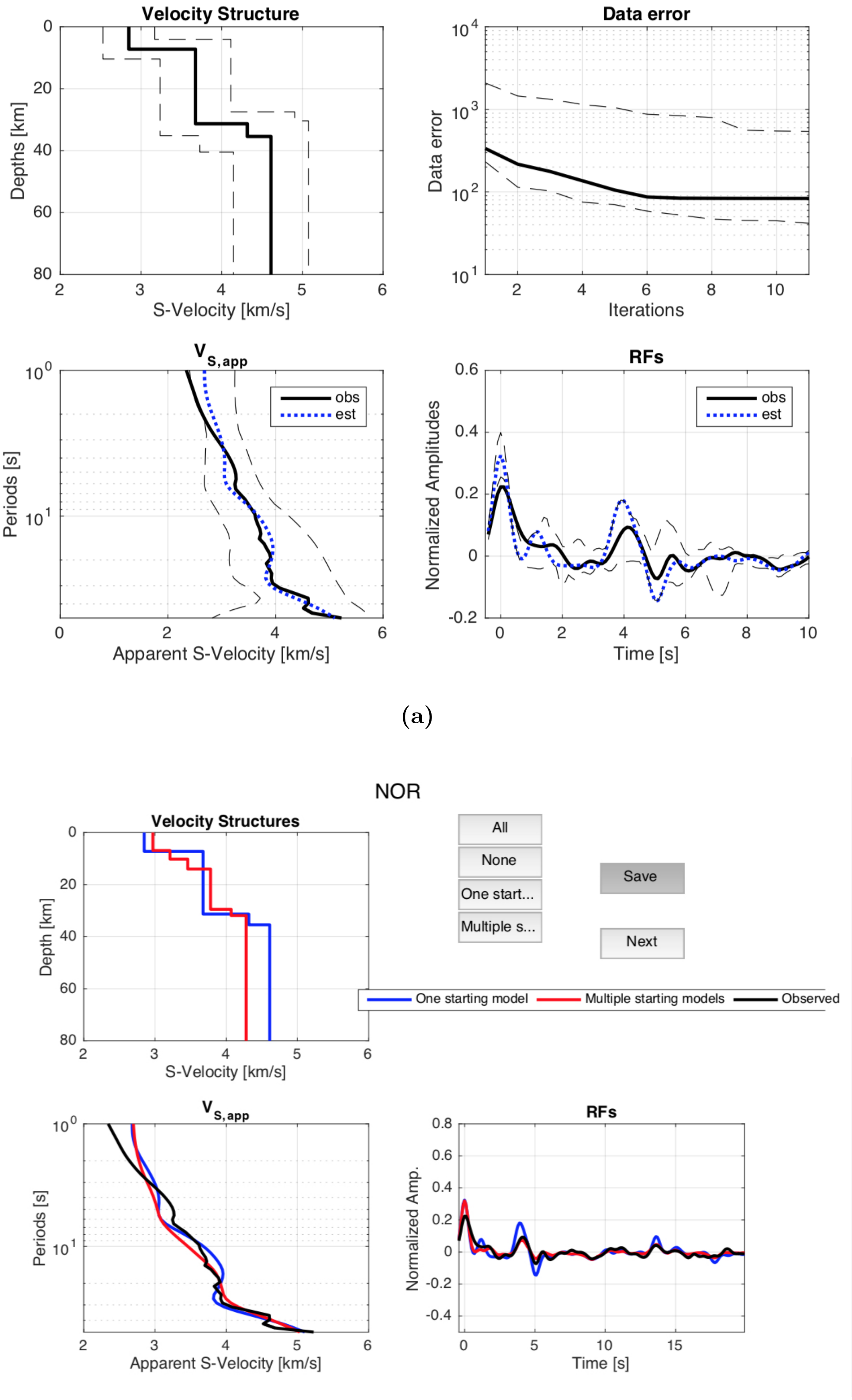

(a)

(b)

Figure 5.5: Results from the joint inversion.

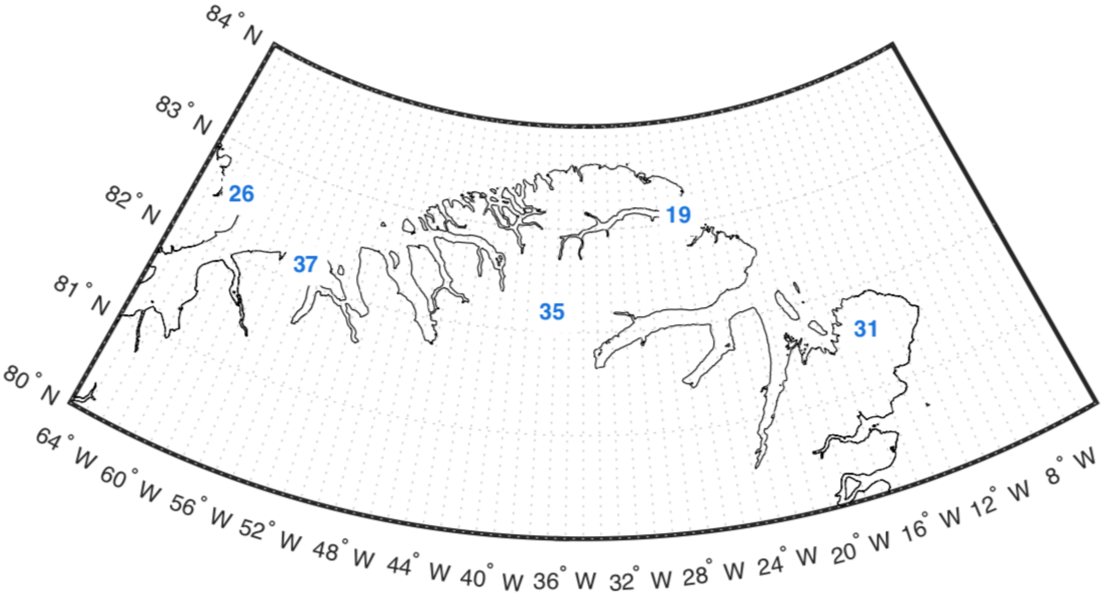

Figure 5.6: Estimated Moho depths in North Greenland beneath the seismic stations.

velocity in the mantle. The program recognizes that the velocities are too low and forces them to reach a higher value by adding a small boundary in the S-velocity structure. As long as there is no peak in the observed receiver function that could cause this layer, it should be ignored, but the velocities it represents are important.

The estimated resulting layer depths beneath each station are represented in Table 5.1. Looking at the values in the table, we find that the layer depths vary a lot. It is difficult to determine a uniform 1-D layered structure for the entire region. We can not be sure if the area is consistent with the same amount of layers and geological properties. Also, the Moho depth varies significantly across the region. The Moho depths are summarized in Figure 5.6.

	ALE	**ASSG**	**CFJ**	**FFBG**	**NOR**
1st boundary	19	10	9	22	7
2nd boundary	26	35	19	37	31
3rd boundary	47.5	48	37	46	35

Table 5.1: Layer depths beneath each seismic station, estimated from the structures obtained from the joint inversion method. All depths are in km and correspond to the bottom of the layer.

The purpose of performing the inversion was to obtain information about the crustal layers and the corresponding velocities, to be able to build a velocity model from the results. Figure 5.7 shows how the S-velocities vary with depths beneath the stations in North Greenland. The transition to mantle velocities are represented with blue colors and lower velocities are represented with red. The figure shows five bars, one for each station, colored with velocities as a function of depth. The width of the bars is determined by the distance to the next station. When the results are represented in this way, it is easy to see the general structural trends across the region. The velocities and their corresponding depths are used to make a series of regional velocity models.

5.1.2 Regional Velocity Models

Three velocity models for the region are obtained by taking the average of the resulting structures from the joint inversion. All the resulting structures are plotted together in Figure 5.8. The inversions that have been carried out in this chapter provide us with estimated S-wave velocities below the region. The calculations of epicenters require P-wave velocities in the velocity model. Therefore, we must convert our S-wave velocities into P-wave velocities. To do so, we apply a constant Vp/Vs-ratio of 1.74 for the conversion.

The velocity models are called *Velocity Model 1*, *Velocity Model 2* and *Ve-*

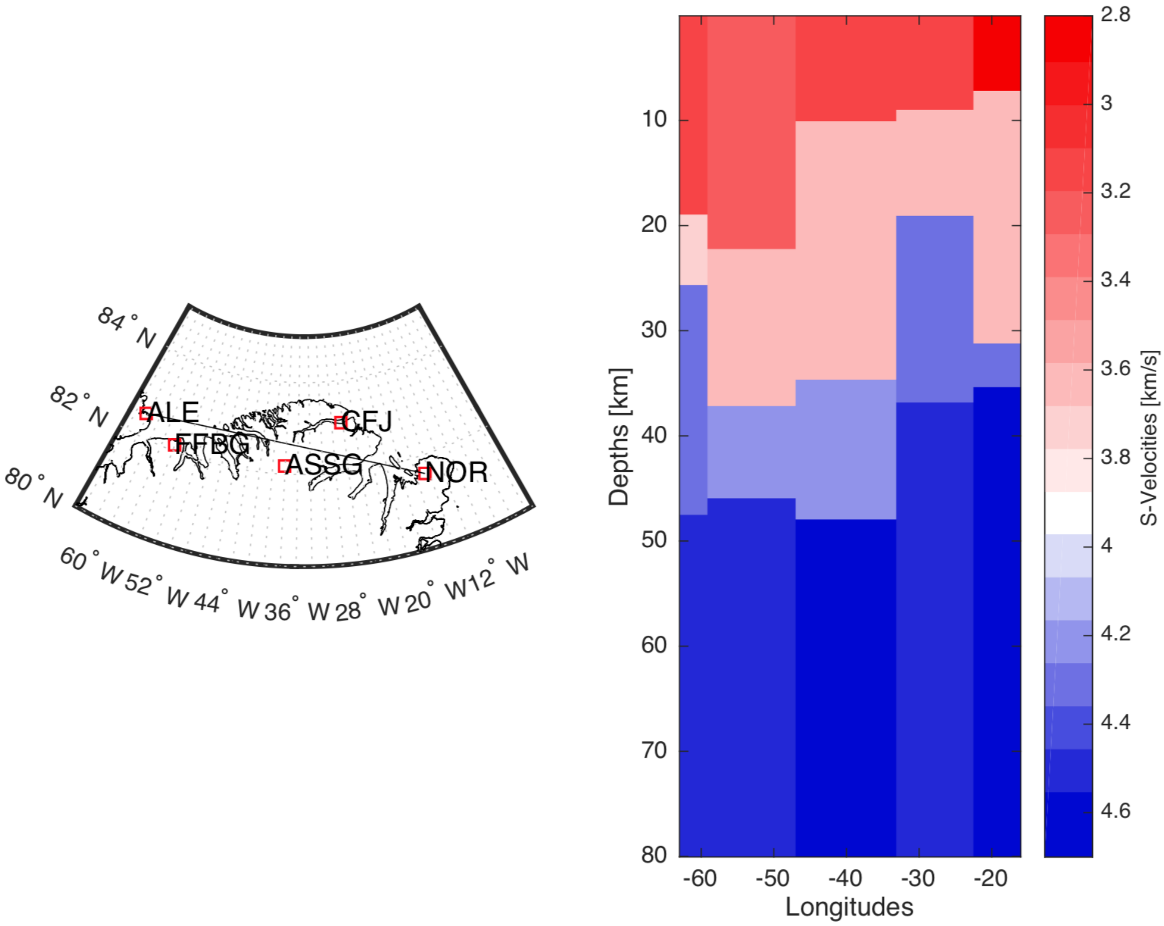

Figure 5.7: Estimated S-wave velocities shown as a profile across the stations in North Greenland. The colorscale is shown on the right side of the figure.

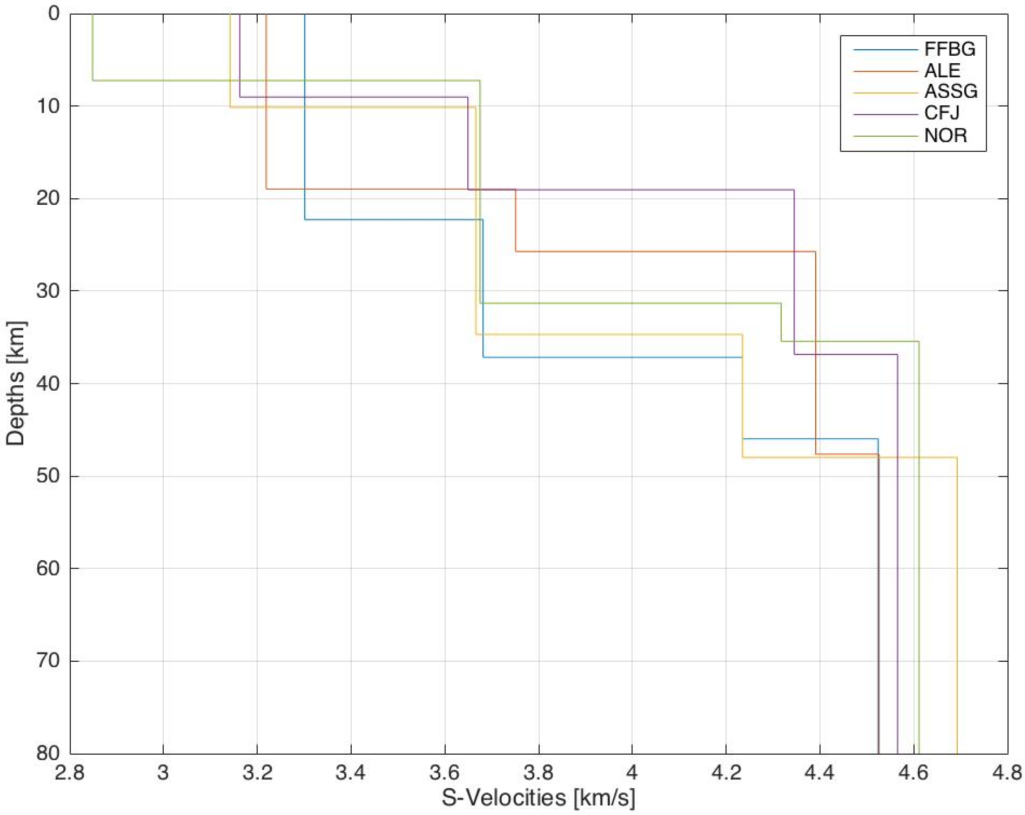

Figure 5.8: The resulting structures beneath the five seismic stations. The results are obtained through the joint inversion method with the single starting model.

Vs [km/s]	Vp [km/s]	Depth [km]	
3.0	5.2	0	
3.4	5.9	9	
3.7	6.4	19	
4.4	8.0	28	Moho
4.6	8.5	80	

Table 5.2: Velocity Model 1. Three layers above Moho. The layer depths correspond to the bottom of the layer.

locity Model 3. They will also be referred to as the first, second and third velocity model, respectively. The inversion program does not calculate velocities deeper than 80 km, therefore the velocities below 80 km are set to be 8.5 km/s in all the velocity models.

1. **Velocity Model 1** was made by visually looking at the structure results from the stations (Figure 5.8) and calculating the average layer depths. The Moho depth beneath each individual station was given more weight in this calculation than for the second velocity model. This velocity model has three layers above Moho, simply because the structure results mainly gave two or three layers above Moho in the structure. The resulting velocity model is shown in Table 5.2.

2. **Velocity Model 2** was made automatically in Matlab, through a program made by Anne Drottning. It samples the velocity values every 10 depth meter for each station, and then a new velocity for each corresponding depth is calculated. The number of layers in the velocity model is determined by the user. When making the velocity model, different number of layers was tested, since this is a choice by the user. A boundary layer at 31 km seemed to be present for any number of layers chosen. The velocity corresponding to this depth was also compatible with mantle velocities. This boundary was therefore assumed to be the Moho discontinuity. A velocity model with four layers above the Moho was chosen as the final model, because in this way, dis-

Vs [km/s]	Vp [km/s]	Depth [km]	
3.1	5.4	0	
3.4	5.9	7	
3.7	6.4	10	
4.0	6.9	19	
4.3	7.8	31	Moho
4.5	8.5	80	

Table 5.3: Velocity Model 2. Four layers above Moho. The layer depths correspond to the bottom of the layer.

tinct boundaries are obtained. The resulting velocity model is shown in Table 5.3. This velocity model does not deviate too much from the first velocity model, but the Moho depth for the first velocity model is shallower. There are also some differences in velocities between the two models, especially for the upper mantle.

3. **Velocity Model 3** was made with the same velocities and depths for the crust as the second velocity model. For the mantle, the P-velocities was fixed to 8.2 km/s for the upper mantle, even though the joint inversion result did not reach quite as high velocities. The reason for choosing this velocity for the mantle was that the upper mantle velocities in the one-layer Greenland Velocity model have these high velocities and it is of interest to use the same mantle velocities, but a more detailed crustal structure for the region and compare the RMS values for the locations.

5.1.3 Choosing One Velocity Model

The model that minimizes the misfit is considered to be the better model. When relocating with the three velocity models, the overall RMS for all events were considered. The RMS values for each individual event are shown in Figure 5.9.

Vs [km/s]	Vp [km/s]	Depth [km]	
3.1	5.4	0	
3.4	5.9	7	
3.7	6.4	10	
4.0	6.9	19	
4.3	8.2	31	Moho
4.5	8.5	80	

Table 5.4: Velocity Model 3. Four layers above Moho and fixed mantle velocities.The layer depths correspond to the bottom of the layers.

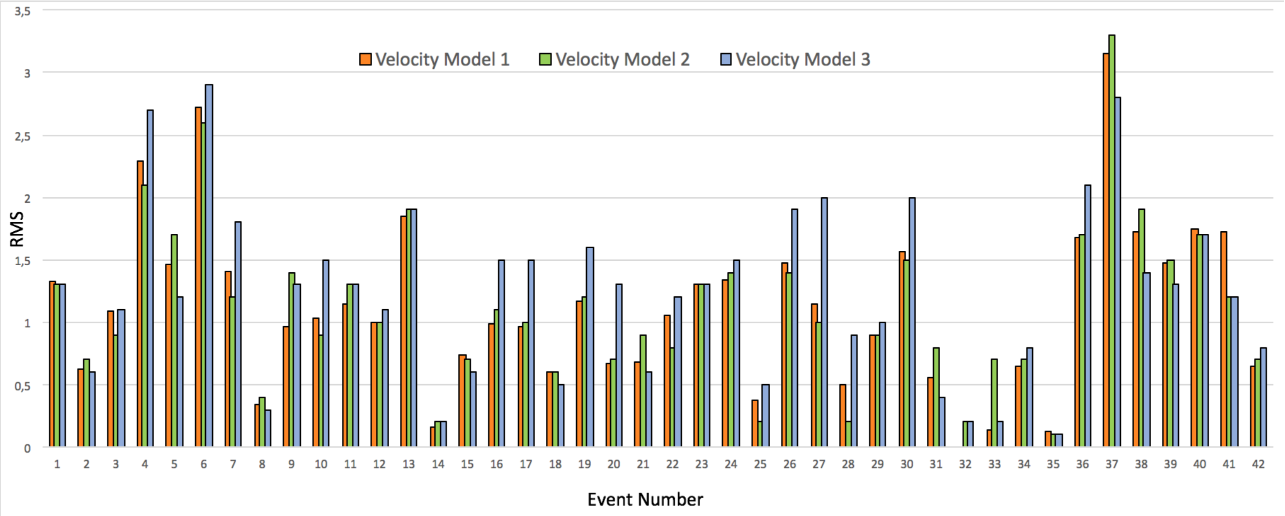

Figure 5.9: RMS for the 42 events located with the three velocity models.

It is seen that the RMS obtained with Velocity Model 3 (blue) stands out because many of the events have a higher RMS. For Velocity Model 1 and Velocity Model 2, it is not easy to see if any of the two represents locations that are more accurate. The overall RMS values are therefore used. The overall mean RMS value for the locations obtained with the three new velocity models are presented below:

Velocity Model 1: RMS = 1.279
Velocity Model 2: RMS = 1.288
Velocity Model 3: RMS = 1.417

From these numbers, Velocity Model 1 is considered to be the better model.

5.2 Relocation

The locations obtained when relocating with Velocity Model 1 will further be presented and the new epicenter locations are shown in Figure 5.10. The old epicenters located with the Greenland Velocity Model are denoted as *Original Epicenters* and plotted with small, yellow circles. The new relocated epicenters are shown with larger, orange circles. The circles representing the same events are connected with thin black lines, to easily compare where the earthquake locations move. Some of the events that are further from the seismic stations appear to have a larger difference in location estimate, compared to the earthquakes that are located close to seismic stations.

In Figure 5.11 the estimated earthquake depths are represented at their longitude location, for comparison, the depths for both velocity models are plotted. It is seen that most of the earthquakes are located between a longitude of -30° and -13°. This applies to the locations obtained with both velocity models, so it appears that the longitude and latitude do not change too much, but the depth does. The change in depth for each event is further investigated.

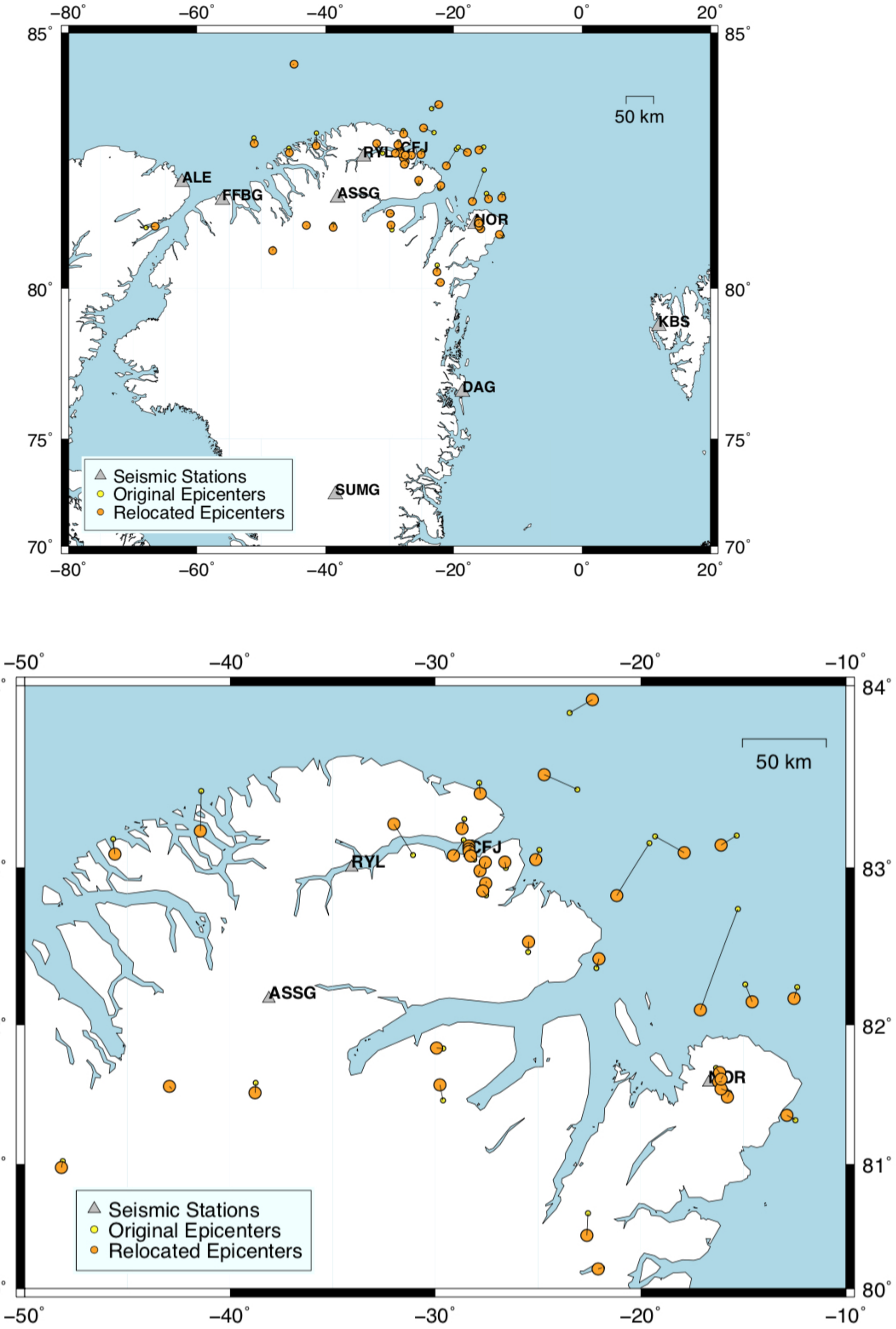

Figure 5.10: Change between the original locations and the locations obtained when locating the with Velocity Model 1.

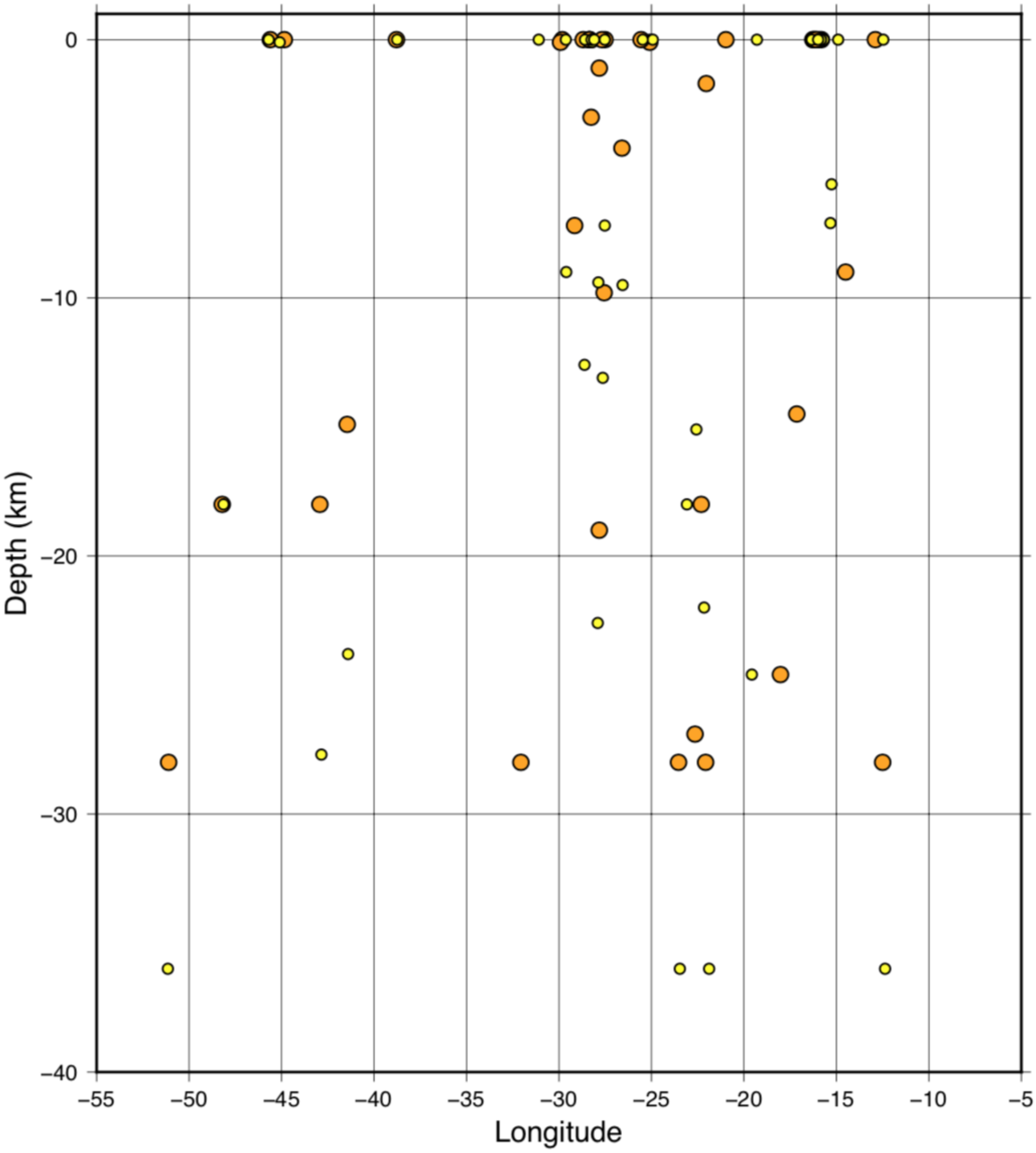

Figure 5.11: Earthquake depths as a function of longitude. Orange circles represent depths corresponding to the epicenters plotted in Figure 5.10, using Velocity Model 1. Yellow circles represent the earthquake depths obtained when locating with the Greenland Velocity Model.

The depth for each individual event when locating with Velocity Model 1 (orange) compared to when locating with the Greenland Velocity Model (yellow), is shown in Figure 5.12. Most earthquakes obtain a shallower depth or no change in depth when relocated. Six of the relocated events are relocated to a deeper origin. Many of the earthquakes that have the same depth for the original and the relocated locations are estimated to originate at the surface. To determine if the relocations are improvements to the old locations, the RMS values are used. The RMS represents a better (negative value) or a worse (positive value) estimate based on three parameters: Longitude, latitude and depth.

Figure 5.13 shows how the RMS value changes when the earthquakes are relocated with the new velocity model. The depths are also represented as the difference between the two velocity models, where a negative change in depth implies a shallower earthquake and a positive change refer to a deeper earthquake. Most of the events have a RMS change of ±0.4 and a depth change of ±10 km. Almost 50% of the earthquakes do not change in depth.

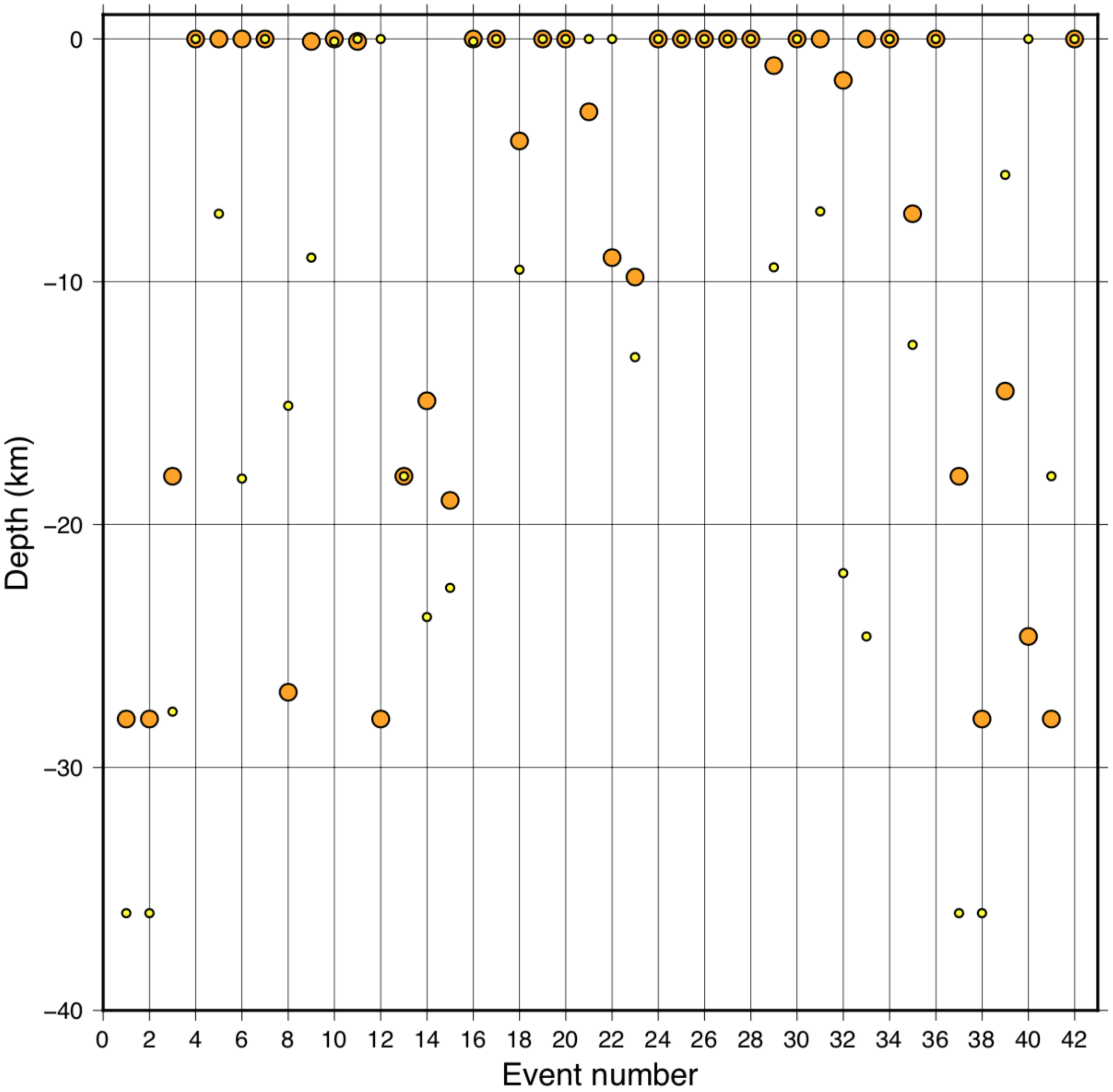

Figure 5.12: Comparison of earthquake depths for each event, obtained with the Greenland Velocity Model (yellow) and Velocity Model 1 (orange).

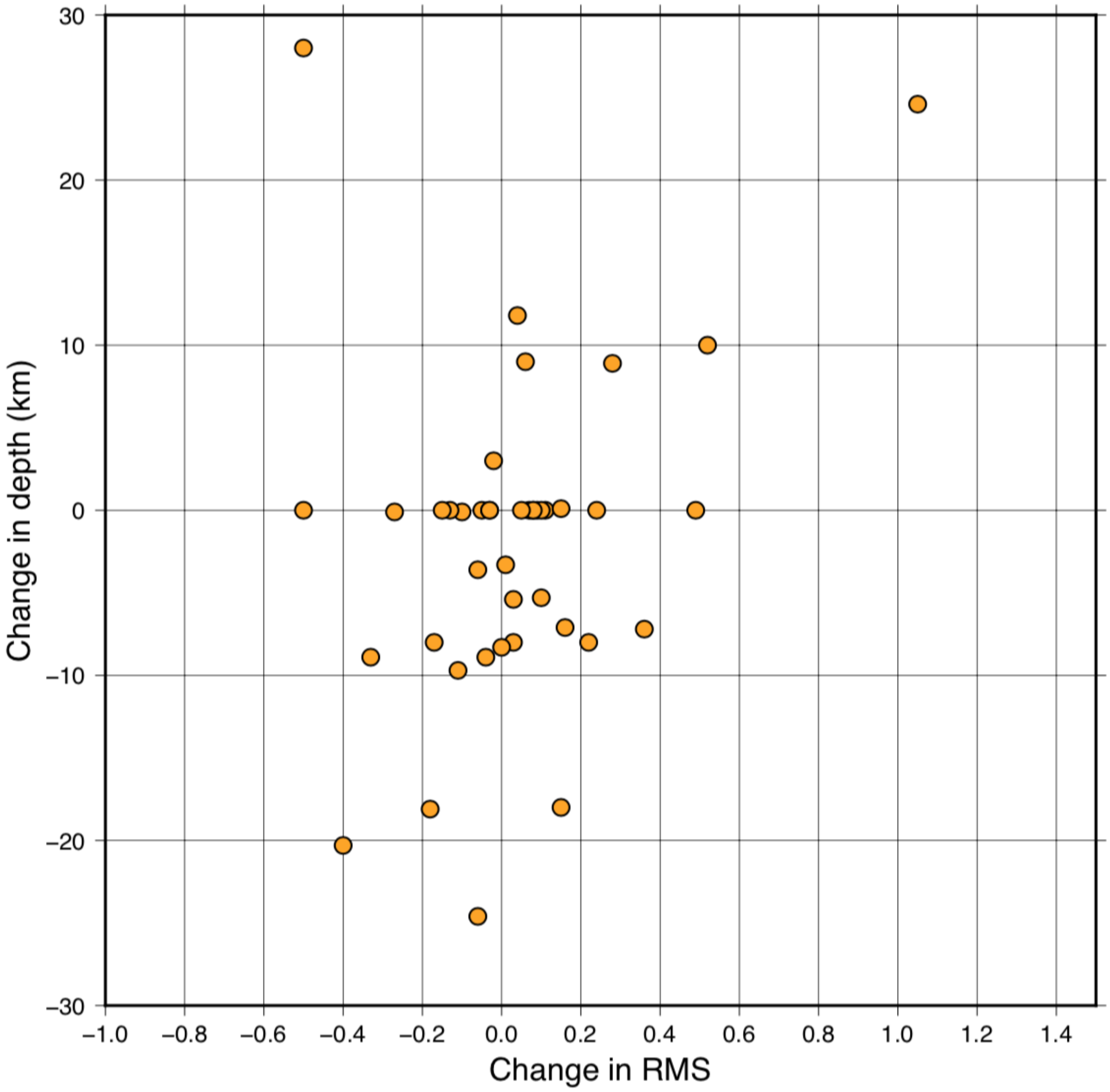

Figure 5.13: The orange dots show how much the earthquake depth changes in the relocation. The depths are plotted as a function of the RMS change. A negative RMS value indicate less uncertainty.

6. Discussion

In this chapter the crustal structure results from the joint inversion and the results from the relocation will be discussed and viewed in context of the North Greenland study area.

6.1 Structure

When interpreting the structure results from the joint inversion for this area, it is important to think about the fact that the temporary stations were deployed for four years, but there are many time periods during those years without data. The amount of data and the data accessible for these stations are thus limited. The results for the temporary stations are in some cases questionable, but at the moment, no more data is available to make the results better.

6.1.1 Comparison with Previous Studies

In this section, the crustal thickness estimated from previous studies are compared with the joint inversion results. The two permanent stations ALE and NOR have been investigated earlier and the estimated crustal thickness beneath these stations has been published. The Moho depth beneath the temporary stations has not been published in any papers, but Trine Dahl-Jensen from GEUS has worked with data from these stations and the receiver functions were also stacked through the GLImER procedure. These sources are used as comparison to the joint inversion results.

The estimated Moho depths from different sources beneath the permanent

	ALE	**NOR**
EARS	25	32
GLImER	27	37
Paper by Ramesh et al. (2002)	22	-
Paper by Gregersen et al. (1988)	-	29.5
Trine Dahl-Jensen	21	29.5
Joint Inversion	**26**	**31**

Table 6.1: Comparison of estimated Moho depths beneath the permanent stations. All depths are in km.

stations are shown in Table 6.1. From the joint inversion method applied in this thesis, the result for station ALE is a Moho depth at 26 km. This is a good comparison to previous studies. For station NOR, the estimated Moho depth is at 31 km. This estimation is also consistent to previous studies. The structure beneath these permanent stations seems to be consistent for different methods. This could be because the two stations have been in operation for many years and a lot of data are available.

There is more uncertainty related to the results from the temporary stations. This could be because the amount of data available for the stations are limited. Fewer events recorded lead to less individual receiver functions. The observed radial receiver function obtained when stacking all the individual receiver functions will most likely be better when more receiver functions are included. Also, for the temporary stations, the inversion ran the maximum amount of iterations, something it did not do for the permanent stations. This could also be an indication of better and more consistent data quality for the permanent stations compared to the temporary stations.

Table 6.2 represents the estimated crustal thickness beneath the temporary stations. From this table the resulting depths for station ASSG appear to be more consistent for the different methods, but for station FFBG and CFJ, the results are quite different from each other. The results in Table 6.1 and

	FFBG	**ASSG**	**CFJ**
GLImER	30/40	38	21
Trine Dahl-Jensen	27.5	40	34.5
Joint Inversion	**37**	**35**	**19**

Table 6.2: Comparison of estimated Moho depths beneath the temporary stations. All depths are in km.

Table 6.2 are obtained using different methods, shortly explained below.

The method applied by GLImER is an automated receiver function analysis that was explained earlier. EARS, The EarthScope Automated Receiver Survey, is another automated method (Crotwell and Owens, 2005) where data is automatically collected from IRIS stations. The difference from GLImER is that the deconvolution is performed on the raw data to remove the source time function and obtain the radial receiver function. Both methods use the time delay between the first arriving incident P-wave and the slower Ps-wave from the radial receiver function. In addition to this, EARS use the time delay multiples. These travel time delays are used to estimate layer thickness (H) and the Vp/Vs-ratio (k) for the different interfaces. The RFs are then stacked with the travel times. This is called the H-k stacking method and this method is explained by Zhu and Kanamori (2000). Dahl-Jensen (GEUS) and Ramesh et al. (2002) also used the H-k stacking method. The article by Gregersen et al. (1988) used spectral ratio curves for long period P-waves to obtain the Moho depth, which is a method that takes advantage of the amplitude differences between the horizontal and vertical components in the seismometer.

6.1.2 A Closer Look at Two Stations

From the joint inversion, two of the temporary stations gave ambiguous results that were hard to interpret. Dahl-Jensen (personal communication,

2018) estimated the Moho at a different depth than what was estimated with the joint inversion method for these two stations. The results for the two stations are therefore discussed in more detail.

For the station FFBG, the problem was that the estimated receiver function did not fit the observed receiver function at all. Since the method is a weighted algorithm, it is possible to change the weighting between the receiver function and the apparent velocity in the inversion. This was done for station FFBG, to see if it affected the result somehow. Different weights were tried and the best fit was obtained when the weighting of the receiver function remained at 1, but the weighting for the apparent S-velocity was set to 10. This means that the inversion tries to fit the receiver function more than the apparent velocity. This resulted in a better fit between the observed and estimated receiver function. The result from the inversion, where the receiver function is given more weight than the apparent velocity, is shown in Figure 6.1.

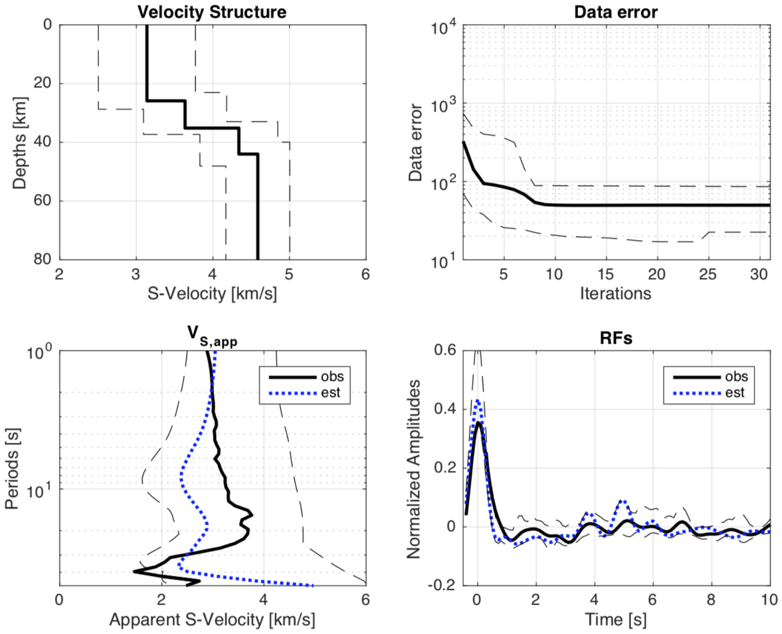

Figure 6.1: Result from station FFBG, when the RF is given more weight than the apparent velocity (1:10).

The main problem with the data from the FFBG station is that the Moho peak is not a clear peak in the observed RF. There is nothing to do about this problem and this is probably the best fit obtainable for the available data. When changing the weighting for this station, the fit between the observed RF and the estimated RF got better. The error bars for the receiver function and the data error got smaller, while the error increased for the apparent velocity and the S-velocity in the crust, as expected. This lead to small changes in the main structure. The velocity increase assumed to correspond to the Moho depth decreased from 37 to approximately 35 km. The boundary layer above the Moho boundary got deeper, as the estimated depth changed from 22 km to 27 km. This new boundary layer seems to fit the depth estimated to be the Moho depth by Dahl-Jensen (personal communication, 2018). This implies that it is highly reasonable that there is a boundary at this depth, but it can be discussed if this is the Moho boundary or not. For the joint inversion results, the velocities corresponding to the boundary at 27.5 km are too low to represent mantle velocities and the estimated Moho depth of the deeper boundary remains.

The Moho depth beneath station CFJ is not consistent with the results from the other stations, as neither of the structures beneath the other stations interprets a Moho this shallow. Also, the Moho peak in the observed RF was a little ambiguous. The structure result presented a big velocity increase at 19 km and the mantle velocities were reasonable at this depth. In the observed receiver function, is was possible to locate two peaks that could represent the Moho discontinuity. From the results obtained with the joint inversion method, it was reasonable to assume that the Moho indeed is found at a depth of 19 km, both because of the distinct jump in S-velocity and because of the fit between the estimated and observed RF. The boundary after what is assumed to be the Moho, is represented as a small boundary in the velocity structure and the peak in the receiver function corresponding to this velocity increase is not that clear.

Different weighting were also tested for this station and the best fit was obtained when the weighting for the apparent velocity was set to 10, and the

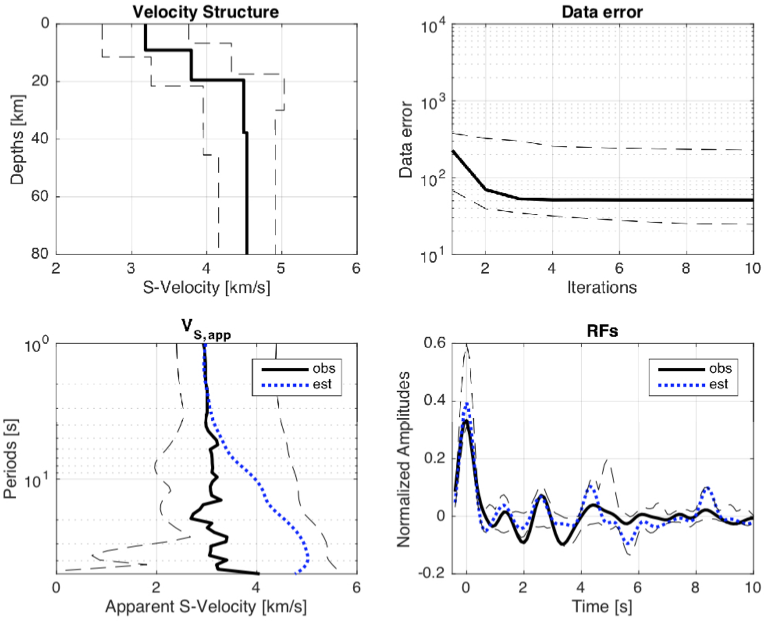

Figure 6.2: Result from station CFJ, when the RF is given more weight than the apparent velocity (1:10).

receiver function weight remained at 1. The result is shown in Figure 6.2.

When changing the weights on the inversion for station CFJ, it is seen that the errors in the receiver functions and the data error get smaller, while the error for the apparent and absolute velocities increases, as expected. In the new results, the deepest velocity increase in the mantle gets smaller, supporting the interpretation that the Moho discontinuity is the boundary above, at 19 km.

For station FFBG and CFJ, the assumed Moho depths estimated by Dahl-Jensen (personal communication, 2018) were visible as boundaries in the structures obtained in this study, but they are not assumed to be the Moho discontinuity.

6.1.3 Comparing Results to Geology

The map in Figure 6.3 shows the geology of North Greenland and the stations' locations. According to the map, the geology in North Greenland consists of sediments deposited in the Franklinian Basin, laying above supracrustal unspecified rocks older than 1600 Ma, known as the Precambrian Shield. This sedimentation covers North Greenland and a part of Canada, and most of the seismic stations used in this thesis are placed on these sediments.

The sedimentation in the Northern region of Greenland has been documented by other authors as well. Since the study area is dominated by sedimentary basin deposits, the low velocities in the upper crust obtained from the joint inversion are reasonable. Especially for station NOR, the joint inversion showed results that implied that the upper crustal velocities were low for the first layer, estimated to be 7 km thick. This could be representing a sediment basin. With the layer below, there is a stark velocity contrast, evident from the resulting structure. This is logical if there are sediments laying above consolidated material.

The sedimentary basins in North Greenland have been documented recently by Darbyshire et al. (2018), in a study using Rayleigh wave group velocities, resulting in an image of the crust and uppermost mantle in Greenland. The average velocities for the crust in the article were estimated to be lower in the northern and southern part of Greenland, compared to central Greenland. Crustal thickness was determined from the shear wave velocities, where the transition to velocities over ~ 4.2 km/s represents the transition from crust to mantle.

The map in Figure 6.3 also shows where some long wide-angle seismic reflection/refraction (WAR) profiles were gathered (the black lines named LORITA) (Jackson et al., 2010). An estimated crustal thickness at the very west of this profile line, on the continental shelf, was estimated to be 27 km. It can be assumed that the crustal thickness beneath station FFBG on the coast is not

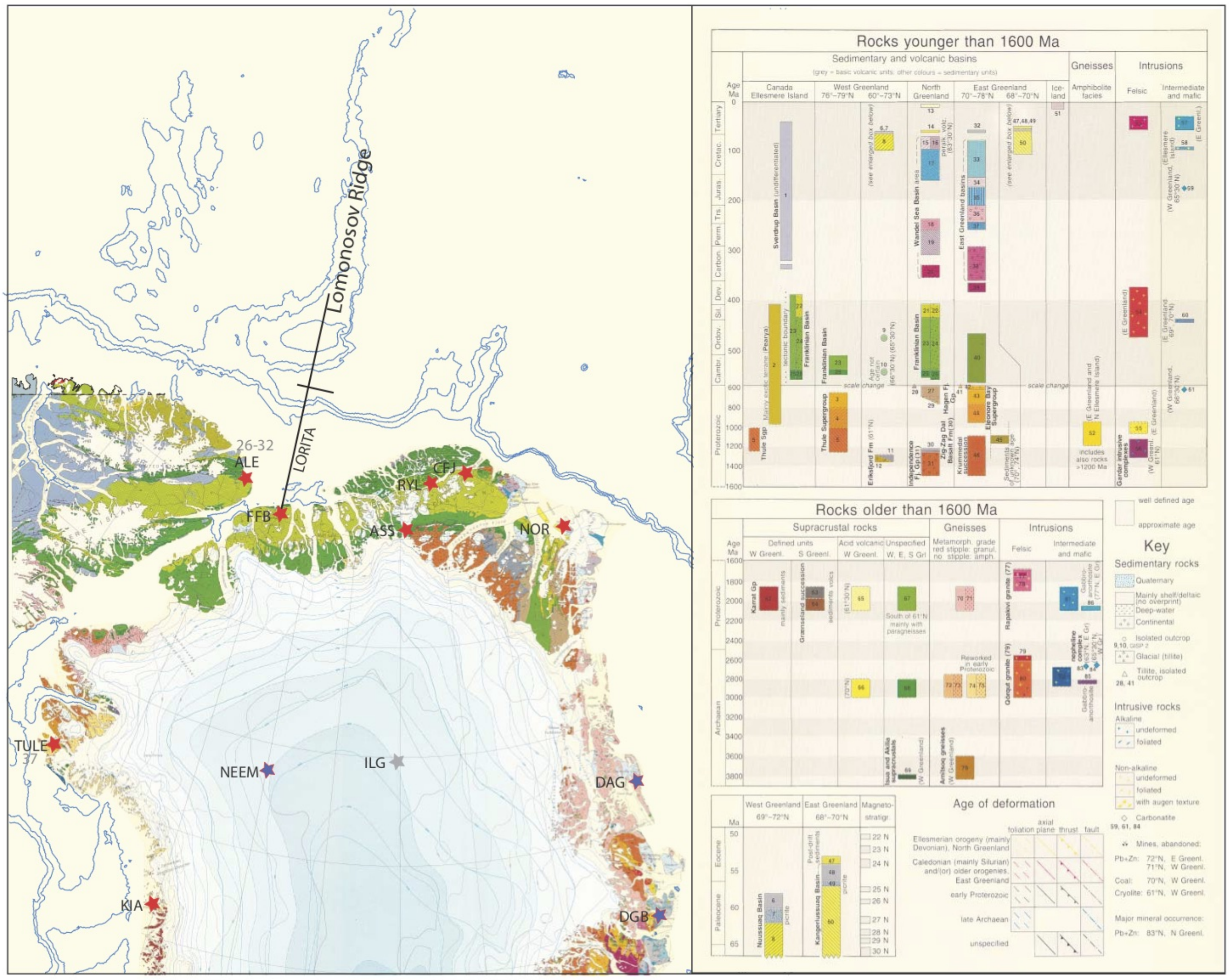

Figure 6.3: Geological map of North Greenland showing the location of the stations. Figure obtained from Trine Dahl-Jensen (personal communication, 2018).

that different from the estimate done by Jackson et al. (2010). According to Dahl-Jensen (personal communication, 2018), the H-k stacking method beneath station FFBG gave results comparable to 27 km. The results from the joint inversion gave an estimated thickness 10 km deeper than this.

Another study based on gravity anomalies also estimated the crustal thickness in Greenland (Braun et al., 2007). They compared their results with the Moho depths estimated with seismic waves by Dahl-Jensen et al. (2003). The results fit quite well with uncertainties between 2-5 km. Station ALE in Canada was also included in the gravity study and the result was compared with the receiver function study by Ramesh et al. (2002). The gravity study estimated a deeper Moho than the receiver function study, which actually gave a slightly shallower estimate than the other sources in Table 6.1. The gravity study did show that the crustal thickness in the Franklinian Basin is shallower than in the rest of Greenland.

The structure results from the joint inversion resulted in P-wave velocities in the mantle that are lower than what we expected. The global average P-wave velocity in the mantle is above 8 km/s and the results for the joint inversion showed a P-wave velocity around 7.5 km/s. This low velocity could be derived from the assumed Vp/Vs-ratio when converting from S-wave velocities to P-wave velocities. It could also be a result of the starting model(s) chosen. Since the estimated S-wave velocity is better constrained for shallower depth, the estimated velocities in the mantle have a larger uncertainty with depth.

6.2 Relocation

In this section, the Greenland Velocity Model and Velocity Model 1 will be compared and the relocation results will be discussed.

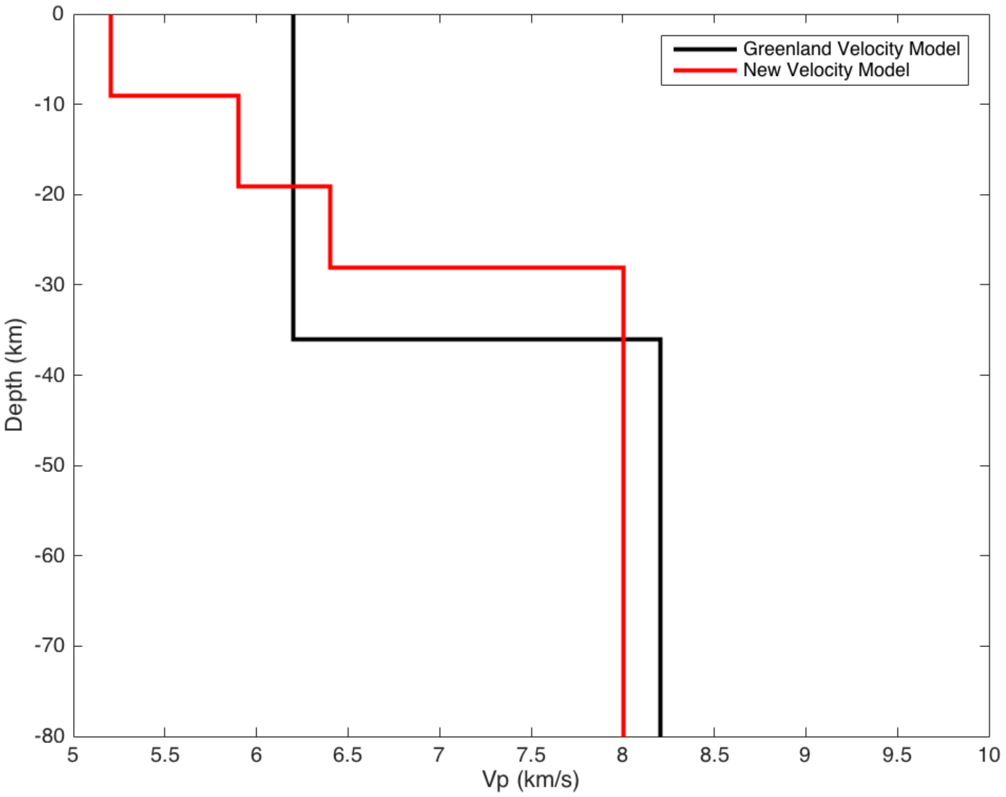

Figure 6.4: Comparison of the original Greenland Velocity Model and the new velocity model obtained through this study.

6.2.1 Comparing the Two Velocity Models

The original Greenland Velocity Model is the same as the one used for the Canadian Shield, so it is assumed that the geology of Greenland is similar to the geology of Canada. The velocity model is not based on imaging of the crustal structure in the area, something that the new regional velocity model is. A robust, detailed shear wave velocity structure was obtained through the joint inversion method. The two velocity models are shown in Figure 6.4. It is seen that the new velocity model is a more detailed velocity model than the Greenland Velocity Model, and the mantle velocities are slightly lower for the newer model.

The synthetic tests carried out in Chapter 4 (Method), showed how wrong the location estimate can be when the location process is performed with a velocity model that is too simple for the crustal structure of a region. Since the imaging of the subsurface revealed a structure more complicated than the structure in the current Greenland Velocity Model, there are reasons to believe that the locations obtained with the old velocity model is wrong.

6.2.2 Comparing the Locations

The largest changes in locations obtained with the two velocity models are in the North-South direction. Also, some of the earthquakes that were located randomly in relation to each other with the Greenland Velocity Model, appear to locate on a line relative to each other when located with the new velocity model. This especially applies for the earthquakes relocated just above latitude 82° and around latitude 83°. This is shown in Figure 6.5.

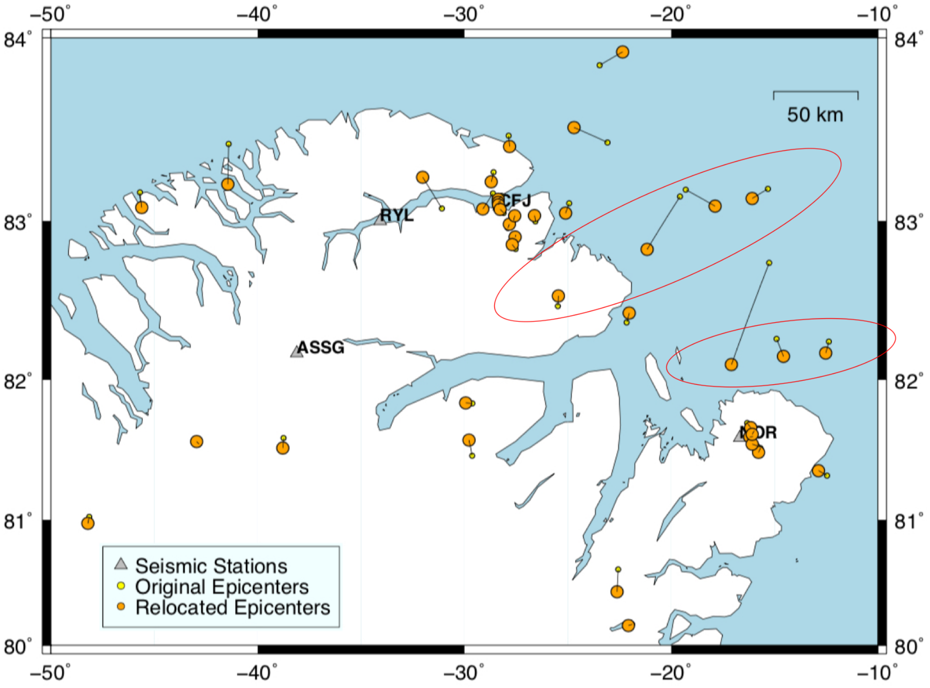

Figure 6.5: Some earthquakes are relocated in a way that they appear to be connected.

Most of the seismic stations in this study are located on a line relative to each other. The two stations causing the geometry of the stations to be better, are SUMG, DAG and KBS (see distribution of the stations in Figure 3.1). These stations are however quite far away, and less earthquakes are recorded by the stations. How many of the stations the earthquake was recorded on might also have an effect of how good both the original and relocated epicenter estimates are.

To see if the relocated hypocenters are better estimates than the original ones, the RMS is important. The RMS for each individual event for the two velocity models is shown in Figure 6.6. It is seen that event numbers 4, 6, 13 and 37 stand out with a high RMS for both velocity models, and for most of the events the RMS values for the two velocity models are quite similar. For a few of the earthquakes the difference in RMS is quite large, e.g. event number 36 and 40.

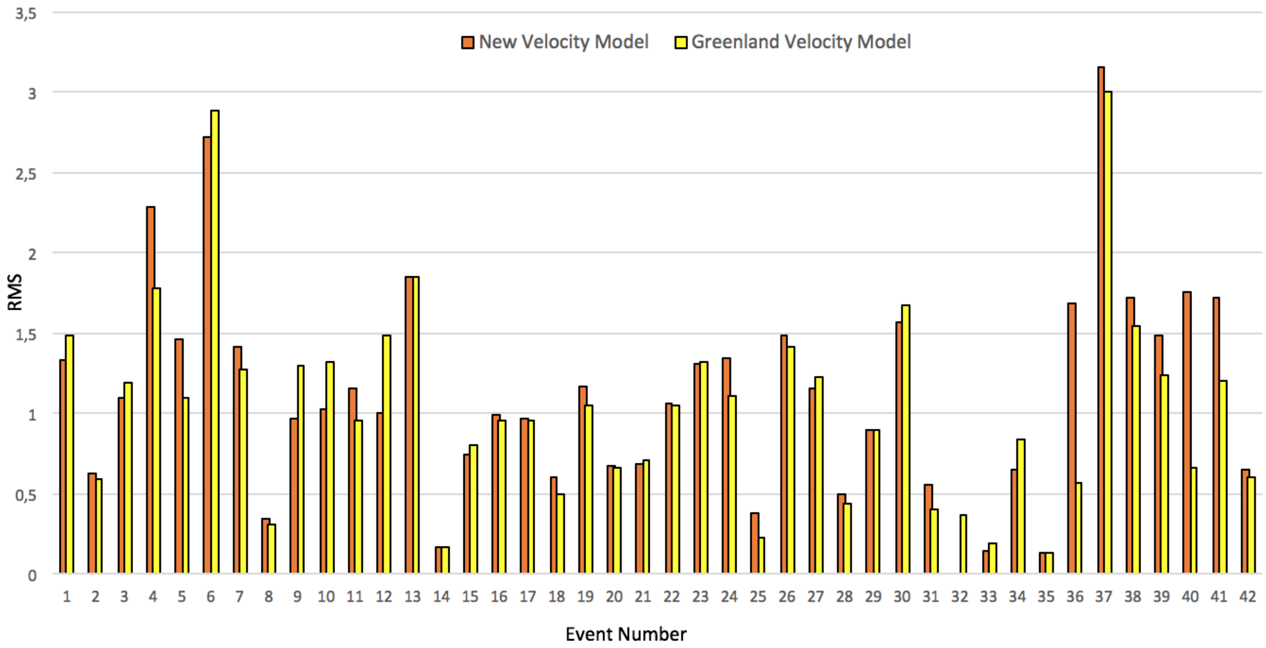

Figure 6.6: RMS error for the 42 events. Yellow bars represent RMS errors from the locations obtained with the Greenland Velocity Model and orange bars represent RMS obtained using the new velocity model.

6.2.3 Analysis of Individual Events with High RMS

The high RMS values does imply a poor fit and a high uncertainty in the location estimate. The events with an RMS value above 1.8 were however 1.8 or higher before the relocation was performed. Therefore, it is possible that these high uncertainties arise from mistakes done when analyzing the raw data. Wrong phases might have been picked. The seismograms for one of these events with high RMS were therefore given a second look. The seismograms for event number 6 are shown in Figure 6.7. It can be discussed if some P- and/or S-phase are picked at the wrong time.

If the phases are picked wrong, it implies that the overall RMS could be lower than it is now.

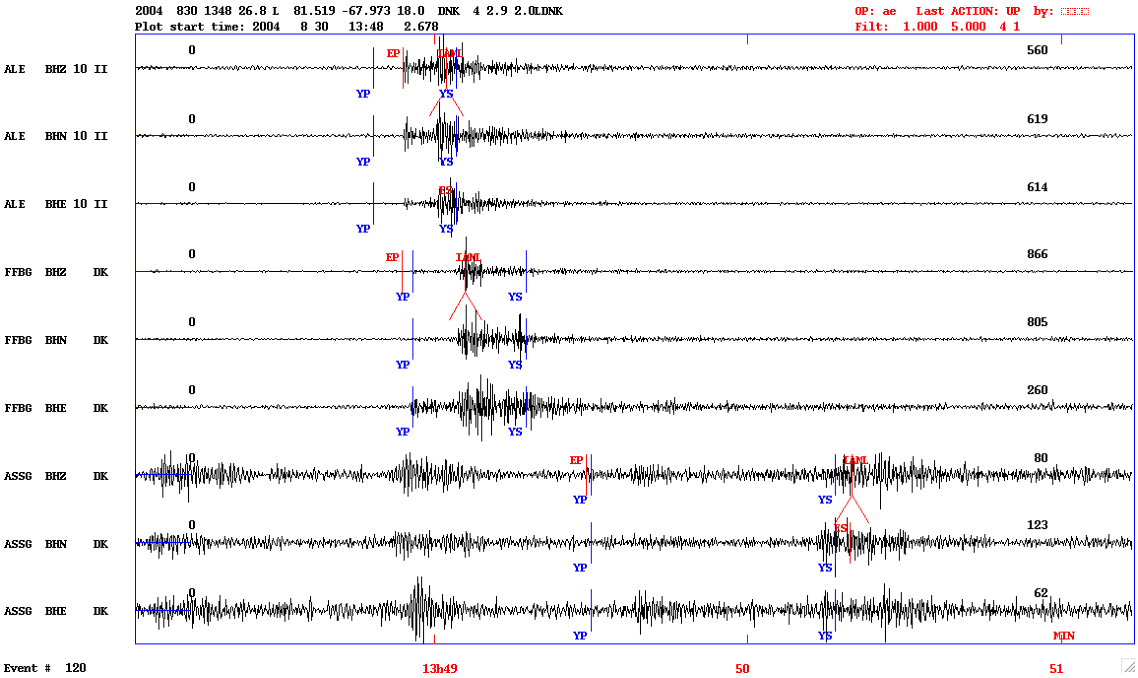

Figure 6.7: Seismograms for event number 6. The earthquake was recorded by three stations: ALE, FFBG and ASSG.

6.2.4 Is the New Velocity Model an Improvement?

The Greenland Velocity Model has one layer above Moho, where the average P-wave velocity is 6.2 km/s. This might be a good average for the crust, but it is highly unlikely that the velocity in the upper crust is ever that high. The new velocity model has three layers above Moho, where the velocities in the upper crust are around 5.2 km/s, which is more realistic for the sedimentary layers.

However, the RMS-values reveal that it is not that straight forward. Many of the events do get a lower RMS relocated with the new velocity model, but many events also get a higher RMS. This makes it difficult to determine if the new detailed velocity model is actually better than the simple velocity model. The overall RMS for the events located with the Greenland Velocity Model is 1.227, while the overall RMS for the new velocity model is 1.279. The RMS for the Greenland Velocity Model has a lower error and the percentage change for the new velocity model is 4.23%.

In Figure 6.8 the events with RMS above 1.5 are left out for comparison, to make it easier to distinguish the events that have more reasonable RMS values. When the events with RMS above 1.5 are removed, the overall RMS value for the events obtained with the new velocity model is slightly lower than the events located with the Greenland Model. The values are 0.852 and 0.855, respectively.

From the comparison of the two velocity models in Figure 6.4 we can see that the new velocity model has a shallower Moho than the original velocity model. Many previous studies have shown that the crustal thickness in North Greenland is thinner than the rest of Greenland, something that support the structure of the new velocity model.

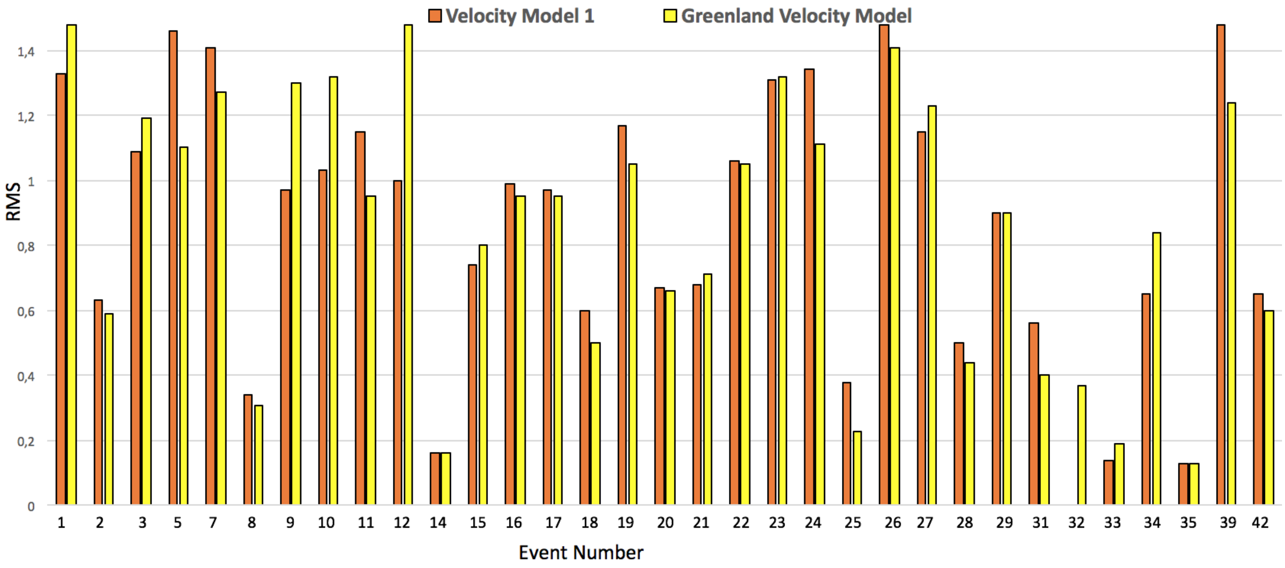

Figure 6.8: RMS error for events with RMS < 1.5. Yellow bars represent RMS from the locations obtained with the Greenland Velocity Model and orange bars represent RMS obtained using the new velocity model.

6.3 Seismicity

It is clear that the seismicity in North Greenland is poorly known and it is difficult to obtain more information in this area. It is also difficult to do something about this, as the area is so remote. Deploying and maintaining stations are challenging in areas where the power supply is limited. The earthquakes in the region are normally not of a large magnitude, so the earthquakes will not be registered at stations too far away.

Focal mechanisms are useful tools to understand the tectonic processes in a region. Unfortunately the data used in this thesis are not good enough to make any fault plane solutions. In the study area, only four fault plane solutions have been obtained since 1976, revealing the low seismicity in the area. It is therefore not surprising that no new fault plane solutions were obtained in this study.

In Figure 6.9 the available focal mechanisms in the region are plotted with the earthquakes found between 2004 and 2007, located with Velocity Model 1.

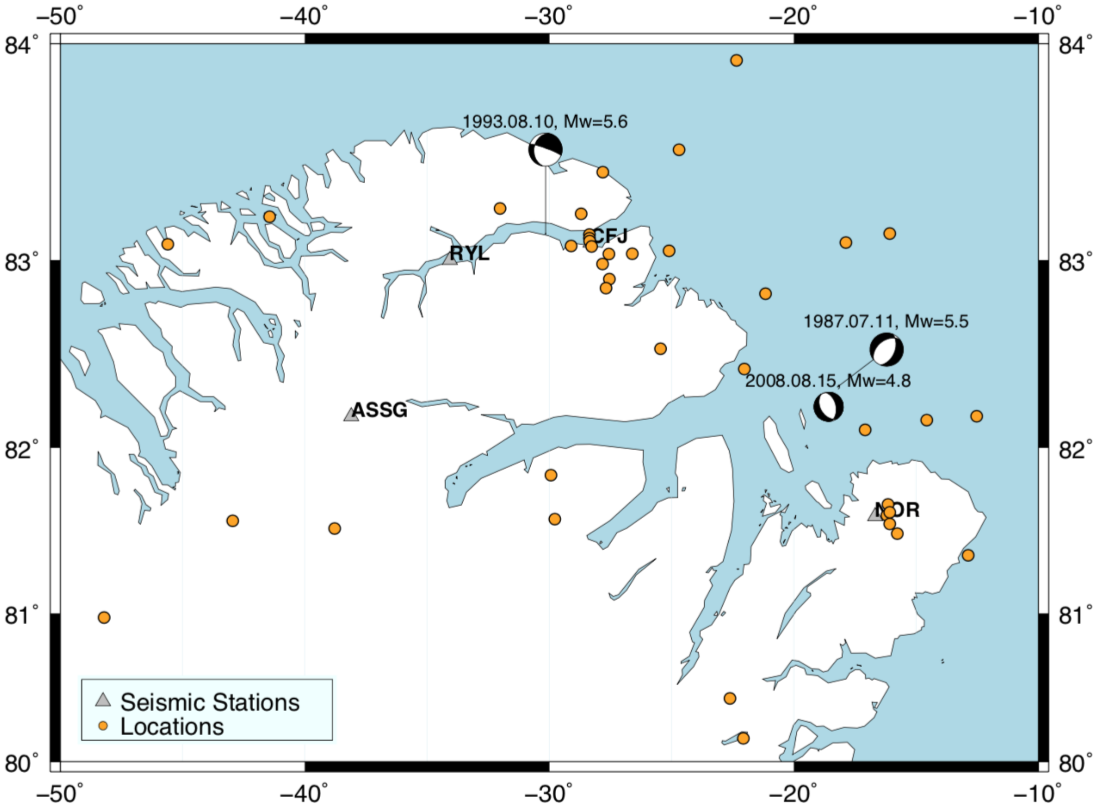

Figure 6.9: Earthquakes located with the new velocity model and the available fault plane solutions in the region.

Examining the few focal mechanisms available from previous years, they seem to be present relatively close to where many of the earthquakes located in this study are clustered. This was done to see if there is a connection between the sources causing the earthquakes. The most recent fault plane solution is obtained in 2008, with a Mw=4.8. This normal fault solution appears to be on an extended line from the earthquakes around station NOR. Maybe the earthquakes are generated from the same fault. The clustering of events around the stations and the locations of the available fault plane solutions could imply seismic zones.

6.4 Further Work

More work could be done with the data set obtained through this thesis. One thing that should be done is to go back to the seimograms and do a quality check of the phases that are picked, at least for the events with high RMS. It could also be interesting to relocate other earthquakes in the region with the new velocity model obtained here.

The data forming the basis of this thesis is limited. This is evident from the data quality difference between the permanent and temporary stations in the inversion process. Obtaining more data from the remote area in North Greenland would give less ambiguous results. To obtain more data, stations must be deployed and monitored in this area again. These stations should have a more secure source of power than previously, or more batteries. However, this is difficult and an expensive task. I argue that there is a potential of understanding the region even better, if more data could be obtained.

Another way of obtaining a new velocity model for the region is by using the travel time inversion method. This method was discussed at the beginning of the work with this thesis, but we concluded that there was too little data. Maybe it could still be tried.

7. Conclusion

The main objective of this thesis was to obtain a new regional velocity model for North Greenland and relocate earthquakes in the region. This has been done.

Synthetic tests were first performed to illustrate the importance of choosing a suitable velocity model in the location process. Estimating earthquake locations using a velocity model significantly different from the true crustal structure can give locations with great error. Therefore, it is important with knowledge about the crustal structure in the region where earthquakes are being located.

The joint inversion of receiver functions and apparent S-wave velocities was applied to obtain crustal information beneath the stations in North Greenland. The structure results were further implemented to make a new detailed velocity model for the region.

In total, 42 earthquakes were found in North Greenland between 2004-2007. They were first located with the Greenland Velocity Model and then relocated with the new regional velocity model. Some of the locations changed significantly when relocated. The overall RMS value is slightly lower when the events are located with the Greenland Velocity Model. Even though this is the case, the new velocity model is more meaningful, when seen in context with the geology in the region.

Bibliography

Ammon, C. J., Randall, G. E., and Zandt, G. (1990). On the nonuniqueness of receiver function inversions. *Journal of Geophysical Research: Solid Earth*, 95(B10):15303–15318.

Blinova, M. (2011). Seismic study along the west Spitsbergen continental margin and adjacent area of the West Spitsbergen Fold and Thrust Belt (Isfjorden).

Braun, A., Kim, H. R., Csatho, B., and von Frese, R. R. (2007). Gravity-inferred crustal thickness of Greenland. *Earth and Planetary Science Letters*, 262(1-2):138–158.

Burdick, L. J. and Langston, C. A. (1977). Modeling crustal structure through the use of converted phases in teleseismic body-wave forms. *Bulletin of the Seismological Society of America*, 67(3):677–691.

Crotwell, H. P. and Owens, T. J. (2005). Automated receiver function processing. *Seismological Research Letters*, 76:702–708.

Dahl-Jensen, T., Larsen, T. B., Woelbern, I., Bach, T., Hanka, W., Kind, R., Gregersen, S., Mosegaard, K., Voss, P., and Gudmundsson, O. (2003). Depth to Moho in Greenland: receiver-function analysis suggests two Proterozoic blocks in Greenland. *Earth and Planetary Science Letters*, 205(3-4):379–393.

Darbyshire, F. A., Dahl-Jensen, T., Larsen, T. B., Voss, P. H., and Joyal, G. (2018). Crust and uppermost-mantle structure of Greenland and the Northwest Atlantic from Rayleigh wave group velocity tomography. *Geophysical Journal International*, 212(3):1546–1569.

Drottning, A. F. (2017). Inversion of Teleseismic Polarization Data for Crustal Velocities in Norway. Master's thesis, The University of Bergen.

Dziewonski, A. M., Chou, T. A., and Woodhouse, J. H. (1981). Determination of earthquake source parameters from waveform data for studies of global and regional seismicity. *Journal of Geophysical Research: Solid Earth*, 86:2825–2852.

Ekström, G., Nettles, M., and Dziewonski, A. M. (2012). The global CMT project 2004–2010: Centroid-moment tensors for 13,017 earthquakes. *Physics of the Earth and Planetary Interiors*, 200-201:1–9.

Gregersen, S. (1982). Earthquakes in Greenland. *Bulletin of the Geological Society of Denmark*, 31:11–27.

Gregersen, S. (1984). Crustal structure anomalies detected with Lg waves in grabens near continental margins in Greenland and in the North Sea. *Marine Geophysical Researches*, 6(4):409–413.

Gregersen, S., Clausen, C., and Dahl-Jensen, T. (1988). Crust and upper mantle structure in Greenland. *Recent Seismological Investigations in Europe*, Proceedings of the 19th General Assembly of the ESC, Nauka, Moscow:467–469.

Håkansson, E. and Pedersen, S. A. S. (2001). The Wandel Hav Strike-Slip Mobile Belt - A Mesozoic plate boundary in North Greenland. *Bulletin of the Geological Society of Denmark*, 48:149–158.

Håkansson, E. and Stemmerik, L. (1989). Wandel Sea basin - A new synthesis of the late Paleozoic to Tertiary accumulation in North Greenland. *Geology*, 17(8):683–686.

Havskov, J. and Bungum, H. (1987). Source parameters for earthquakes in the northern North Sea. *Norsk Geologisk Tidsskrift*, 67:51–58.

Havskov, J. and Ottemoller, L. (1999). Seisan earthquake analysis software. *Seismological Research Letters*, 70(5):532–534.

Henriksen, N., Higgins, A., Kalsbeek, F., and Pulvertaft, T. C. R. (2000). Greenland from Archaean to Quaternary. Descriptive text to the Geological map of Greenland 1:2 500 000. *Geological Survey of Denmark and Greenland Bulletin*, 185:1–93.

Henriksen, N. and Higgins, A. K. (2000). Early Palaeozoic Basin Development of North Greenland - Part of the Franklinian Basin. *Polarforschung*, 68:131–140.

Higgins, A. K., Soper, N. J., and Leslie, A. G. (2000). The Ellesmerian and Caledonian orogenic belts of Greenland. *Polarforschung*, 68:141–151.

Jackson, H. R., Dahl-Jensen, T., Chian, D., Shimeld, J., Funck, T., Asudeh, I., and Snyder, D. (2010). Sedimentary and crustal structure from the Ellesmere Island and Greenland continental shelves onto the Lomonosov Ridge, Arctic Ocean. *Geophysical Journal International*, 182(1):11–35.

Kanao, M., Suvorov, V. D., Toda, S., and Tsuboi, S. (2015). Seismicity, structure and tectonics in the Arctic region. *Geoscience Frontiers*, 6(5):665–677.

Kennett, B. L. N. and Engdahl, E. R. (1991). Travel times for global earthquake location and phase association. *Geophysical Journal International*, 105:429–465.

Larsen, T. B., Voss, P. H., Dahl-Jensen, T., and Rasmussen, H. P. (2014). Earthquake swarms in Greenland. *Geological Survey of Denmark and Greenland Bulletin*, 31:75–78.

Laske, G., Masters, G., Ma, Z., and Pasyanos, M. (2013). Update on CRUST1. 0 - A 1-degree Global Model of Earths Crust. 15:2658.

Laughton, A. S. (1975). Tectonic evolution of the northeast Atlantic Ocean; a review. *Norges Geologiske Underskelse*, 316:169–193.

Marshak, S. (2011). *Earth: Portrait of a Planet: Fourth International Student Edition*. WW Norton & Company.

Nuttli, O. and Whitmore, J. D. (1961). An observational determination of the variation of the angle of incidence of P waves with epicentral distance. *Bulletin of the Seismological Society of America*, 51(2):269–276.

Ramesh, D. S., Kind, R., and Yuan, X. (2002). Receiver function analysis of the North American crust and upper mantle. *Geophysical Journal International*, 150(1):91–108.

Rondenay, S. (2009). Upper Mantle Imaging with Array Recordings of Converted and Scattered Teleseismic Waves. *Surveys in Geophysics*, 30(4-5):377–405.

Rondenay, S., Spieker, K., Sawade, L., Halpaap, F., and Farestveit, M. (2017). GLImER: A New Global Database of Teleseismic Receiver Functions for Imaging Earth Structure. *Seismological Research Letters*, 88(1):39–48.

Rosa, D., Schneider, J., and Chiaradia, M. (2016). Timing and metal sources for carbonate-hosted Zn-Pb mineralization in the Franklinian Basin (North Greenland): Constraints from Rb-Sr and Pb isotopes. *Ore Geology Reviews*, 79:392–407.

Stemmerik, L., Dalhoff, F., Larsen, B. D., Lyck, J., Mathiesen, A., and Nilsson, I. (1998). Wandel Sea Basin, eastern North Greenland. *Geology of Greenland Survey Bulletin*, 180:55–62.

Svenningsen, L. and Jacobsen, B. H. (2007). Absolute S-velocity estimation from receiver functions. *Geophysical Journal International*, 170(3):1089–1094.

Tessensohn, F. and Piepjohn, K. (2000). Eocene compressive deformation in Arctic Canada, North Greenland and Svalbard and its plate tectonic causes. *Polarforschung*, 68:121–124.

Zhu, L. and Kanamori, H. (2000). Moho depth variation in southern california from teleseismic receiver functions. *Journal of Geophysical Research: Solid Earth*, 105(B2):2969–2980.